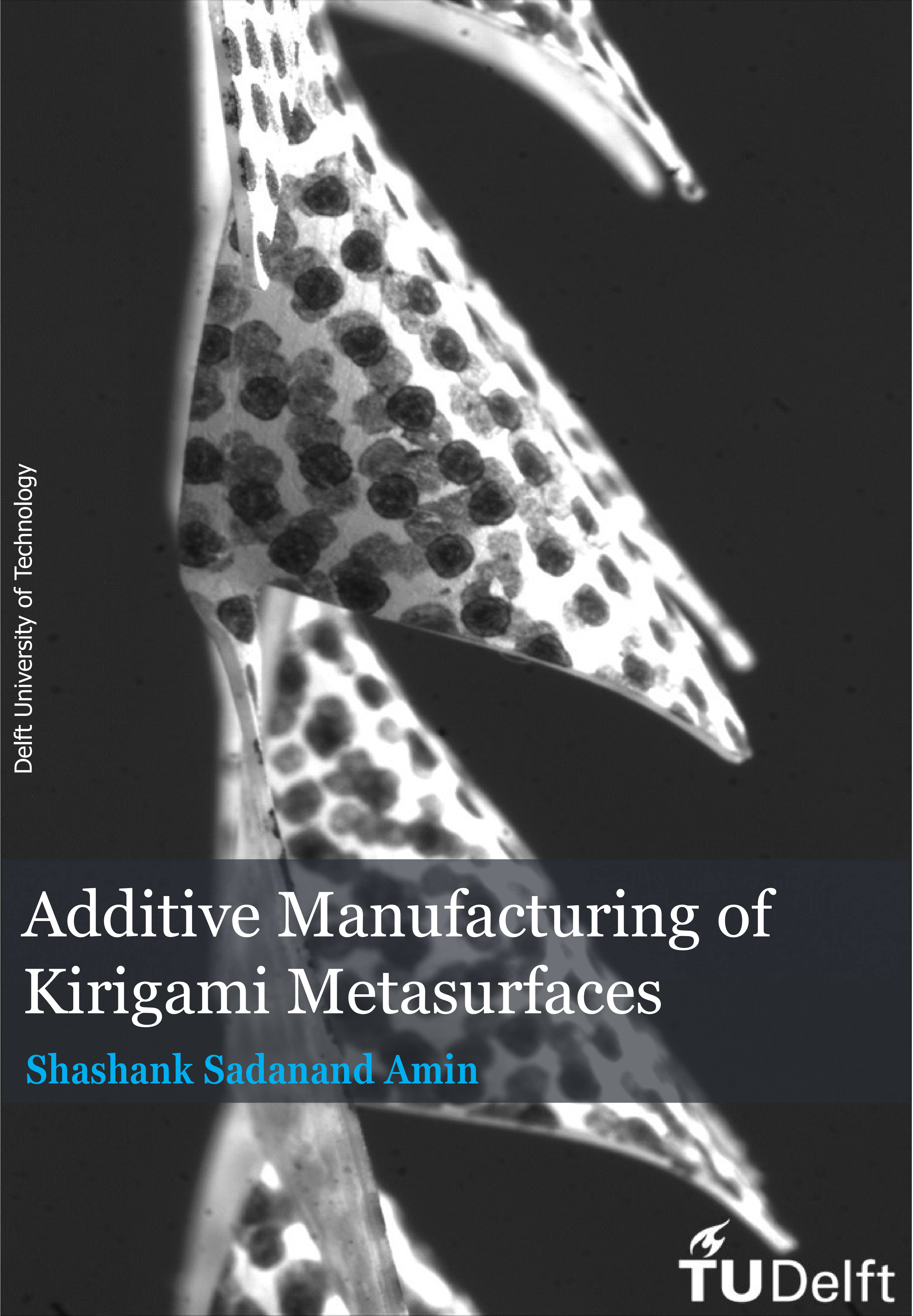

Delft University of Technology

Additive Manufacturing of Kirigami Metasurfaces

Shashank Sadanand Amin

TU Delft

Additive Manufacturing of Kirigami Metasurfaces

by

Shashank Sadanand Amin

in partial fulfilment of the requirements for the degree of

Master of Science
in Aerospace Engineering

at the Delft University of Technology.

Student Number:	5059399
Supervisors:	Dr. Kunal Masania
	Dr. Vinay Damodaran
Thesis committee:	Dr. Jovana Jovanova
	Dr. Ir. Otto Bergsma

Delft University of Technology

Preface

With this thesis, the journey of my master's has finally come to an end. Though it was a bumpy ride, it was quite fulfilling. I want to express my deepest gratitude to everyone who has helped me over its course.

First and foremost, I'd like to thank my parents. This journey would not be possible without their unfathomable and unconditional support. I'd also like to thank my sister, Disha, who stuck by me throughout and never let me experience a bleak day. She's undoubtedly the best elder sibling that anyone could hope to have.

Next, I'd like to thank my supervisors–

Dr Kunal Masania for his trust and unwavering support over the past years. You have consistently expanded my knowledge horizons since day one, and your guidance through adversity has been instrumental in helping me complete this thesis. Your motivation and reassurance were invaluable both in times of strife and success.

Dr Vinay Damodaran, for his patience in helping me overcome my most trying moments and for his stellar advice in helping me navigate complex problems. It was my genuine privilege to work with and learn from both of you; I will always be grateful for it.

In addition, I'd like to thank everyone from Shaping Matter Lab, past and present, who made this research experience truly unforgettable. Working in the vicinity of such talented minds has constantly been enriching.

Lastly, I'd like to thank all my friends who helped me maintain a positive mental attitude. They've been a constant source of joy and have pushed me to dig deeper when times were tough. All of you mean the world to me, and I will always cherish you.

Shashank Sadanand Amin
Delft, December 2022

Abstract

Kirigami – the Japanese art of paper cutting – is used extensively as a design philosophy for stretchable and morphable structures. An array of cuts on a thin planar sheet creates a structure that can morph into a 3D pattern on applying an in-plane uniaxial load. This type of structure is called a kirigami metasurface. A subset of this type of structure is a buckling-induced kirigami metasurface that displays an in-plane and out-of-plane deformation response when an in-plane tensile load is applied. This metasurface type is multistable and displays a snap-through behaviour. The angles at which the cuts are made are one of the main influences behind the proportions of these in-plane and out-of-plane deformations.

Cut patterns for these kirigami metasurfaces are specified with respect to the loading direction. For example, linear cut patterns contain periodically spaced linear cuts perpendicular to the loading direction, and angular cut patterns contain periodically spaced angular cuts in the form of the legs of an isosceles triangle, with its median parallel to the loading direction.

Traditionally, stiff materials with low operating strain ranges are used to manufacture angled cut pattern kirigami metasurfaces. This work incorporates the use of high-toughness thermoplastic elastomer and fused filament fabrication (FFF) to manufacture metasurfaces with higher operating strain ranges. The influence of varying the cut pattern's geometric parameters on the metasurface's overall mechanical response is studied. Digital Image Correlation is used to quantify this out-of-plane mechanical response, and the effects of manufacturing using FFF on the bistability of the kirigami metasurface are analysed.

The results showed that the 30-degree angled cut design gave the highest out-of-plane displacement relative to the size of its spikes. This angled cut design also gave the highest projected area amongst the other angled cut design types. The maximum projected area of this 30-degree angled cut design is 2.9 times greater than a similarly sized linear cut sample.

An outcome of this work is to be the starting point for the use of FFF additive manufacturing and its design and material deposition freedom to tailor the response of the unit cells of an angled-cut kirigami metasurface. It also highlights the potential for using the angled cut design over the linear cut design for aerodynamics applications where local drag generation is favourable.

Contents

List of Figures

List of Tables

Nomenclature

AM	Additive Manufacturing
CFD	Computational Fluid Dynamics
DIC	Digital Image Correlation
FDM	Fused deposition modeling
FFF	Fused Filament Fabrication
TPE	Fused Filament Fabrication
TPE	Thermoplastic Elastomer
TPU	Thermoplastic Polyurethane
w/o	Without

1 Introduction

1.1. Origins and Etymology

Origami is the ancient Japanese art of transforming planar 2D sheets of paper into 3D sculptures with varying topologies using folding [27]. The origins of the word come from the Japanese language, with *ori* meaning ”to fold” and *kami* meaning ”paper”. Kirigami is a variation of origami in which planar sheets are cut and folded into 3D designs without using any adhesives. The origins of this word come from *Kiru*, which means ”to cut” in Japanese. An artistic example of a Kirigami pop-up is shown in Figure 1.1.

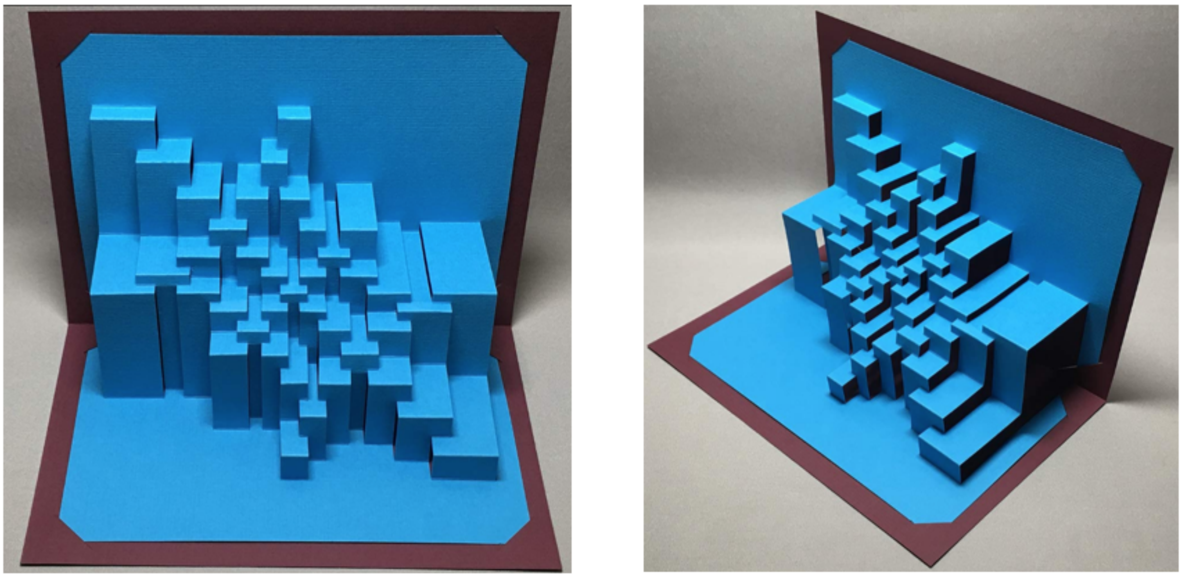

Figure 1.1: An Artistic Kirigami Pop-up [1]

1.2. Structural and Material Applications

Kirigami techniques have been adopted for design applications ranging from highly stretchable devices, Figure 1.2, to morphable and transformable structures, Figure 1.3. In these examples, an array of cuts are made on stiff planar sheets. Upon applying a tensile force, these planar sheets display a highly stretchable behaviour, many times greater than the actual stretchability of the material.

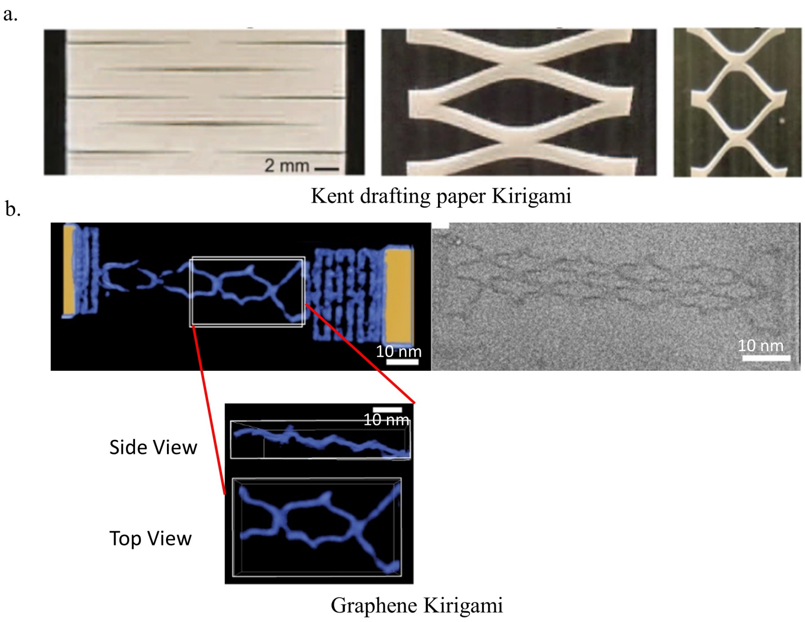

Figure 1.2: Stretchable Kirigami
a. Drafting Paper Kirigami [2] | b. Graphene Kirigami [3]

Examples of morphable and transformable structures using kirigami are shown in Figure 1.3. Here, compressive forces are applied at the end tabs of silicon nanomembranes with specialised cuts. These nanomembranes then morph into a desired 3D pattern.

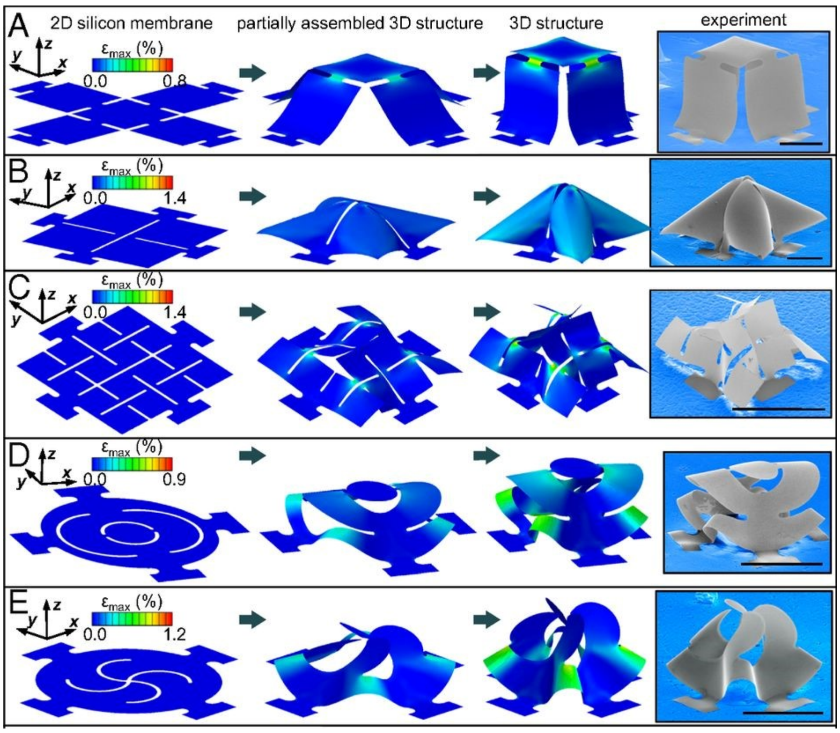

Figure 1.3: Morphable and Transformable Kirigami [4]
Compressive forces applied at the edge tabs lead to shape morphing for silicon nanomembranes.
Scale bars: A–E, 200 μm

These research studies have shown that morphable kirigami 3D patterns can be formed without folding. Instead, using planar sheets with an array of cuts is sufficient.

What is a Lattice? How is it relevant to Kirigami Structures?

A lattice is a regular and repeated arrangement of unit cells. A unit cell is the smallest unit of a lattice, representing the periodic repeating arrangement. If a periodic array of cuts is made on a planar sheet, the shape and size of an individual cut will represent a unit cell, and the corresponding sheet in which the cuts are made will represent the lattice. Examples of such lattices can be seen in Figure 1.4.

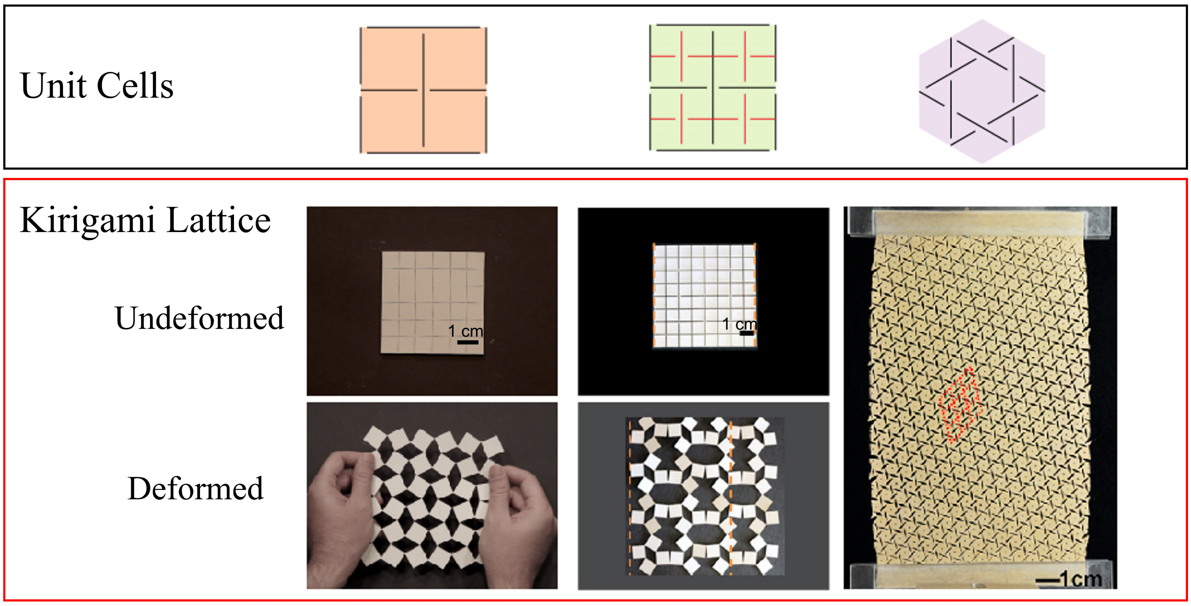

Figure 1.4: Kirigami Lattice Structures [5–7]

These lattice surfaces generated by making the periodic cuts are kirigami lattice structures. As seen in Figure 1.4, a variety of unit cell cut types are possible for kirigami lattice structures. The type of cut unit cell chosen would depend on the desired response expected from the resulting kirigami structure.

1.3. Kirigami Metasurfaces
What are they? How do we define them?

The use of kirigami in structural applications primarily stems from the potential to program the mechanical response of a material [28]. As shown in the previous sections, this can be done in the form of cuts made, in a periodic array of unit cells, on planar surfaces to allow for the creation of hierarchical and morphable metamaterials [29]. These kirigami lattice structures now represent **kirigami metasurfaces** as they allow for mechanical properties that differ from the actual mechanical property of the material, such as greater apparent breaking strain or a negative Poisson ratio [29, 30]. The mechanical properties of such metamaterials can be controlled by varying the orientations of the cuts on the planar sheet.

To summarize, a definition for kirigami metasurfaces can be given as follows:

"A kirigami metasurface is a flat elastic sheet perforated with an array of patterned cuts."

This definition is adopted from a research journal blog [16], which focuses on the use of kirigami metamaterials for mechanical applications.

1.3.1. Types of Kirigami Metasurfaces

A brief description of how lattice-based kirigami metasurfaces behave under an applied load can be given as follows. When a uniaxial tensile load is applied, the initial deformations are localized around the hinges separating adjacent cuts. Then, based on the cut unit cell geometry and the ratio of the hinge width to sheet thickness, the mechanical behaviour of the metasurface changes. A hinge in a kirigami metasurface is the solid space between subsequent cuts. An example can be seen in Figure 1.5. A more detailed description of the mechanical behaviour and the mechanics involved will be provided in chapter 2.

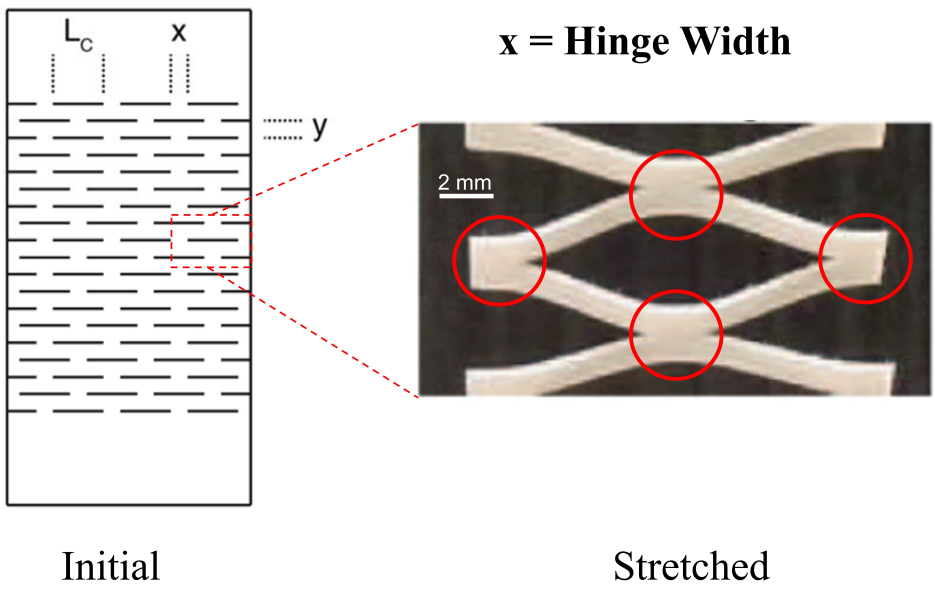

Figure 1.5: The hinge locations and their widths, highlighted in a linear cut pattern kirigami metasurface [2, 8]

Based on the mechanical response observed, kirigami metasurfaces are classified as either:

1. Planar kirigami metasurfaces
2. Buckling-induced kirigami metasurfaces

Planar Kirigami Metasurfaces

As the name suggests, planar kirigami metasurfaces display a deformation behaviour primarily in the in-plane direction. This class of metasurface is primarily limited to unit cells containing mutually orthogonal cuts. They display highly stretchable behaviour and are monostable. If kept within their loading range, they retain their undeformed configuration after removing the load. The main types of planar kirigami metasurfaces can be seen in Figure 1.6.

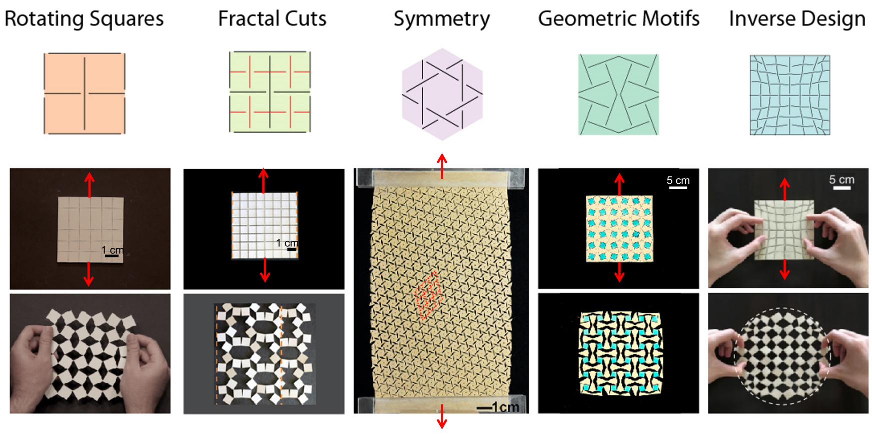

Figure 1.6: Planar Kirigami Metasurfaces [5–7, 9, 10]

They are categorized based on the unit cell geometry. The behaviour of these metasurfaces can be briefly described as follows:

Rotating squares are created using an array of orthogonal linear cuts in a thick elastic sheet. This type of metasurface exhibits an auxetic behaviour characterized by an effective Poisson's ratio of -1.

Fractal cuts: These are generated by when cuts divide the unit cells into self-similar domains, these domains can continuously be cut to create a hierarchical kirigami metasurface. These hierarchical cut patterns into material based on the rotating squares generate extremely large strains and shape changes [5, 6].

Symmetry: These types of cut geometries expand upon the concept of rotating squares. The concept involves a number of lines placed over a grid with small spacings between them to preserve the connectivity of the structure. A similar template can be applied to other grids and symmetry groups to create different designs for rotating units. For example, in Figure 1.4, the symmetry unit cell cut allowed for a planar kirigami structure with nearly isotropic negative Poisson's ratio [7].

Geometric motifs: This cut pattern is based on architectural geometric motifs. These cut patterns are based on a variant of rotating squares and triangles. They exhibit simultaneous auxetic behaviour and multistability [10]. The example shown in Figure 1.4 allows for the locking of the deformations after the load is released.

Inverse design: These cut patterns are generated to enable shape-shifting from an initial geometry into a target shape. The target shape is the starting point and computer algorithms generate a kirigami pattern from the rotating squares unit cell to reach the final target shape [9].

Buckling-Induced Kirigami Metasurfaces

This class of metasurfaces are not limited to in-plane behaviour. Applying a uniaxial tensile load on this type of metasurface causes their ligaments to buckle out-of-plane. These kirigami metasurfaces are not only highly stretchable, but their out-of-plane deformation leads to the formation of 3D patterns. In this way, they differ from planar kirigami metasurfaces that primarily deform in-plane. Another way in which they differ from planar kirigami metasurfaces is their stability. Buckling-induced kirigami metasurfaces can exhibit multistability. Different deformation modes can be dominant depending on the spacing and size of the cuts in a particular cut pattern. Numerous types of buckling-induced kirigami metasurface cut patterns are possible. Figure 1.7 shows some common types.

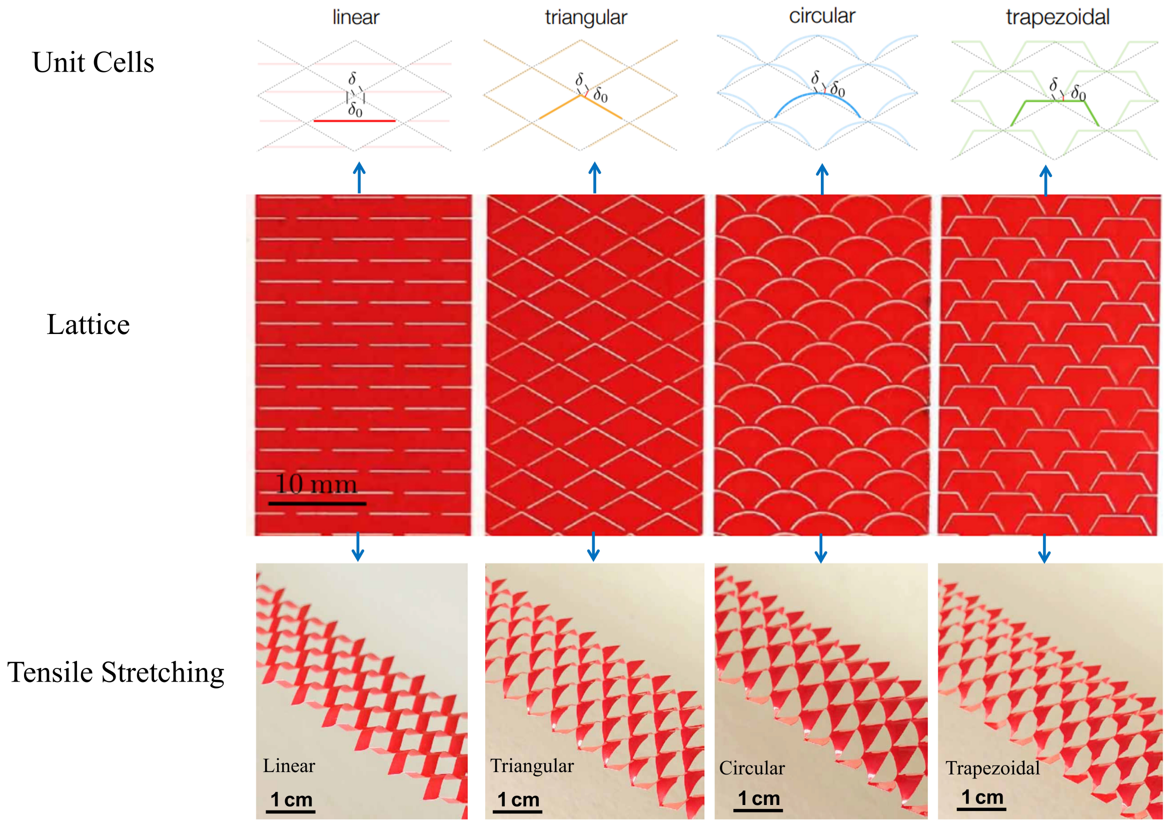

Figure 1.7: Buckling-Induced Kirigami Metasurfaces [11]

In a perfect sample, there is no preferential direction for the out-of-the-plane popping of the unit cells due to the symmetry of the cut pattern. However, the presence of imperfections in an actual may lead to a non-uniform distribution of unit cell popping. These stabilities and popping directions will be explored more deeply in chapter 2.

Another critical consideration for buckling-induced kirigami metasurfaces is sheet thickness. Thin planar sheets allow for the exploitation of local elastic instabilities at the hinges, allowing the sheets to transform into complex 3D configurations upon stretching [29]. Therefore, the thinner the sheets used, the easier it is to induce buckling and allow for out-of-plane deformation.

1.3.2. Materials and Techniques predominantly used to manufacture buckling-induced kirigami metasurfaces

Since a low sheet thickness is preferred, malleable materials such as steel or stiff polymeric materials like polyester, that can be drawn into thin sheets are generally used [11, 14, 28, 31]. An array of cuts, embedded in these thin, flat sheets, allow for their transformation into kirigami metasurfaces. These cuts are usually made using laser cutting, as this subtractive process allows for precise and minuscule cuts.

A caveat of using such stiff materials is their low-breaking strains. Kirigami metasurfaces made using such materials have a low critical strain. This low critical strain restricts their allowable strain range of operation. Therefore, their applications are often limited to low-strain applications.

A caveat of using laser cutting is that it can cause warping around the cut edges and change the material properties locally due to heating. These defects can unintentionally bias the direction of popping of the unit cells.

1.4. Using Tougher Materials and Additive Manufacturing

Compared to stiff materials, tougher materials such as elastomers would allow for higher critical strains. This would also mean a greater allowable strain range of operation. Thin sheets made of stiff materials are more likely to deform plastically at the hinges during a strain cycle due to stress concentrations from potential defects. Tougher materials are more forgiving in this regard and would allow for greater structural integrity at the hinges during a strain cycle.

Additive manufacturing (AM) is a process where geometries are built up in a layerwise fashion. When AM is applied to kirigami metasurfaces, the cuts are built into the design while manufacturing. Compared to subtractive processes like laser cutting, where localized melting is used to generate the cuts, in AM, no material is taken away. This allows for greater manufacturing control of the cut edges. Hence, the use of tougher materials and AM make an interesting use case for high-strain, controllable kirigami metasurfaces.

1.5. Aerodynamic Applications: Flow control using Surface Texturing

Surface texture is defined as the local deviation of a surface from a perfectly flat plane [32]. In flow applications, surface texturing is often used to reduce skin friction and provide a slip condition at the surface. This surface texturing mechanism has also been observed in biological species. An extensively studied example of this is the shortfin Mako shark, whose skin is covered with a series of overlapping denticles [12, 13]. The tiny flat V-shaped scales, shown in the top view of Figure 1.8, are called the denticles.

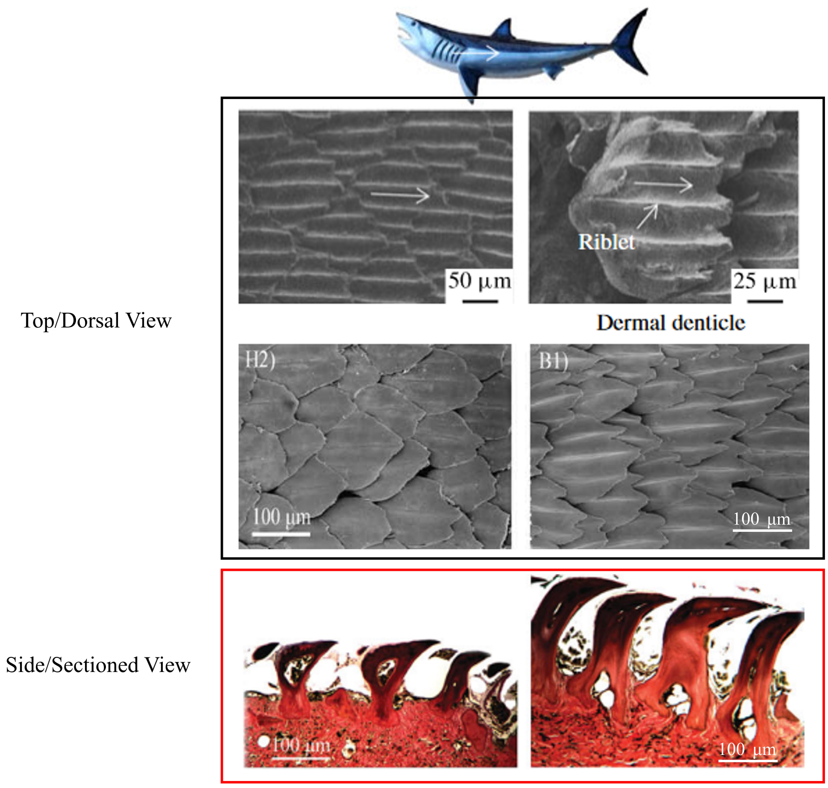

Figure 1.8: Shark Scale Morphology [12, 13]
The top and sectioned side view of the scales/denticles are shown

These denticles have been observed in locations of the shark body where the fluid flow exhibits an adverse pressure gradient past the location of maximum girth. At these locations, the fluid is more prone to flow separation. The denticles exhibit a unique geometry combining streamwise riblets with a flexible scale structure, which can bristle and change the denticle angle [33]. Both these components have been shown to provide drag reduction. These scales are compared to a bristle trapping flow that is reversing in direction, thus preventing flow separation [34].

Similarities between shark skin and kirigami metasurfaces

These flexible shark scales and their ability to vary their angle of attack with respect to the incoming water stream help in the flow steering. One thing to note is that angular cut pattern, buckling-induced kirigami metasurfaces, as shown in Figure 1.9, are quite similar in design and function to these shark scales. They morph from a planar to a 3D shape upon loading and do so in a controlled manner.

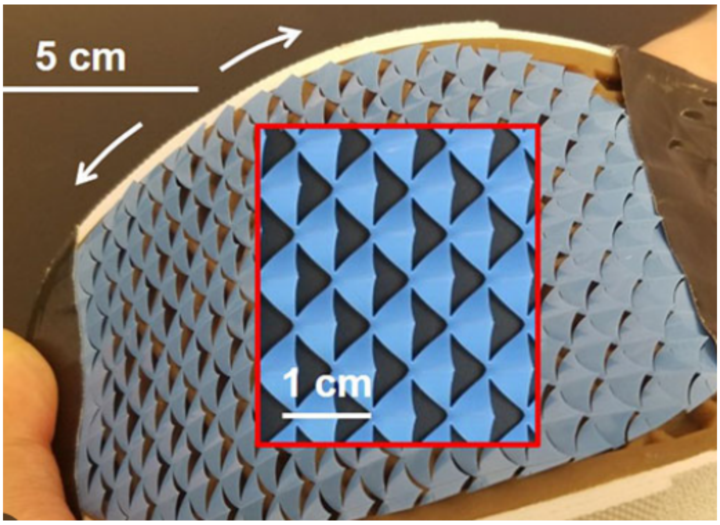

Figure 1.9: Angular cut pattern kirigami metasurfaces used as shoe grips [14]

On observing these similarities between kirigami metasurfaces and hydrodynamically efficient shark skin, the following questions come to mind:

- Can these morphing kirigami metasurfaces be used for *aerodynamic applications*?
- Can they also allow for flow control?
- And what kind of drag forces can they generate?

2

Literature Review

This chapter reviews the existing literature with the objective of summarizing the work that has already been done in the research space. It also provides a basis for the current work being carried out in this thesis. This literature review will focus on research pertaining to kirigami metasurfaces created using an array of cuts on planar sheets and **without the use of folding**. Another focus will be **buckling-induced kirigami** metasurfaces subject to **tensile loading**.

The chapter starts by explaining how such a kirigami metasurface is created and the mechanics behind its out-of-plane transformation behaviour.

2.1. Structural Mechanics of buckling-induced kirigami metasurfaces

A pattern of cuts made to a planar sheet induces a mechanical instability that creates a kirigami metasurface. Exploiting these local elastic instabilities allows the transformation of the metasurfaces from planar 2D into a 3D pattern when stretched. These instabilities also lead to a bistable configuration that can either cause a clockwise or counterclockwise out-of-plane deflection. This directionality can be biased by applying an initial load in the desired direction [8, 21], as shown in Figure 2.1.

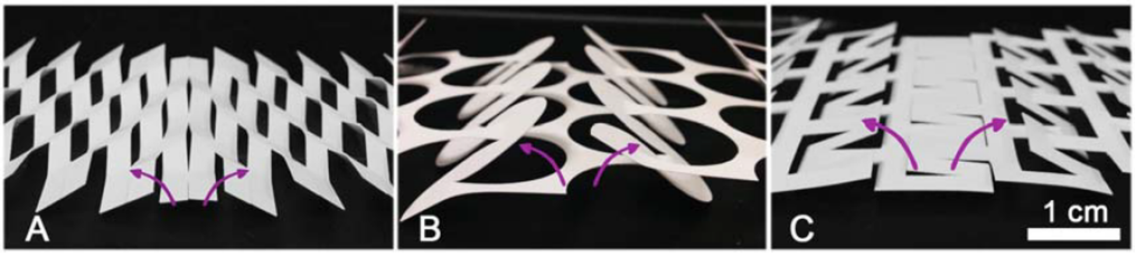

Figure 2.1: The system chooses a favourable configuration by bending out-of-plane. It can do so in either clockwise or counter-clockwise direction [8]

2.1.1. Why do mechanical instabilities occur?

Thin structures are highly susceptible to instability, primarily due to their tendency to deform by bending [35]. The simplest reduced-order model of a thin structure is a rod. To understand how a thin structure deforms, let us consider the strain energy of this thin elastic rod. Reduced-order models of slender structures (rods, plates and shells) generally use a standard form: a stretching energy $\mathcal{U}_s$, which accounts for extension or compression of the middle surface of the rod and is linear in the rod thickness, h, and a bending energy $\mathcal{U}_b$, which accounts for the curvature change of the deformed rod and is dependent on h^3. The strain energy of the thin rod can then be given as [35]:

$$\mathcal{U} \sim \underbrace{Y \int \varepsilon^2 \, \mathrm{d}\omega}_{\mathcal{U}_s} + \underbrace{B \int \kappa^2 \, \mathrm{d}\omega}_{\mathcal{U}_b} \tag{2.1}$$

where $Y = Eh/\left(1-\nu^2\right)$ is the stretching rigidity, $B = Eh^3/\left[12\left(1-\nu^2\right)\right]$ is the bending rigidity, ν is the material's Poisson's ratio, and $\mathrm{d}\omega$ is the area element. Comparing the bending and stretching energies, we see that $\mathcal{U}_b/\mathcal{U}_s \sim h^2(\kappa/\varepsilon)^2$, where κ is the average curvature induced by bending the rod, and ε is the average strain induced when the rod is stretched.

Because the rod is thin, we can approximate that the average strain, ε, is extremely small.This indicates that the bending energy is much lesser than the stretching energy. Therefore, it would be much **easier to bend a thin structure than it is to stretch it**, as the system favours lower energy.

This insight helps explain why thin structures are prone to instability. If you try to shorten the length of a thin rod by compressing it, the **rod would much rather bend than be compressed, and to bend, it must buckle**.

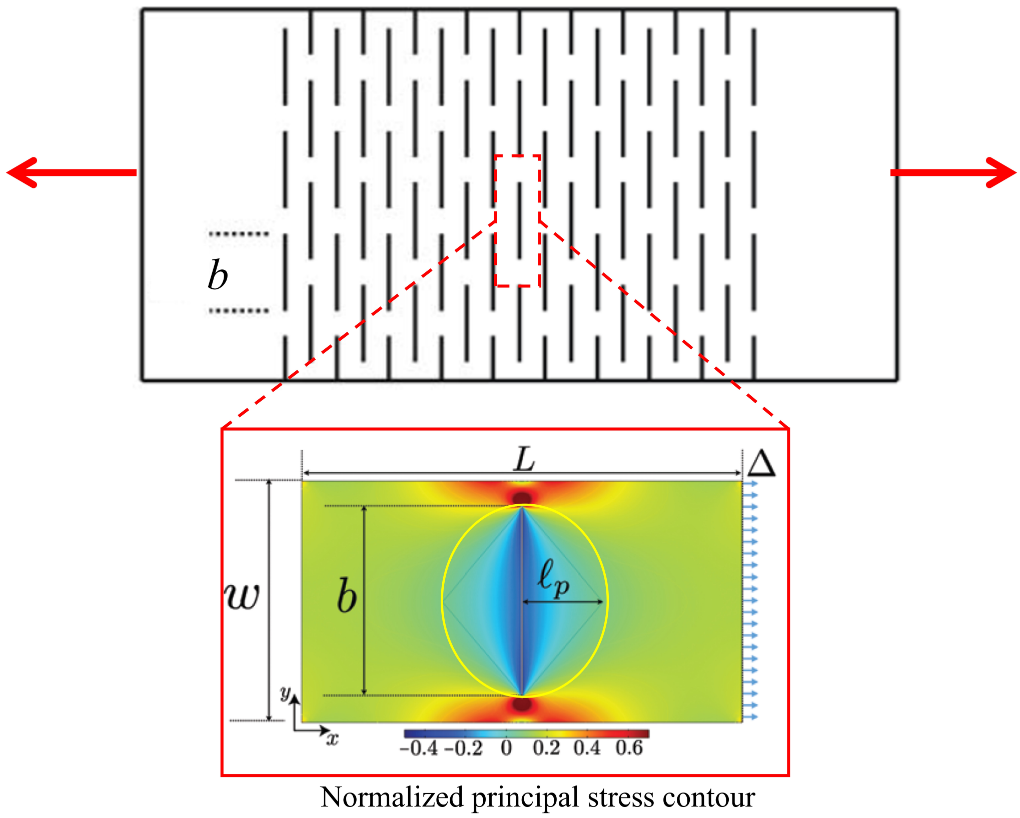

Figure 2.2: Principal stress contours on single cut of linear cut pattern kirigami metasurface [15]

Looking at the principal stress contours of the single cut in Figure 2.2, we can observe that there is an in-plane compressive zone along and around the internal boundary along the cut, highlighted by the yellow ellipse at the stress contours, in Figure 2.2. If we assume the longitudinal edges, that bound this cut, as thin rods subjected to a compressive force. We can then understand why the rods would much rather bend than be compressed, as explained previously. For this bending to occur, the rods must first buckle.

Due to this buckling behaviour, the overall lattice structure is energetically metastable with two local minima. It therefore exhibits a **snap-through** behaviour [17]. Each local stable state is associated with a corresponding structural configuration. This structural configuration is based on geometric specifics of a cut pattern. By applying an external perturbation or biasing, we can manipulate the unit to switch between the two stable configurations.

2.1.2. General Deformation Behaviour

The general deformation behaviour of buckling-induced kirigami metasurfaces can be explained using the simplest unit cell cut type. The unit cell geometry for this cut pattern can be seen in Figure 2.3. It consists of linear parallel cuts hexagonally arranged perpendicular to the loading direction. Due to its multistability, the structure can adopt multiple shapes when stretched by varying the spacing and dimensions of the cuts.

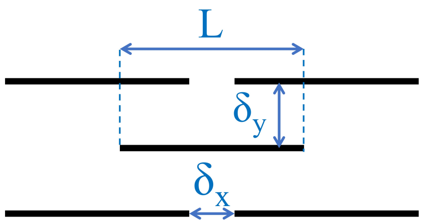

Figure 2.3: Linear cut pattern kirigiami unit cell

The tensile response of kirigami metasurfaces with linear cut patterns consists of three regimes, as demonstrated by Isobe and Okumura [3], consists of three deformation regimes. These regimes can be seen in Figure 2.4.

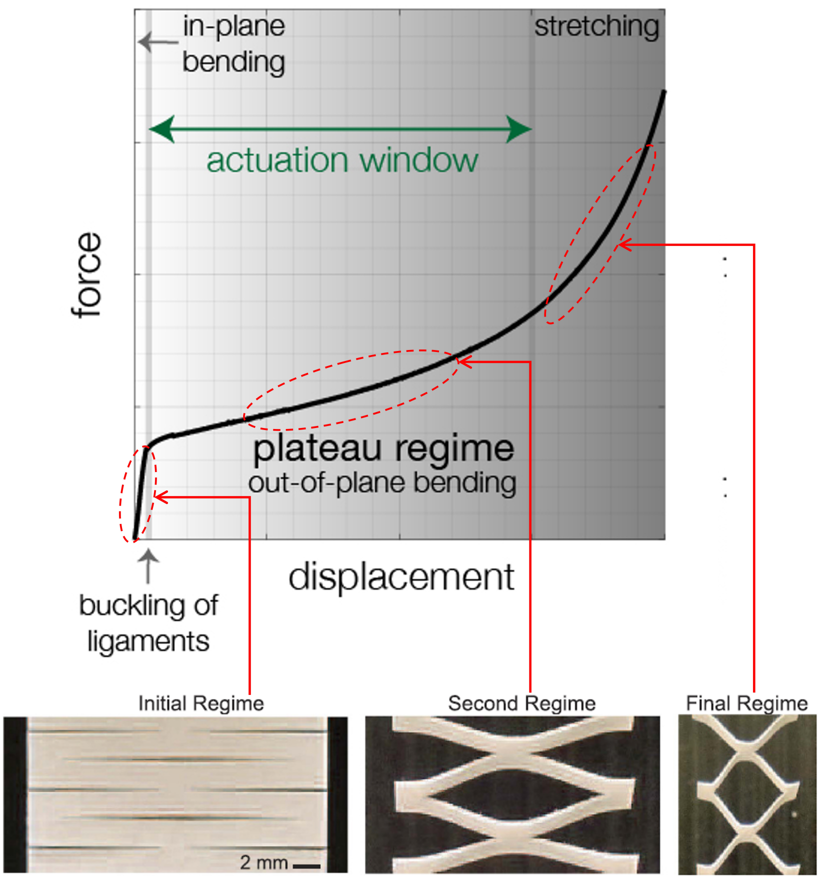

Figure 2.4: Force-Displacement response of buckling-induced kirigami metasurfaces [3, 16]

In the initial regime, the response is linear, and hinges bend in-plane under small, applied deformation without rotation. As shown in Figure 2.5, the in-plane bending causes the centre line of the segment to deflect in-plane by a distance of δ_1.

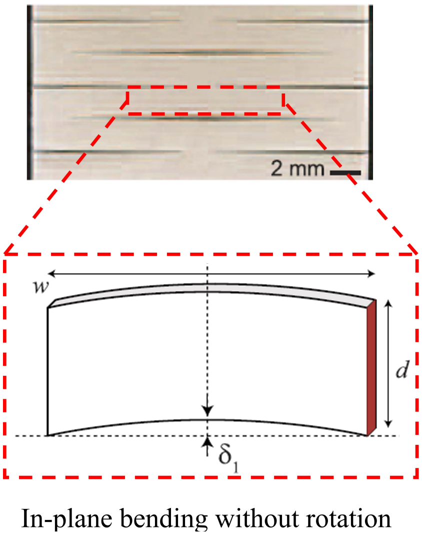

Figure 2.5: In-plane bending without rotation in the first regime [3]

In the second regime, the response shows a sudden departure from linearity to a large plateau region caused by out-of-plane deformation with rotation. As shown in Figure 2.6, the out-of-plane bending causes the centre line of the segment to deflect out-of-plane by a distance of δ_2 and rotate by an angle θ. This region starts as the ligaments begin to buckle, as demarcated by a line in Figure 2.4.

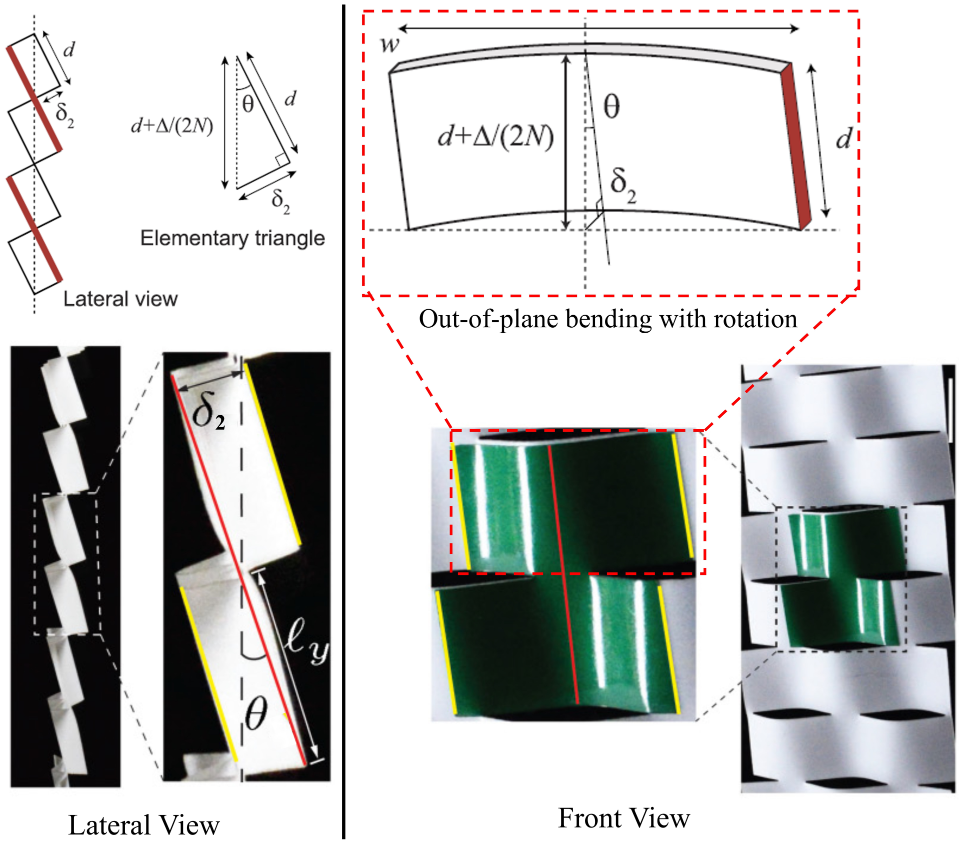

Figure 2.6: Out-of-plane bending with rotation in the second regime [3, 17]
Front and Lateral views

At the final regime, for a large enough applied deformation, the force rises again, and the deformation mechanism of hinges changes from bending to stretching. At this stage, the stress rises sharply, and localized zones of intense plastic strain develop at the hinges.

A key thing to note is that almost all buckling-induced kirigami metasurfaces share the same deformation behaviour pattern. This makes them a robust platform for designing programmable structures with predictable responses irrespective of their cut geometries [16].

Deeper investigations of the mathematics and local mechanics behind linear cut pattern kirigami metasurfaces [16]

Several mechanicians have investigated the local mechanics of this cut pattern type and related them to this kirigami metasurface's global behaviour. Dias *et al.* [15] studied the connections between this kirigami pattern and the mechanics of a single, non-propagating crack in a sheet. Yang *et al.* [17] proposed an excess angle cone as the most fundamental geometric building block of buckling-induced kirigami metasurfaces with a linear cut. Investigations were also done correlating the types of buckling configurations to the cut pattern geometric parameters [17]. Sadik and Dias [36] used a reduced two-dimensional plate model of a thin circular disk with a radial slit and unravelled its deformation map following the opening of the slit and the rotation of its lips. Sadik *et al.* [37] followed up and further expanded this work using stretchable creased solutions. These works explain the non-linear mechanics of this type of kirigami metasurface. These fundamental behaviours are governed by the nonlinear mechanics of thin frames [35, 38]. They can be used to tune and control the direction of popping and program the multistability of the kirigami metasurface.

These, however, are not required for the scope of this thesis work. Beam theory and beam approximations are sufficient to theoretically derive the global force and stiffness of a symmetric buckling-induced kirigami metasurface. Hence, they will be employed in the upcoming subsections.

2.1.3. Linear Cut Pattern Kirigami Force Analysis

Linear cut pattern kirigami are single incision patterns comprising parallel cuts, used to make a kirigami metasurface as shown in Figure 2.7. To analyse the forces of such a kirigami system, we assume beam deflection to predict the forces induced due to the bistable configuration. The characteristic geometric parameters are represented as follows. L_c is the characteristic cut length, x and y represent the distance between subsequent cuts in the x and y directions.

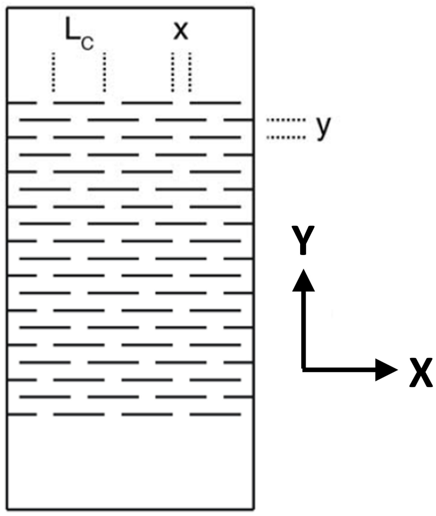

Figure 2.7: Linear cut pattern Kirigami Geometry[8]

When this sample type is stretched in the in-plane y-direction, the instabilities created because of the cut geometry, cause a shear effect along the length of the cut. Therefore, there is sample elongation accompanied by a decreasing width. As shown in Figure 2.8, the highlighted section, consisting of a portion of the cut length and the subsequent row, are approximated as a set of two beams connected in series.

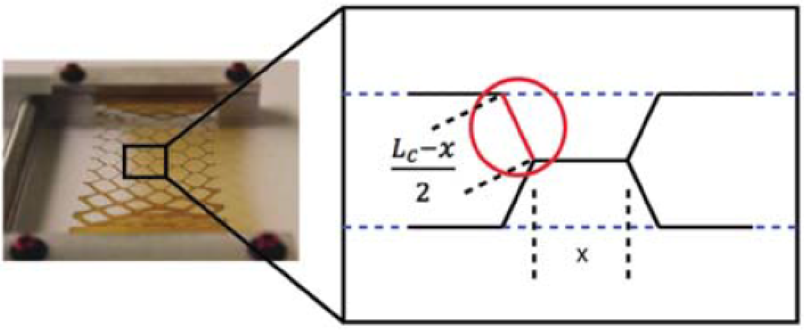

Figure 2.8: Beam Approximation [8]

The single section circled in Figure 2.8 is approximated as two smaller joined beams of lengths $\frac{L_C-x}{4}$, as shown at the left of Figure 2.9.

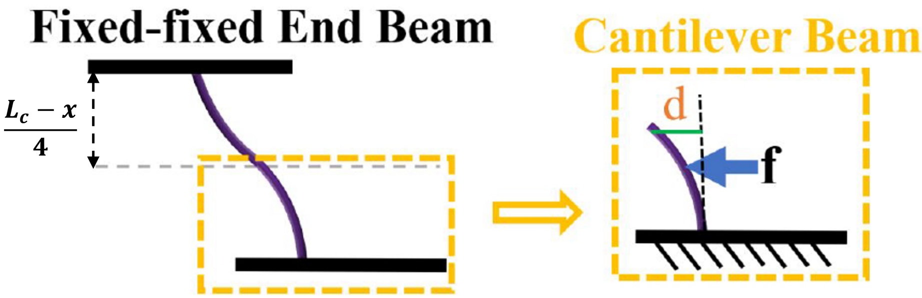

Figure 2.9: Free body diagram of the fixed-fixed end beam and cantilever beam model [18]

Each of these smaller fixed-fixed end beams can be assumed as single free-end cantilevers joined together at the free ends and fixed at the other end as shown in Figure 2.9.

Now that these approximations are made, we can use beam theory to find the deflection (d) and the stiffness (k) of each beam using the following equations:

$$d = \frac{fL^3}{3EI} \tag{2.2}$$

$$k = \frac{EI}{L^3} \tag{2.3}$$

where f is the force acting on a beam, L is the beam length, E is the Young's modulus of the material used, and I is the moment of inertia, given by:

$$I = \frac{wt^3}{12} \tag{2.4}$$

where w is the beam width, and t is the thickness in the direction of deflection. Therefore, deflection is now given as:

$$d = \frac{4fL^3}{Ewt^3} \tag{2.5}$$

Since the two beams are connected to each other in a series configuration, the total beam deflection is given as:

$$d_{\text{beam,total}} = d_{\text{beam 1}} + d_{\text{beam 2}} = 2d_{\text{beam 1}} = \frac{8fL^3}{Ewt^3} \tag{2.6}$$

From Equation 2.5, we can rearrange the equation to solve the force on the beam, as a function of the deflection:

$$f = \frac{dEwt^3}{4L^3} \tag{2.7}$$

If we substitute the characteristic geometric parameters of the kirigami unit cell, we get the beam length as L = $\frac{L_C - x}{4}$. Substituting this beam length and the total beam deflection from Equation 2.6 in Equation 2.7, we get the force on the beam as:

$$f_{\text{beam}} = \frac{Eyt^3}{4\left(\frac{L_C - x}{4}\right)^3} = \frac{8Edyt^3}{(L_C - x)^3} \tag{2.8}$$

To calculate the force acting on the entire kirigami metasurface, we consider the beams along the width (x - direction) and the length (y-direction) of the sample. The beams along a particular row (in the x-direction) are connected in parallel. The force per row is given as:

$$f_{\text{row}} = N_{B'} f_{\text{beam}} \tag{2.9}$$

where N_B is the number of beams per row, in the x-direction. In the y-direction, beams from each row are connected to the next row in series. Now, the total force is given as:

$$\frac{1}{F_{\text{Total}}} = \frac{N_{\text{rows}}}{f_{\text{row}}} \tag{2.10}$$

where N_R is the number of rows along the y-direction. Combining all the equations shown above, we obtain the total force in terms of the characteristic geometric parameters of the kirigami unit cell.

$$F_{\text{Total}} = \frac{f_{\text{row}}}{N_{\text{rows}}} = \frac{N_{B'} f_{\text{beam}}}{N_{\text{rows}}} = \frac{8dN_{B'}Eyt^3}{N_{\text{rows}}\,(L_C - x)^3} \tag{2.11}$$

Using the above total force equation and Equation 2.3, we get the total stiffness (K_{Total}) as:

$$K_{\text{Total}} = \frac{N_B}{N_{\text{row}}} k = \frac{16N_B Eyt^3}{3N_{\text{row}}\,(L_C - x)^3} \tag{2.12}$$

Using these equations [2.11, 2.12], buckling-induced kirigami metasurfaces can be designed based on the desired mechanical response. This can be done by optimizing the material choice and the characteristic geometric parameters of the cut pattern. These beam approximations can also be adapted to other types of cut patterns.

2.1.4. Angular Kirigami Cut Pattern Force Analysis

As stated in the previous section, the beam approximations for the linear cut pattern can be adapted for this angular cut pattern. This is done by adapting the characteristic geometric parameters shown in Figure 2.7 to those that define an angular kirigami cut pattern. We see this adaptation in Figure 2.10.

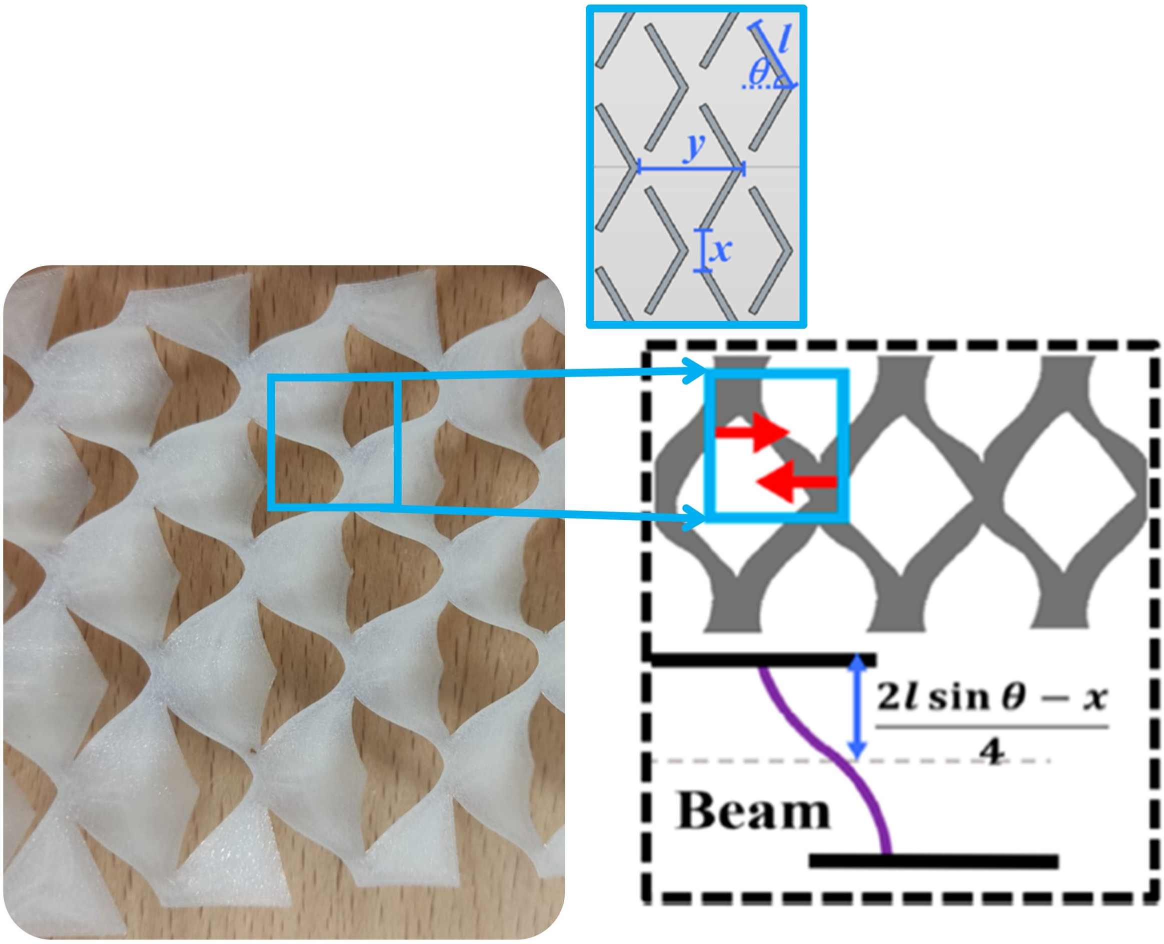

Figure 2.10: Schematic diagram of the beam model with the characteristic geometric parameters of a triangular unit cell [18, 19]

The main difference from the previous cut pattern type is the adaptation of the characteristic cut length (L_c), from Figure 2.7, which is now $2l\sin\theta$ for the triangular cut pattern. The beam length therefore changes from $\frac{L_C-x}{4}$, as shown in Figure 2.9, to $\frac{2l\sin\theta-x}{4}$, as shown in Figure 2.10.

Substituting the adapted characteristic cut length in Equation 2.11 and Equation 2.11, the total force and the total stiffness for this kirigami cut pattern type, is now given as:

$$F_{\text{Total, Triangular}} = \frac{N_B}{N_{\text{row}}} f = \frac{8N_B E d y t^3}{N_{\text{row}}\,(2l\sin\theta - x)^3} \tag{2.13}$$

$$K_{\text{Total, Triangular}} = \frac{N_B}{N_{\text{row}}} k = \frac{16N_B E y t^3}{3N_{\text{row}}\,(2l\sin\theta - x)^3} \tag{2.14}$$

These total equations [2.11, 2.13], used to analyse the forces on these kirigami metasurface structures, are only theoretical. In experimental practice, several factors, such as uneven cut finishes, material defects and unaccounted edge effects during testing, could contribute to a higher loading when measured experimentally.

2.1.5. Explaining the Buckling Behaviour

These equations relating the force to displacement do not consider the deformation experienced by the whole sample due to buckling and torsion. Instead, these equations show how the force is affected by the unit-cell geometry [21].

When the applied in-plane tensile load on the kirigami system, exceeds the critical buckling load at the hinge section (represented as beams in the previous section), the initial planar sheet starts to deform. Exceeding the critical buckling load, marks the onset of buckling, where the initial elastic linear regime transitions to the second, nonlinear regime [21]. And as a result of mechanical bistability generated due to cut pattern, the kirigami metasurfaces display an out-of-plane deflection during this deformation process.

2.2. A Review of the Existing Work

A short preface before going forward. As seen in section 2.1, a buckling-induced kirigami metasurface can be created using a pattern of cuts that induce mechanical instability in a planar sheet. Now, the types of kirigami cut patterns are infinite and are only restricted by one's imagination. This literature review will focus on a few types of cut patterns extensively used in research works and will highlight the reasons why such cut patterns are primarily used.

2.2.1. Research works using linear cut patterns

Linear cut patterns encompass the types of kirigami cut that consist of single incision parallel cut patterns aligned perpendicular to the applied tensile forces. These cuts are usually placed in a centred rectangular arrangement, as shown in Figure 2.1.

An application of such a cut pattern was used to enhance film adhesion in Zhao *et al.* [20]. This work used silicon-based film substrates to create a kirigami film with a linear cut pattern. A linear cut pattern kirigami , along with soft silicon material, was used for this application as this combination greatly enhanced the critical strain the film would detach from the substrate. This critical strain is essential, as film adhesion to substrates is usually prone to delamination failure when the substrates are highly deformed.

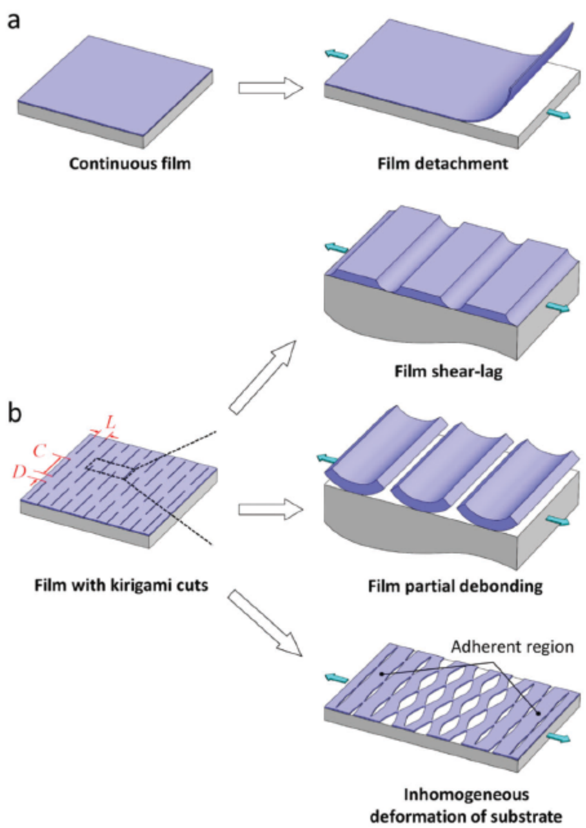

Figure 2.11: Schematic diagrams of a.) Film detachment of a continuous film
b.) Use of Kirigami cuts to enhance the critical strain for delamination and the reasons for it's better bonding [20]

Figure 2.11 a, shows how a regular, continuous film on a substrate detaches due to delamination when there is an excess deformation. Figure 2.11 b, shows how the linear cut pattern kirigami in the film enhances the film adhesiveness, owning to:

1. *The shear-lag effect of the film segments*. This reduces the energy release rate compared with the continuous film and allows the film to bear a larger stretch prior to debonding.
2. *Only a partial debonding at the film segment edges*, as highlighted at the edges in Figure 2.12.
3. *The kirigami films' compatibility with the substrates' inhomogeneous deformation.*

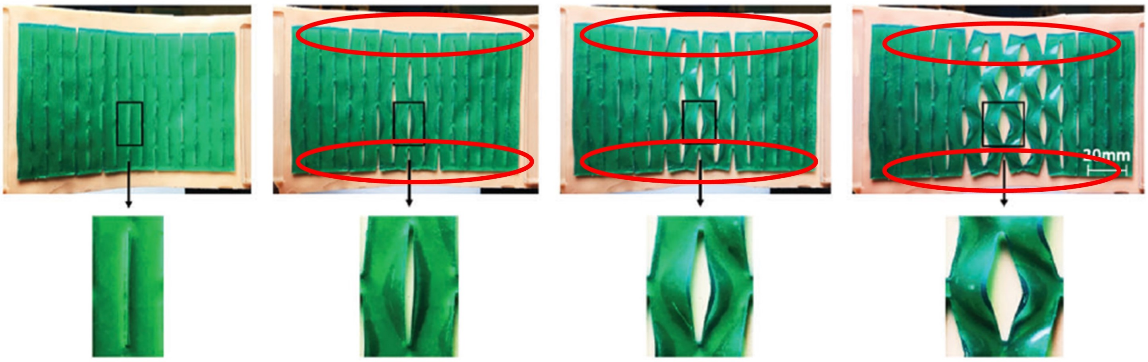

Figure 2.12: Partial debonding along the width edges [20]

As seen in Figure 2.13, the corresponding kirigami film maintains adhesion during cyclic bending of the elbow, and the continuous film detaches.

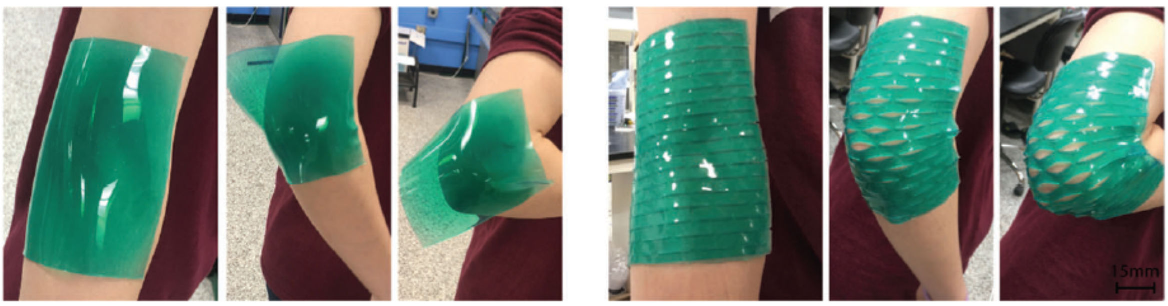

Figure 2.13: Film behaviour during cyclic bending [20]

Such linear cut pattern kirigami films undergo deformation without delaminating from the base substrate, as their ends can continuously stick to the substrate. In contrast, the regions at the centre with the linear cuts undergo a high amount of strain and deformation and adapt to the inhomogeneous deformation of the substrates. These patterns allow extensibility without plastic deformation due to the soft material used and can retain their shape when the force is removed. Their capacity for high strain allows them to adhere to the substrate. In addition, they allow for high amounts of in-plane, axial strain along the direction of the applied force. These kirigami patches were made by pouring the silicon resin into moulds. Since a soft material was used, it could be used cyclically without permanent plastic deformations.

Another research work uses linear cut pattern kirigami in the nano and micro-scale [21]. An oxygen plasma etch creates the cuts on a multilayered graphene oxide nanocomposite. This work aims to impart elasticity to the nanocomposites and increase their ultimate strain.

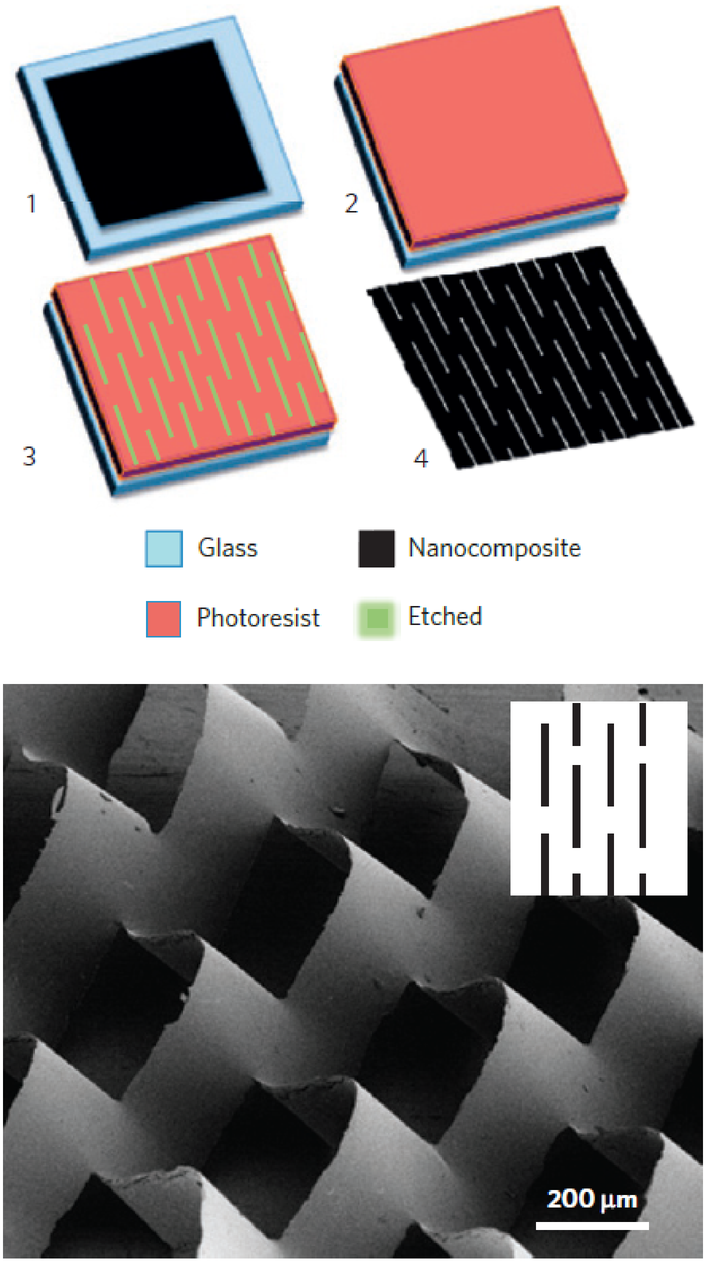

Figure 2.14: Microscale kirigami patterns [21]
Top: Schematic of the kirigami microfabrication process. (1) A nanocomposite is deposited on a solid substrate for patterning; (2) photoresist is deposited and developed; (3) an oxygen-plasma etch through the nanocomposites creates kirigami patterns; (4) nanocomposite sheet is detached from the substrate.
Bottom: Stretched Linear cut pattern Kirigami Nanocomposite

Figure 2.14 shows how the linear cut pattern was etched into the nanocomposite and what it looks like when stretched. This pattern has allowed us to develop a comprehensive description of deformation patterns taking place in the material. The original material without patterning shows a strain of 4% before failure; its deformation primarily stretches the individual nano-, micro- and macro-scale cellulose fibres within the matrix (Figure 2.15, grey curve). The dashed blue curve in Figure 2.15 curve) represents a sample, a single cut in the middle of the sample.

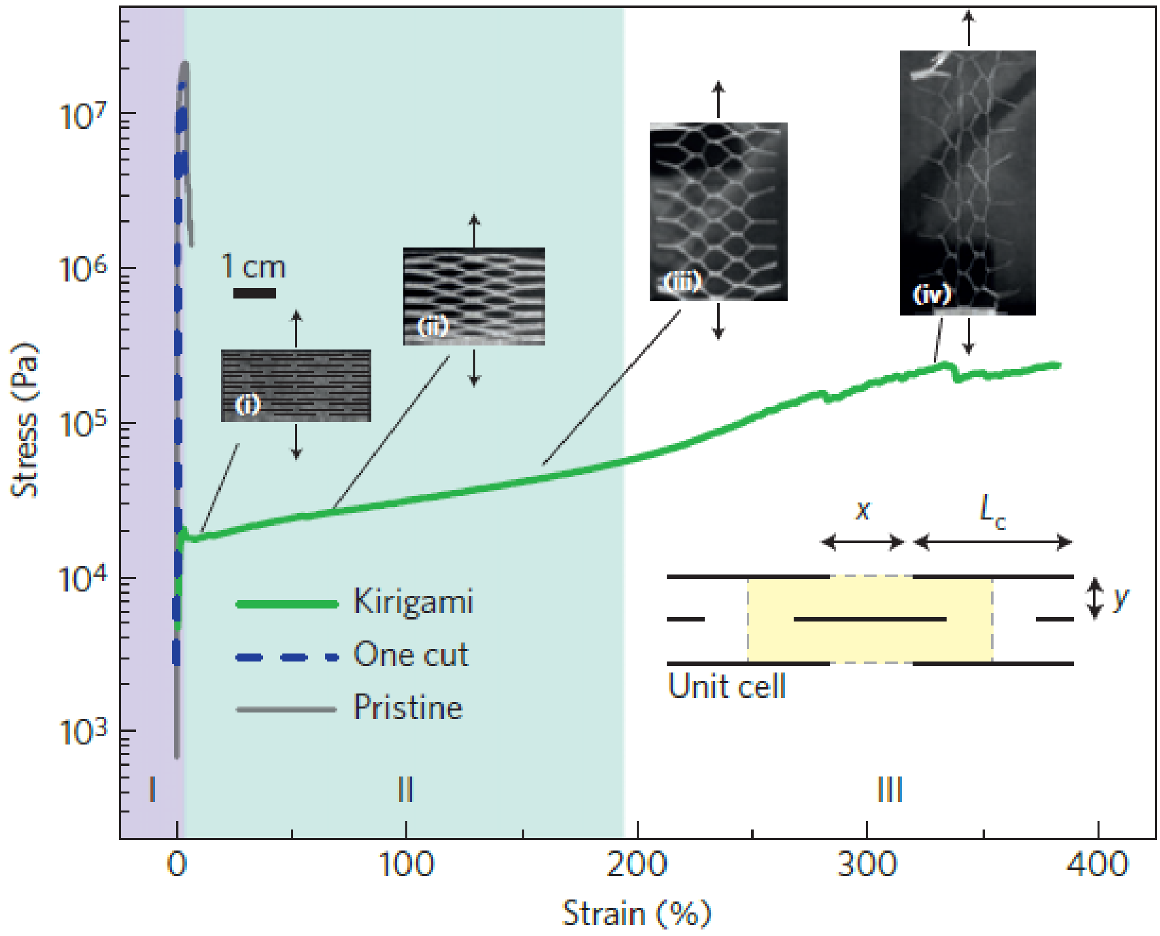

Figure 2.15: Stress–strain curves for the graphene kirigami sheet [21]

The green line in Figure 2.15 shows the behaviour of the kirigami sheet as it is stretched. In the purple section, initial elasticity at <5% strain is before the tensile force exceeds the critical buckling force. As the applied tensile force exceeds a critical buckling force, the initially planar sheet starts to deform as the thin struts formed by the cuts open up. The secondary elastic plateau shown in the green section buckling occurs at the struts as they rotate to align with the applied load, and deformation occurs out of the plane of the sample. During the deformation process, kirigami- patterned sheets exhibit out-of-plane deflection due to mechanical bistability. Finally, the alignment of the struts causes the overall structure to densify perpendicular to the pulling direction, in the white section. Failure then begins when the ends of the cuts tear and crease owing to high stress at these regions. These linear kirigami cuts impart a massive increase in the ultimate strain of the sheets. The deformation behaviour of this plot Figure 2.15, is quite similar to regimes shown in Figure 2.4

Research works using linear cut patterns and additive manufacturing

The tensile properties of a linear cut pattern, kirigami metasurface made using thermoplastic polyurethane (TPU), and Fused Filament Fabrication (FFF) are investigated in Nakajima *et al.* [22]. The impact of stacking sequence, slit size and thickness on the tensile properties was investigated. The specimens produced and their dimensions are shown in Figure 2.16. A variety of stacking sequences [from 0/90 to -45/+45], slit heights (h) [1, 1.5, 2 and 2.5 mm] and sample thickness [1, 1.5, 2 and 2.5 mm] were investigated. The dimensional specifics and the manufactured samples can be seen in Figure 2.16

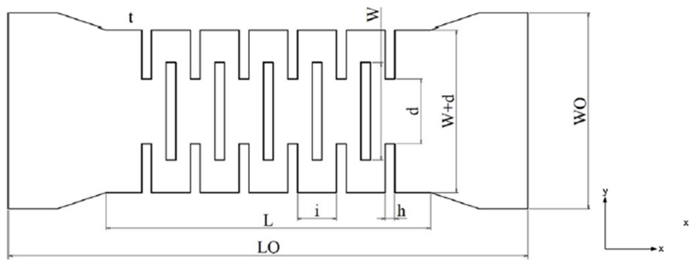

Parameter	Description	Value (mm)
W	Slit Width	15
h	Slit Height	1
i	Slit interval	5
d	Distance between slit ends	10
t	Specimen thickness	2
W + d	Width of kirigami	25
L	Length between grips	50
LO	Overall length	80
WO	Width of the grip section	30

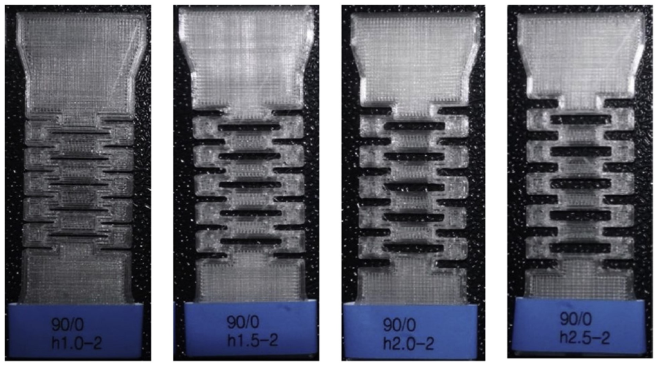

Figure 2.16: Geometrical specifics of the Kirigami sample [22]

The displacement response to the force can be seen Figure 2.17. Before the failure, these samples were only 50 mm long and could be displaced to about 90 mm. We will not go into the tensile response of the samples to the various factors tested for. Instead, it is more interesting to observe the sample deformation behaviour during testing. A high in-plane and relatively low out-of-plane strain, as seen in Figure 2.18.

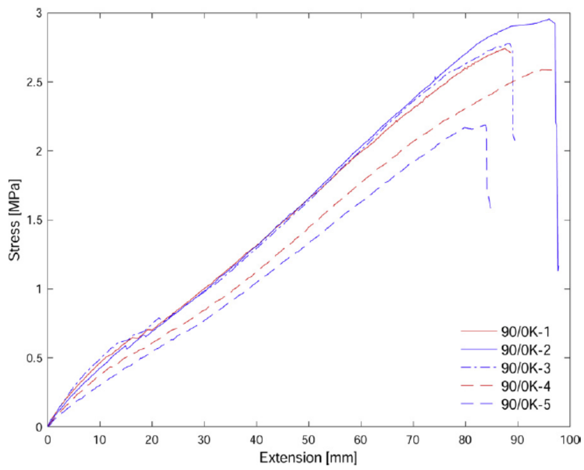

Figure 2.17: Stress-extension curve for [90/0]4 kirigami specimens [22]

This type of deformation behaviour shown in Figure 2.18 is characteristic of linear cut pattern kirigami samples. A combination of the linear cut pattern with soft and tough materials leads to a high in-plane strain response.

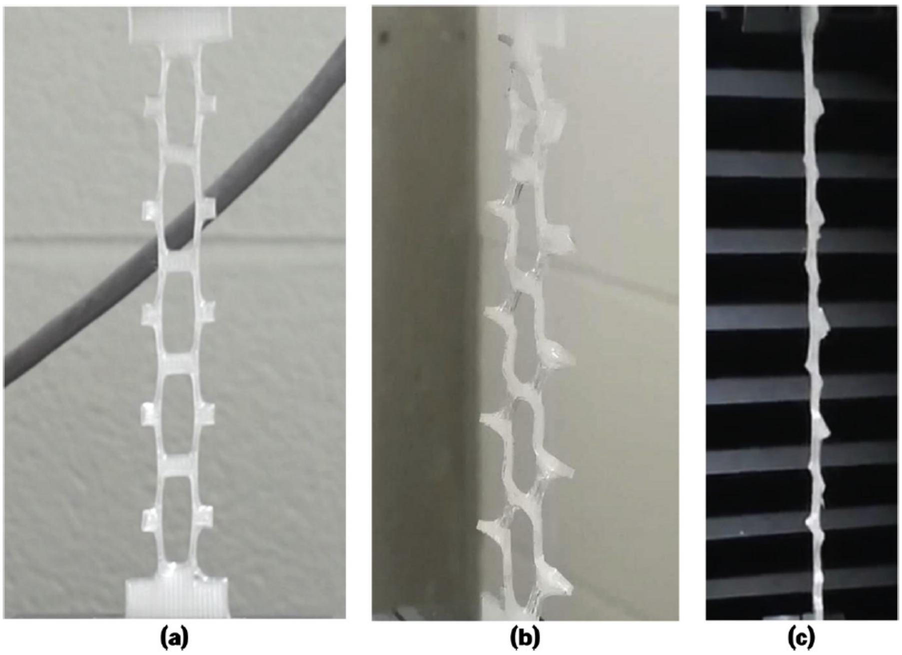

Figure 2.18: The kirigami specimen during testing, showing deformations: (a) front; (b) isometric; and (c) side views [22]

FFF was used in this work to tune the stacking sequence and infill pattern configurations for the samples. The response of these factors on the tensile strength of the specimens was then quantified.

Summarizing the linear cut pattern kirigami behaviour and its application areas

After reviewing the literature related to the linear cut pattern kirigami surfaces, we can briefly summarise their behaviour as follows:

1. Most of the deformation behaviour for linear cut pattern kirigami patterns is in the direction of the applied force, i.e. in-plane axial strain.
2. This type of kirigami surface shows a relatively low out-of-plane deformation.

If the goal of the required application is a high amount of strain for a relatively low out-of-plane displacement, this kirigami cut type is beneficial. Additionally, if softer materials are used, they would be able to retain their shape and allow for a greater elastic region. They would also be able to adapt to inhomogeneous deformations. Stiffer materials would not display resistance to any deformation in directions apart from the direction of the in-plane applied load. They have a lower elastic region and show plastic deformations at the hinges for lower strains.

2.2.2. Research works using angled cut patterns

The main inspiration for this work comes from the research carried out in [14]. In this work, out-of-plane buckling kirigami metasurfaces were designed, taking inspiration from claws and scales found in nature. The goal of this work was to dynamically modulate friction using the out-of-plane displacement of the kirigami metasurfaces. This work used a periodic array of cuts on steel sheets to generate the kirigami metasurface patches. These patches were placed on the outsoles of shoes and would buckle out-of-plane during a human gait cycle. Three types of unit cells were designed, as shown in Figure 2.19, with the design goals geared towards optimal friction on various surfaces.

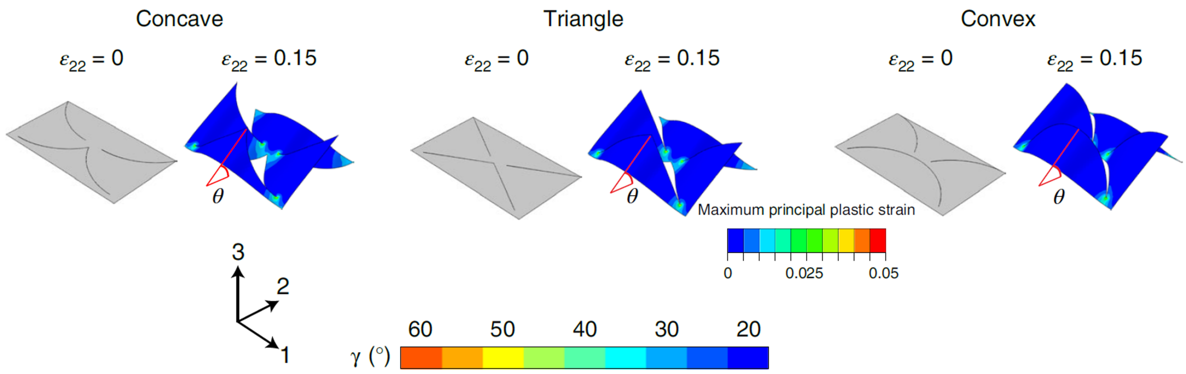

Figure 2.19: Unit cell designs and the maximum principal plastic strains [14]

A linear buckling and non-linear post-buckling finite element analyses (FEA) were carried out on a single unit cell, using periodic boundary conditions. The simulation was carried out using a uniaxial in-plane tensile strain. The critical buckling mode is identified in the linear FEA, and the non-linear post-buckling response of the system was simulated by introducing a slight imperfection (☐0.005 of the length) in the form of the critical mode into the initial geometry. The results of the out-of-plane deflection(θ) vs the in-plane strain (in Y or the 22 direction) for the different unit cell designs can be seen in Figure 2.20.

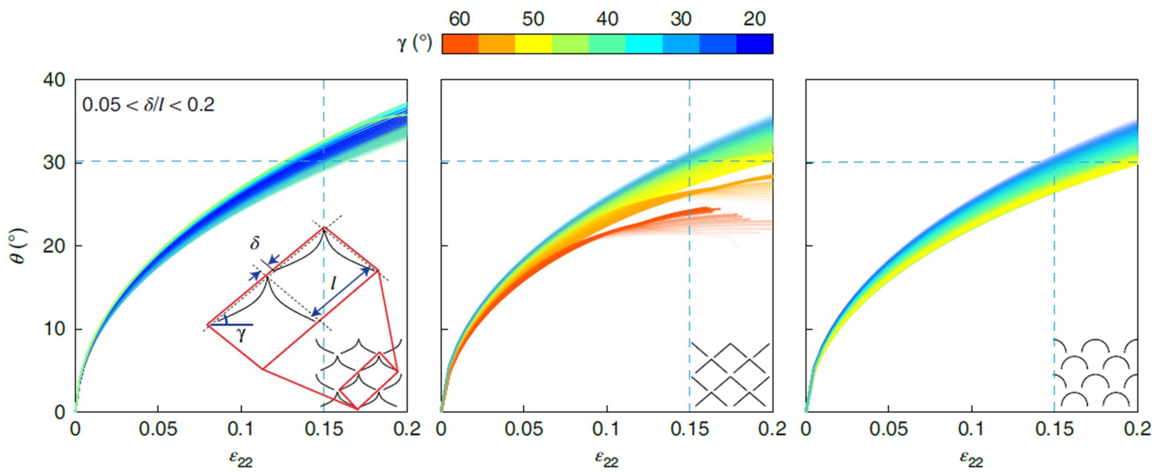

Figure 2.20: Out-of-plane deflection angle(θ) of the spikes plotted as a function of ε22 for the geometric design parameters γ and δ/l [14]

After the uniaxial tensile simulation, the normal stiffness of the spikes was found by compressing the stretched unit cells, as shown in Figure 2.19, with a rigid plate while keeping the four corners of the unit constrained in the normal direction. This estimated out-of-plane stiffness (K33) for the 30-degree cut angle (γ) spikes has been shown in Figure 2.21. It was also found that the **triangular spikes** demonstrated the greatest out-of-plane stiffness amongst the other designs. This meant it would provide the most resistance to an out-of-plane load.

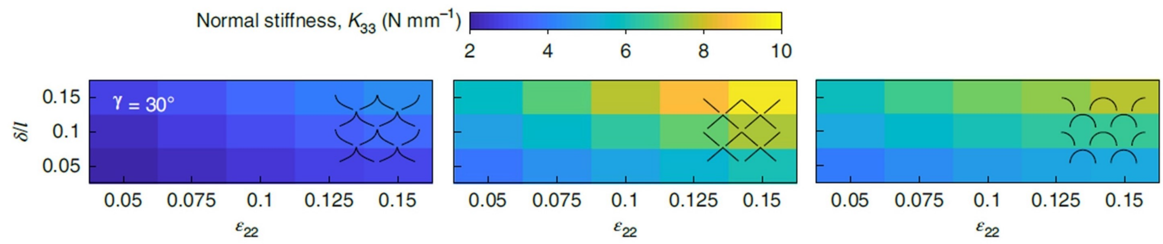

Figure 2.21: Effect of δ/l on the stiffness in the 33 direction (K33) of the kirigami spikes [14]

Summarizing the angled cut pattern kirigami behaviour and its application areas

After reviewing the literature related to the angled cut pattern kirigami surfaces, we can briefly summarise their behaviour as follows:

1. These kirigami metasurfaces display a relatively lower amount of in-plane strain in the direction of the force as compared to linear cut kirigami surfaces.
2. They display a high out-of-plane deformation as a function of their cut angle.

If the goal of the required application is a controlled out-of-plane deflection, this type of kirigami cut pattern is beneficial. The use of stiff materials for this type of kirigami cut pattern limits the elastic strain levels that can be achieved. However, they allow for high out-of-plane stiffness. Research on these types of angled cut pattern kirigami metasurfaces using soft and tough materials has yet to be done thus far.

2.2.3. Research works using Kirigami for Aerodynamic Applications

In the work done by Gamble *et al.* [23], a method of aerodynamic control through surface texturing on aircraft wings using multifunctional kirigami composites was investigated. Linear cut pattern kirigami metasurfaces, manufactured using thin film thin-film gallium arsenide solar cells, were used to increase the drag over the wings and subsequently control the aircraft's yaw. Wind tunnel experiments were also done to quantify the lift, drag and yaw moment. The study showed that these kirigami skins on the wings demonstrated excellent yaw-control capabilities and allowed for a delayed aerodynamic stall. This delayed stall behaviour indicated that the actuated kirigami features might delay the flow separation. The kirigami geometry used can be seen in Figure 2.22 and the illustration of the kirigami surfaces over the airfoil at different strains can be seen in Figure 2.23.

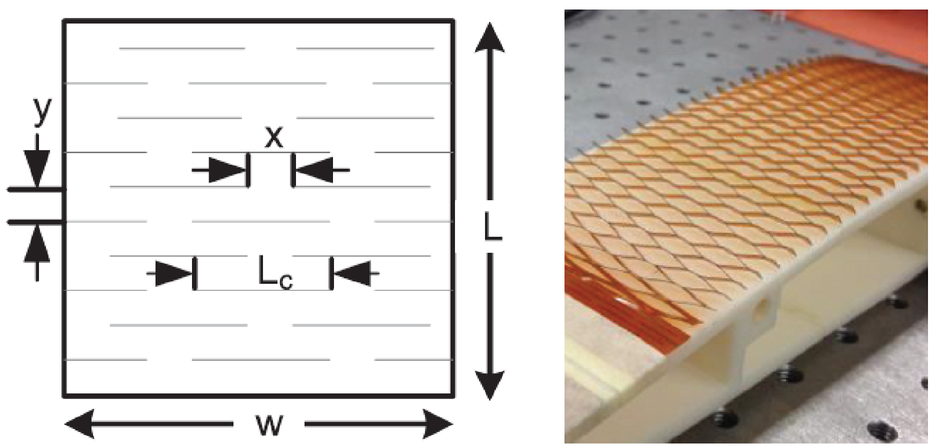

Figure 2.22: Illustration of the linear cut pattern kirigami and a close up of the kirigami solar film covering the airfoil [23]

Surface texturing has been shown to reduce skin friction and provide a slip condition at the surface. In addition, wing surface texturing using kirigami scale-like substrates allows for active drag steering and possibly a delayed flow separation.

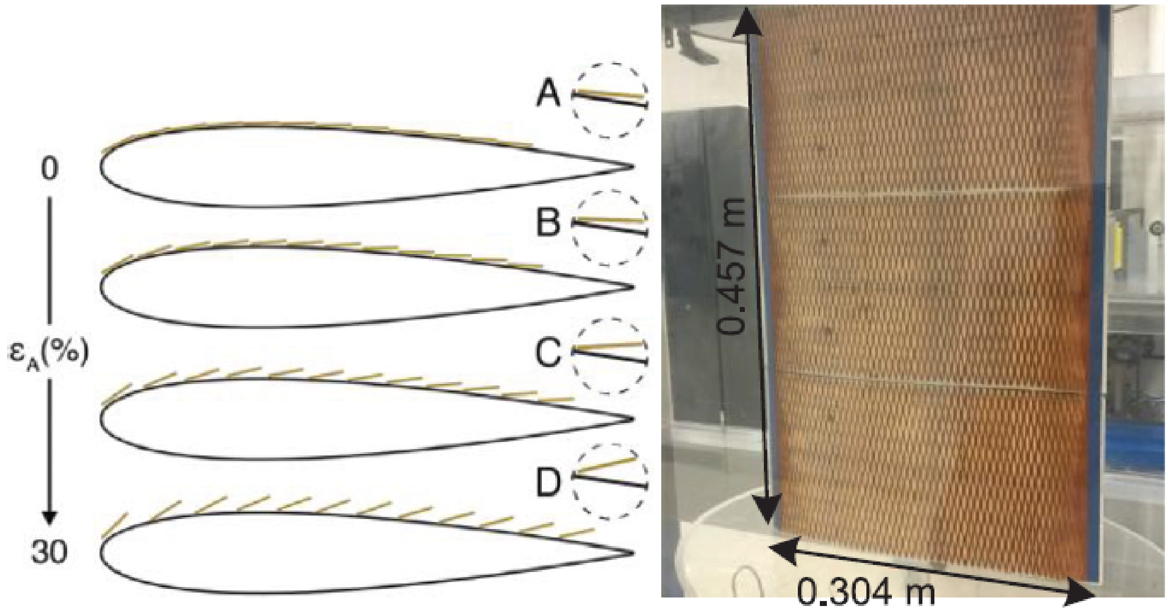

Figure 2.23: Illustration of the kirigami surface actuated at various strains over the airfoil [23]

During the wind tunnel testing, it was observed that as the kirigami surface was actuated, the lift curve shifted downward, and the stall angle (angle of maximum lift) increased by two degrees, with the lift curve experiencing a minor reduction. The plot is shown in Figure 2.24, where the numbers inset in the plot, show the strain applied on the kirigami surface, i.e. the kirigami surface actuation.

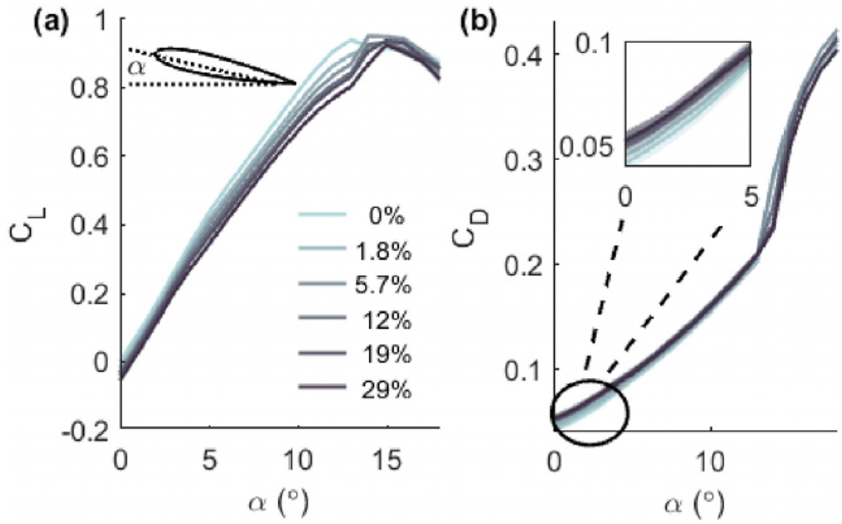

Figure 2.24: Aerodynamic response of kirigami actuation [23]
(a) Coefficient of Lift vs angle of attack | (b) Coefficient of Drag vs angle of attack
The legend shows the level of applied strain on the kirigami metasurface

This work demonstrated that kirigami could effectively be used for drag steering and delaying flow separation. Also, prior to the stall angle, increasing the strain on the kirigami sheet increased the drag.

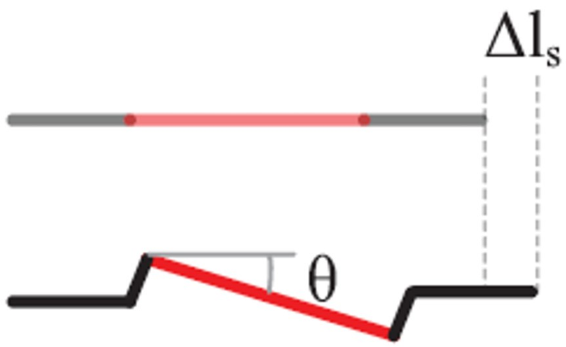

Figure 2.25: Side view of the deformed kirigami geometry in response to axial strain [23]

This out-of-plane deflection angle θ, is derived geometrically as:

$$\theta = \cos^{-1}\left(\frac{1}{\epsilon_A + 1}\right) \tag{2.15}$$

where ϵ_A is the applied axial strain [39]. The maximal strain applicable in this work is 0.29. Therefore, the max calculated out-of-plane deflection θ, angle is **39.18 degrees**.

Linear cut pattern buckling-induced kirigami metasurfaces used on top of the wings can achieve drag responses, as shown in Figure 2.24. The question that comes to mind is *what kind of drag can angled cut pattern kirigami metasurfaces*, with their greater out-of-plane deformations, produce?

3

Research Definition

This section will cover the research gaps found after reviewing the available literature, the objectives of this research, the main research questions to be answered and a map of how the work was carried out.

3.1. Research Gap

After reviewing the literature, a gap has been identified in the scope for additive manufacturing of angled cut pattern, buckling-induced kirigami metasurfaces. Some key observations made are as follows:

1. The use of Additive Manufacturing (AM) as a design feature in the creation of kirigami metasurfaces has yet to be done. The scope for tuning the response within an angled cut kirigami unit cell by exploiting the anisotropy of parts created using the additive manufacturing processes was yet to be explored.
2. A majority of the research conducted on angled cut pattern kirigami metasurfaces focused on using stiff polymers and metals such as steel. The starting point always involved using isotropic sheets made from such stiff materials. Cuts were subsequently imparted to these sheets using subtractive processes such as laser cutting.
3. Existing research works did not characterize the full field displacements and strains of the kirigami metasurfaces.
4. The amount of drag that could be generated by angled cut pattern, buckling induced kirigami metasurfaces has yet to be explored.

3.2. Research Objective

The research aims to explore the possibilities of using elastomeric materials and AM for applications in angled cut pattern kirigami metasurfaces. Tough materials such as elastomers would allow for higher elastic strain levels and repetitive use without plastic deformation and damage in the kirigami metasurfaces. AM allows for tuning the bistabilities of the kirigami unit cells by controlling factors such as local thickness, stacking sequence and infill pattern. Compared to subtractive cutting, the use of AM also leads to lower residual stresses at the cut locations due to an absence of intense localized heating (laser cutting). These angled-cut pattern kirigami metasurfaces, made using elastomer, also have much potential for surface texturing and applications involving local drag generation. They are quite similar to the scales found in shark skins [40], which are known to offer hydrodynamic advantages. These scales help prevent flow separation. For these aerodynamic applications, the area projected by a kirigami unit cell can give us a good idea of the proportional drag they can generate.

To achieve these objectives, it is essential to carry out design trials and observe the best design and print specifics that can be achieved for such kirigami metasurfaces within the scope of Fused

Filament Fabrication (FFF). Designs that would create metasurfaces capable of eliciting a complete out-of-plane buckling response. After achieving this objective, the next focus would be to characterize this mechanical response and observe the full-filed displacements and strains of the kirigami metasurface. Furthermore, it is also essential to make observations regarding the effect on the mechanical behaviour of the kirigami metasurfaces due to FFF and how this affects or influences their bistability.

3.3. Research Questions

The main research questions that need to be answered in order to fulfil the research objective are:

1. What design features are achievable for angled cut pattern, elastomeric kirigami metasurface using FFF?
2. What is the mechanical response of the manufactured kirigami metasurfaces, and how does FFF affect them?
3. What comparisons can be made between the area projected by linear and angled cut pattern kirigami metasurfaces?

For the goal of studying the out-of-plane behaviour, the second research questions can be broken down as follows:

1. What is out-of-plane displacement response of the metasurface on applying loads?
2. What is the out-of-plane angular deflection response of the Kirigami unit cells?
3. What is the force required to reach such a defection angle?
4. And how do the above stated variables differ from each other with respect to varying the unit cell design?
5. What observations can be made about the bistability of the kirigami metasurfaces due to the use of FFF?

3.4. Road Map

The approach towards this research can be summarized as the following sequence of events:

Design:

1. Selecting a particular elastomeric material for the kirigami metasurface to be studied.
2. Deciding on the geometry and the characteristic geometric parameters of a unit cell used, in the periodic lattice array of cuts to form the kirigami metasurface.

Manufacturing and sample preparation:

1. Running trials on the FFF printer to determine the specific geometric features that can be achieved considering the material used.
2. Fine-tuning the printing parameters to achieve consistent and repeatable prints, free from defects.
3. Finalizing the sample size to be studied.

Testing:

1. Setting up an experimental protocol.
2. Performing the testing and collecting the response data.
3. Post-processing and reporting the results.
4. Drawing conclusions and inferences for future research.

4

Sample Sizing & Manufacturing

The cut unit cell shape for the kirigami samples was chosen as triangular. This cut shape was chosen as it gives the greatest out-of-plane stiffness (K33) compared to other spike-based designs meant to deform out-of-plane [14]. In addition, this unit cell design mimics shark scales, which are known to provide hydrodynamic advantages, as mentioned in subsection 2.2.3. Therefore, with the goal of future use in aerodynamics applications involving surface texturing and drag force generation, this cut design is the most suitable for this study. Additionally, this kirigami cut pattern has been extensively studied through numerical simulations and experimental testing of physical samples [14].

4.1. Sample Sizing and Characteristic variations

Ideally, studying the mechanical response of an infinite sheet size kirigami sample would be preferred, as it would be independent of edge effects. However, specific practical considerations need to be made to design a sample that can be manufactured using FFF printing and provides a sufficient response for a successful study and testing.

4.1.1. Characteristic Design Parameters

This study will characterise the out-of-plane mechanical response of an angled cut pattern, buckling-induced kirigami metasurfaces. This response will be observed while varying the characteristic geometric design parameters of a cut as shown in Figure 4.1.

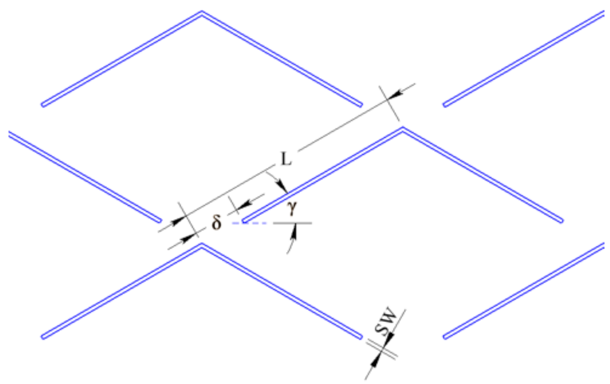

Figure 4.1: Characteristic design parameters of the cuts

The characteristic design parameters used to define a particular cut lattice pattern for triangular shape are shown in Figure 4.1. In this figure, the cut angle is represented as **γ**, the characteristic length of the periodic lattice is represented as **L**. The length of the segment separating the cuts, also referred to as the hinge length, is represented by **δ** and finally **SW** or slit width, represents the width of the cut.

4.1.2. Design Parameters varied for Testing

The main characteristic design parameters of interest were the cut angle (γ) and the dimensionless ratio of δ/L, which is defined as the ratio between the hinge length (δ) and characteristic length (L) of the periodic lattice. These two parameters were selected as they are what primarily control the mechanical response of the kirigami metasurface.The decision was made to use samples with cut angles varying from 20 to 60 degrees in 10-degree increments to observe the effects of varying the cut angle on the mechanical response. The dimensionless ratio δ/L would be fixed at 0.10 for these tests. To observe how the mechanical response varies with cut dimensionless ratio δ/L, a representative cut angle of 30 degrees was fixed, and the dimensionless ratio δ/L was varied from 0.10 to 0.20 at increments of 0.05.

4.1.3. Sample Sizing

Multiple factors go into the sizing of a sample. One significant design parameter affecting the sample sizing is the cut angle. For the same characteristic length, different cut angles will give different sample sizes for the same number of unit cells. To maintain a standard for averaged and normalized testing, a 3x6 pattern was fixed for all sample types. A fixed grid of unit cells (3x6) was chosen over a fixed sample size for all angle types. This was done as a fixed sample size would require unusual cut angle intervals to sufficiently fill the sample dimensions. Additionally, the number of print lines used to construct a sample remains constant with a fixed grid for all angle types. This is important as manufacturing specifics affect the overall mechanical behaviour. A fixed grid allows for a better comparative analysis between different angle types compared to a fixed sample size. Another factor to consider is the minimum hinge length. The minimum hinge length selected must not allow for tensile failure before buckling can occur. The final consideration is the characteristic design parameters to be varied. The following choices were made for the sample sizing, keeping all of the above factors in mind:

1. The lattice pattern of the cuts would follow a 3 x 6 [Length x Height] pattern for all cut angles.
2. The characteristic length (L) would be fixed at 15 mm.
3. Additional tabs of 15 mm would be added to the top and bottom of each sample to help with testing, as can be seen in Figure 4.2.

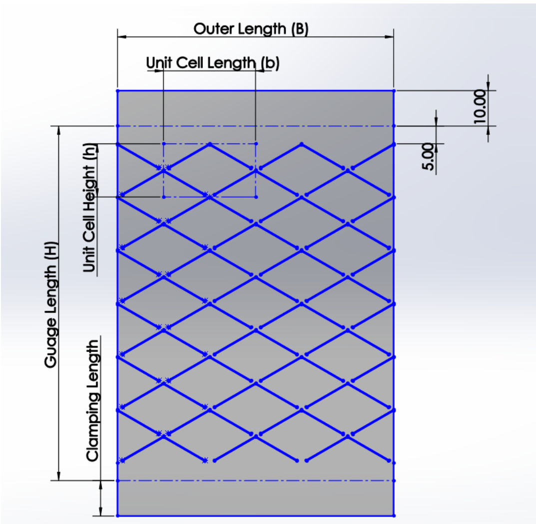

Figure 4.2: Sample geometric dimension specifics

Through trial and error, samples with various hinge lengths, starting from 0.9 to 2 mm, were manufactured. It was found that the minimum hinge length (δ) required for suitable samples was 1.5 mm. Hence, the characteristic length (L) was set at 15 mm as this would allow for samples with a δ/L ratio of 0.1, as seen in Table 4.1.

	δ/L		
	0.1	0.15	0.2
L (mm)	**δ (mm)**		
9	0.9	1.35	1.8
10	1	1.5	2
11	1.1	1.65	2.2
12	1.2	1.8	2.4
13	1.3	1.95	2.6
14	1.4	2.1	2.8
15	**1.5**	**2.25**	**3**
16	1.6	2.4	3.2
17	1.7	2.55	3.4
18	1.8	2.7	3.6
19	1.9	2.85	3.8
20	2	3	4

Table 4.1: Characteristic length (L) and hinge length (δ) combination require for different δ/L values

With a fixed characteristic length (L) value and the 3×6 lattice pattern chosen, the length and height dimensions of a single unit cell and the sample they would generate are shown in Table 4.2. The variables representing the dimensions shown in the table below are defined in Figure 4.2.

	Single Unit Cell		Final Sample	
γ (°)	Length, b (mm)	Height, h (mm)	Length, B (mm)	Height, H (Gauge) (mm)
20	28.19	10.26	84.57	71.56
30	25.98	15.00	77.94	100.00
40	22.98	19.28	68.94	125.70
50	19.28	22.98	57.85	147.89
60	15.00	25.98	45.00	165.89

Table 4.2: Outer dimensions of the Kirigami samples for a fixed characteristic length of 15 mm

Since the 3x6 pattern and the characteristic length (L) were fixed, we can observe that the manufactured samples had different widths and heights. This was due to the varying cut angle (γ) values. The sample types can be seen in Figure 4.3. After testing, the strain values for each sample type would be used as a metric for comparison. The thickness of all the samples was fixed at 0.3 mm.

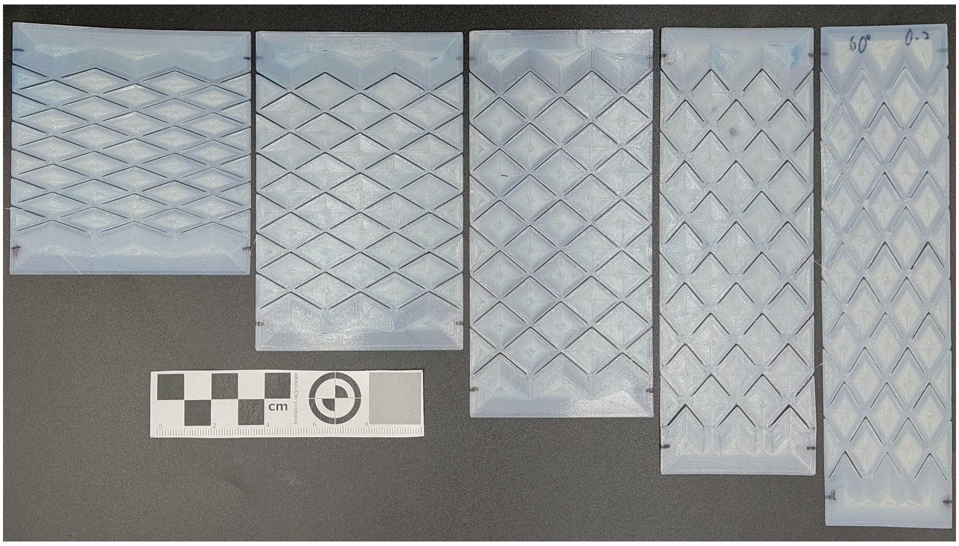

Figure 4.3: Kirigami Samples printed with cut angles from 20 to 60 Degrees (Left to Right), with 10 degree increments

4.2. Manufacturing

Flat isotropic sheets have been used to manufacture kirigami metasurfaces. Thin sheets of steel or polymeric materials are embedded with a periodic array of cuts using methods such as laser cutting. However, in this project, the kirigami metasurfaces are manufactured using additive manufacturing (AM). AM is used as a design feature to create whole parts without any subtractive cuts. The AM method chosen in particular is Fused Filament Fabrication (FFF). Fused Filament Fabrication is an extrusion process where parts are built by depositing melted material in a layerwise fashion.

4.2.1. FFF Printer Used

The printer used is a stock Prusa MK3S with a textured steel sheet [24]. Elastomers are prone to stick to the print bed after printing and are difficult to remove. Therefore, a textured steel print bed was used as it helps with the removal of the TPE samples from the print bed, after printing.

Figure 4.4: A Prusa MK3S FFF Printer [24]

4.2.2. Material used

The material used to manufacture the samples is thermoplastic elastomer (TPE). TPE filaments used in AM consist of a physical mixture of polymers such as a plastic and a rubber. They combine the rubber-like properties with thermoplastic processability. They give properties that close the gap between the elastomeric and thermoplastic materials [41]. TPEs can be grouped into two types: 1.) Block copolymers and 2.) Polymer blends.

1. Block copolymers contain hard (thermoplastic) and soft (elastomeric) segments that chemically form a macromolecule. Representatives of the thermoplastic part are thermoplastic styrene elastomers (TPS), thermoplastic co-polyesters (TCP) and thermoplastic polyamide elastomers (TPA) [42]. The elastomeric segments can be formed from unsaturated (poly(styrene-b-isoprene-b-styrene) (SIS); poly(styrene-b-butadiene-b-styrene) (SBS)) or saturated (poly(styrene-b-(ethy lene-co-propylene)-b-styrene (SEPS), poly(styrene-b-(ethylene-co-buty lene)- b-styrene) (SEBS)) blocks [43].

2. In polymer blends, the thermoplastic and the elastomer are physically mixed in a two-phase system. In polymer blends the elastomeric phase can either be present in so-called TPE-based olefins without cross-linking (TPO) or dynamically cross-linked thermoplastics (thermoplastic vulcanize (TPV)) [42].

The composition of commercially available FFF TPE filaments is confidential as they are industry secrets. Their shore hardness levels are used to categorize them.

TPE was selected as the print material for the high degree of elasticity and toughness it offered. This allowed for the manufacturing of samples with a lower hinge area and thickness. Compared to other stiffer FFF filaments, such as PLA, that would fail at much lower loads for the exact hinge dimensions before the buckling load of the kirigami sheets could be reached.

The TPE filament used was the 1.75 mm 123-3D Jupiter series TPE filament [44]. This filament was chosen as it is locally available and a 1.75 mm diameter was chosen to match the requirements of the Prusa MK3S printer used. The material specification is shown in Table 4.3.

Filament Diameter	1.75 mm	**Print temperature**	220–260 °C
Max. Deviation	±0.05 mm	**Shore Hardness**	45D
Roundness	>95%	**Tensile Modulus**	95 MPa
Bed Temperature	0–95 °C	**Specific Gravity**	1.14 g/cc

Table 4.3: Material properties and printing specifications provided by the supplier

4.2.3. Print Settings and Printing Challenges

The chosen print settings for the samples are given in Table 4.4. Since kirigami metasurfaces must be thin to allow for the exploitation of the local inelastic instabilities, it would be beneficial for the sample thickness to be set as low as possible. However, if the samples were too thin, removing them from the print bed would be difficult without damaging them, and they would also warp out of shape due to residual heat. Therefore, samples printed with two print layers gave suitable results and maintained their shape after removal from the print bed. A layer height of 0.1 mm was used, with the first layer having a height of 0.2 mm. This is usually the case in FFF 3D printing and helps maintain the perimeters of the print after shrinkage and helps with bed adhesion. With these two layers, the CAD models for the samples given to the slicer had a thickness of 0.3 mm. Since TPE was used as the material, the print speed needed to be kept low, and filament retraction had to be turned off. This was done as retraction could lead to the jamming of the filament, as seen in Figure 4.9. The Nozzle and bed temperatures were set within the range specified by the manufacturer. The print settings in Table 4.4 allowed for the least amount of defects, such as porosities and gaps in the print, while maintaining consistent print quality and avoiding slit closure.

Nozzle Size	0.4 mm	XY Size Compensation	-0.03 mm
Layer Height	0.1 mm	Perimeter Print Speed	20 mm/s
First Layer Height	0.2 mm	Infill Speed	60 mm/s
Perimeters	4	Nozzle Temperature	240 °C
Infill Pattern	Concentric	Bed Temperature	50 °C

Table 4.4: Printing Parameters

XY Size Compensation is a setting used to thicken or thin $(+\backslash-)$ all the print walls in the XY plane. A print wall consists of internal and external perimeters. The XY compensation option helps compensate for the expansion or shrinkage of printed parts. The concentric infill pattern is an internal structure composed of concentric lines that match the outline of the part. The print features controlled by these options are illustrated in Figure 4.5.

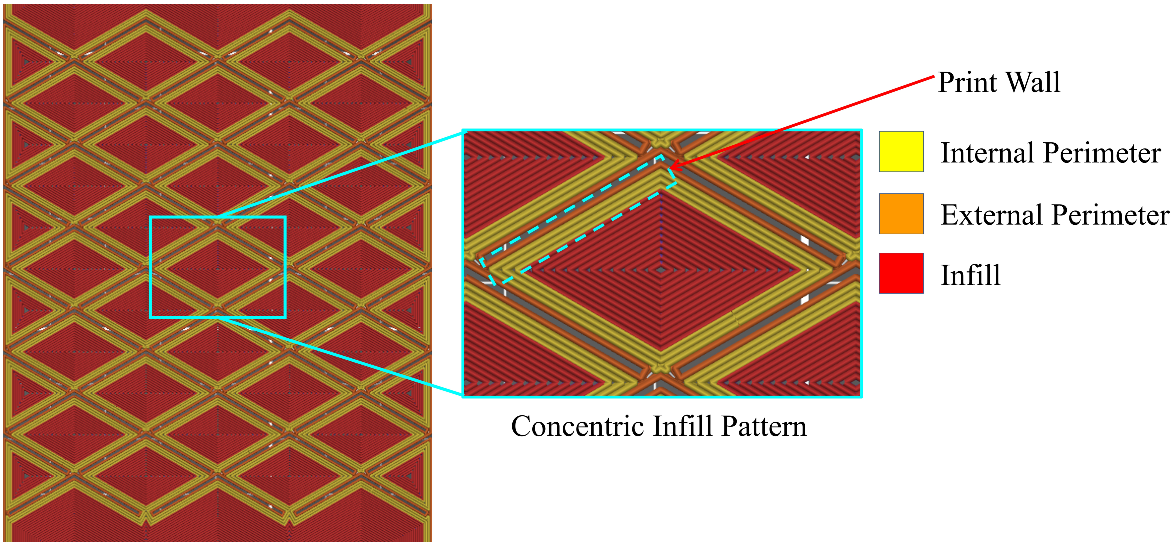

Figure 4.5: Print Feature Specifics

4.2.4. Slit Sizing and Printing Considerations

A significant issue while printing the Kirigami samples is the slit closure due to the fusion of material at the slits. This can be seen in the highlighted regions in Figure 4.6. To prevent this type of slit closure, several choices were made with the printing parameters to ensure better dimensional accuracy of the prints.

1. The option to print outer perimeters first was also enabled on the Prusa slicer. This allowed for better dimensional accuracy of the outer perimeters of the sample.
2. The number of perimeters was set to 4. This placed a greater barrier between the infill print lines and the slits. This barrier was important as it minimised the expansion of the infill printed lines. These infill lines being perpendicular to the slit often caused slit closure upon expansion.
3. The infill pattern was set to concentric. This allowed the printing along the slit length, which helped keep the slit shape and dimensions.
4. The XY Size compensation was set to -0.03 mm to compensate for material expansion near the slits.

Apart from the parameters set in Table 4.4, default settings were used on the Prusa slicer. After a series of test prints, the slit size for the sample specimens was set to 0.25 mm—this value allowed for consistent prints without fusion.

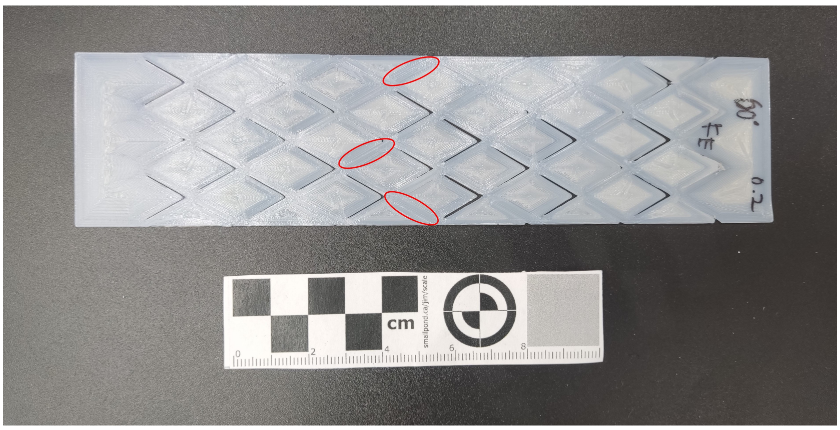

Figure 4.6: Slit fusion in a printed Kirigami Sample

4.3. Defects

During the printing process, the primary defect encountered during the printing of the samples was gaps in the print lines. This usually occurred at intersection points of multiple print lines, such as at the hinges of the kirigami samples. This occurred primarily due to residual heat at these locations, leading to shrinkage and a failure of material fusion. This defect can be seen in regions **a** and **b** in Figure 4.7. The defect at region **c** occurred when the infill stepped from concentric to linear near the tab regions. This change in print direction led to these gaps.

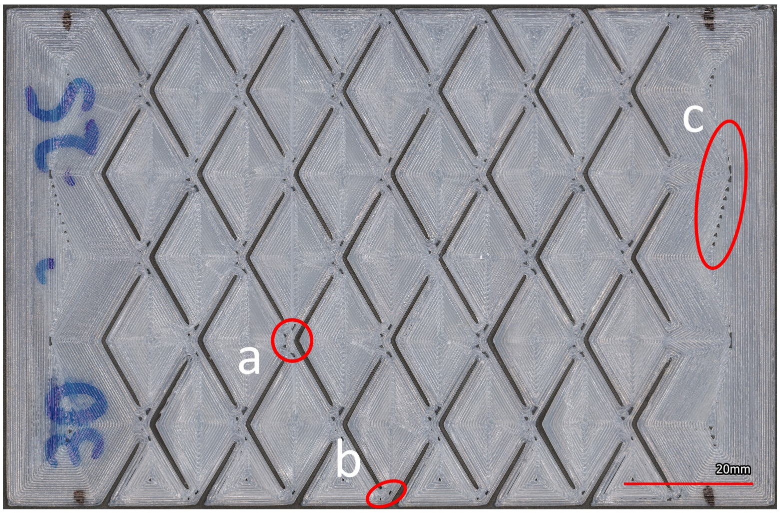

Figure 4.7: Sample with numerous defects (30 Degrees)

The height map of this defective sample, shown in Figure 4.8, also clearly displays the porosities in the sample. These defects at the hinges critically decrease the mechanical response of the sample, as they are located at the regions from where the buckling is initially initiated. As a result, they cause stress concentrations and lead to premature failures. Therefore, all samples with defects were discarded.

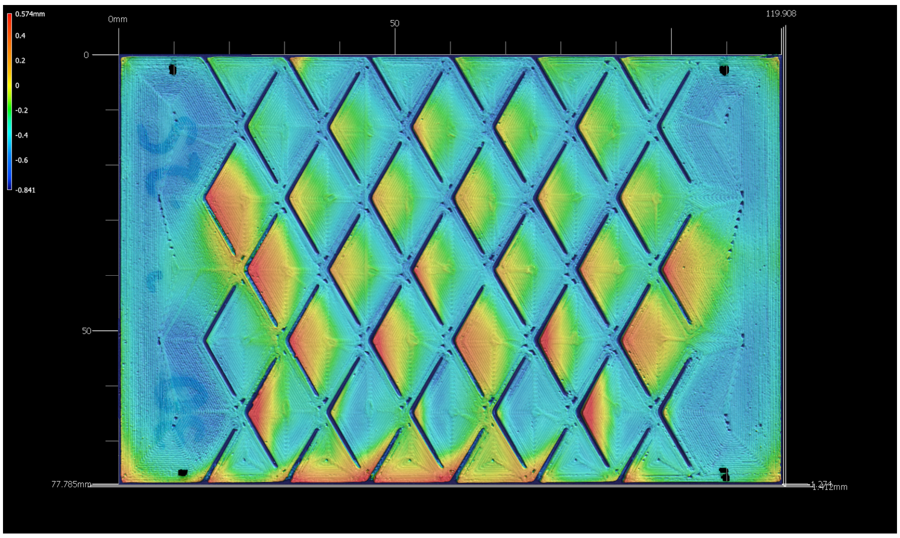

Figure 4.8: 30 degree defect sample Height Map

Another issue while continuously printing with TPE filament is heat creep. Over the course of continuous printing, heat generated at the nozzle hot end slowly creeps up to the toothed gear wheel at the cold end extrusion stepper motor. This motor and gear wheels are used to dispense filament. This conducted heat causes the filament to creep and jam. An example of this heat creep on the filament can be seen highlighted in Figure 4.9. Below the highlighted circled portion, we can also observe the wavy spaghetti-like form of the filament. This problem is particularly cumbersome as it occurs only after a good portion of the print has been completed and leads to failed prints as the filament can no longer extrude.

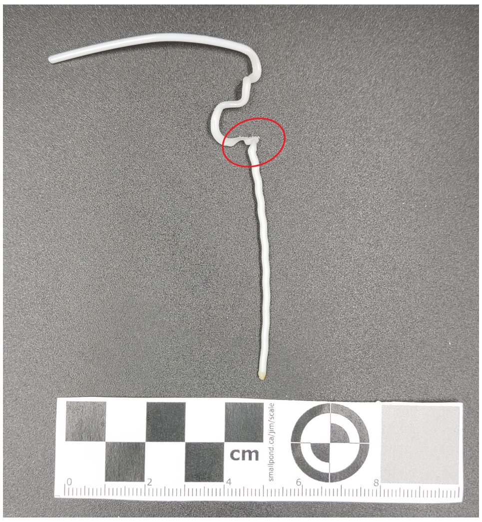

Figure 4.9: Filament Jamming

This can be avoided by setting shorter print times and by avoiding continuous printing for long periods of time.

4.4. Printed Samples

A Keyence VR-5000 Wide Area 3D measuring system was used to measure the actual dimensions of the printed samples. This was done to observe the differences between the given CAD and printed sample dimensions. The Keyence measuring system allows for measuring the height profile and gives accurate dimensions of features such as the slits, which have a dimension of less than 1 mm. The given CAD dimensions for the sample shown below were a slit size of 0.25 mm, a cut angle of 30 degrees and a thickness of 0.30 mm

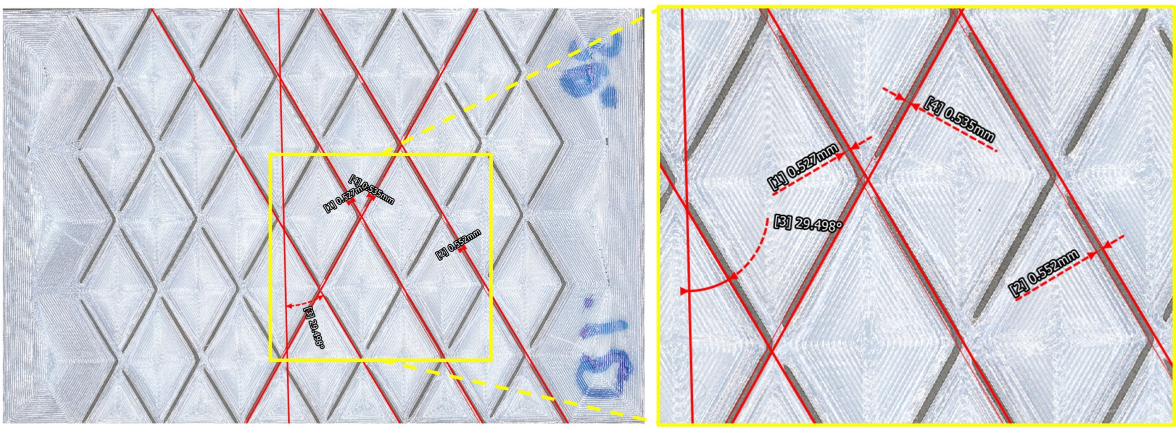

[1]	Slit Size	0.527 mm
[2]	Slit Size	0.552 mm
[3]	Angle	29.498°
[4]	Slit Size	0.535 mm

Figure 4.10: 30 degree printed sample with the characteristic features measured

From observing the printed samples, it was clear that the outer dimensions and the cut angle were quite similar to the values set in the CAD. The deviation from the CAD was only 0.5 degrees in the cut angle. As shown in Figure 4.10, the actual slit width value of the printed samples was higher than the given CAD value of 0.25 mm. On observation of different slits on the same sample and of other printed samples, it was found that the slit width varied from 0.5 to 0.55 mm for all printed samples.

There were also variations in the thickness of the printed sample. As can be seen in the height map in Figure 4.11, the variations exist within a sample as well. The samples seem to be thicker towards the centre of triangular spike regions. The two reasons for this variation are:

1. The concentric infill pattern.
2. Additional material trailing out of the print nozzle head as it finishes the material deposition at one triangular unit cell region and then moves on to the next.

The second reason occurs due to the retraction being disabled during printing and during the print head motion.

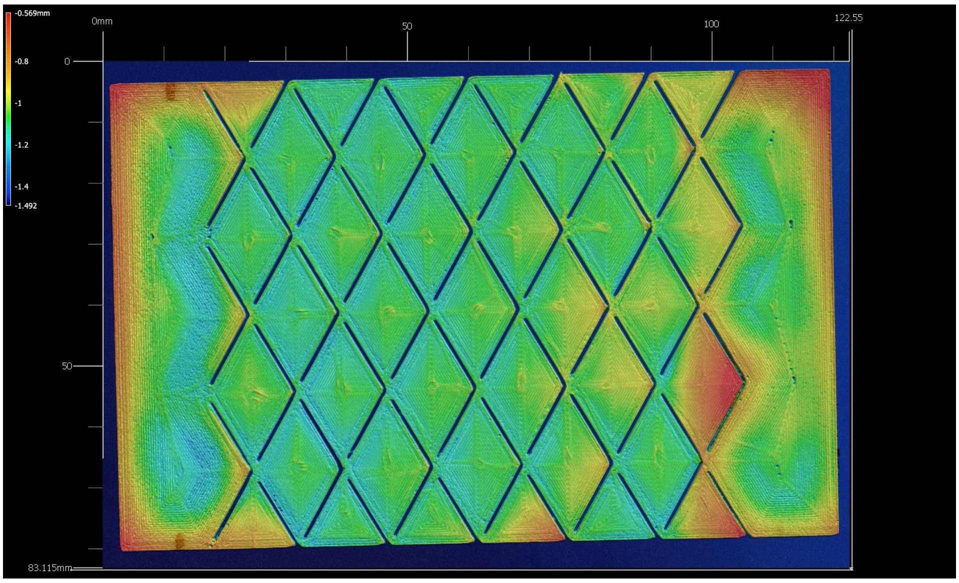

Figure 4.11: 30 Degree Sample Height Map

Using a micrometer screw gauge to confirm, the sample thicknesses for the printed samples varied from 0.35 mm to 0.45 mm at different regions on the sample. This differed from the given CAD thickness of 0.30 mm. This printed sample thickness range of 0.35-0.45 mm was maintained for all printed samples.

5

Methodology: Experimental Protocol and Mechanical Testing

To observe the out-of-plane mechanical response of the buckling induced kirigami metasurfaces, the samples need to be observed while in uniaxial in-plane tension. This extension initiates the out-of-plane buckling response. To quantify this response and observe the full field displacement and strain, Digital Image Correlation (DIC) was used. When the in-plane load was applied, the out-of-plane displacement response of the kirigami unit cells could then be measured by the DIC cameras. This chapter details the mechanical testing equipment used, the data-acquisition instruments used, and the experimental protocol followed.

5.1. Experimental Setup

Testing Equipment

The test was performed on a 20KN Zwick universal testing machine, using a mechanical clamp as shown in Figure 5.1. The samples were placed in these clamps with 10 mm of the sample height, gripped at the bottom and the top, as shown in Figure 4.2. When the test was started, the bottom crosshead would move in a downward direction. A 100 N load cell was used to measure the applied force. Two 5-megapixel cameras with 50 mm lenses were set up at a stereo angle of roughly 30 °or lesser, keeping to the recommendations of the Vic 3D user manual [25]. These cameras and their corresponding attachments were used to perform 3D DIC on the sample during the tensile test. The equipment and test setup can be seen in Figure 5.2. The top and bottom mechanical clamps were aligned collinearly to ensure that a uniaxial tensile force would be applied to the samples and not a shear force.

Figure 5.1: Mechanical Clamp used

Figure 5.2 shows the test setup for the experiment along with the 3D DIC cameras used to measure the out-of-plane displacements. Two floodlights were also positioned in front of the DIC cameras to illuminate the sample.

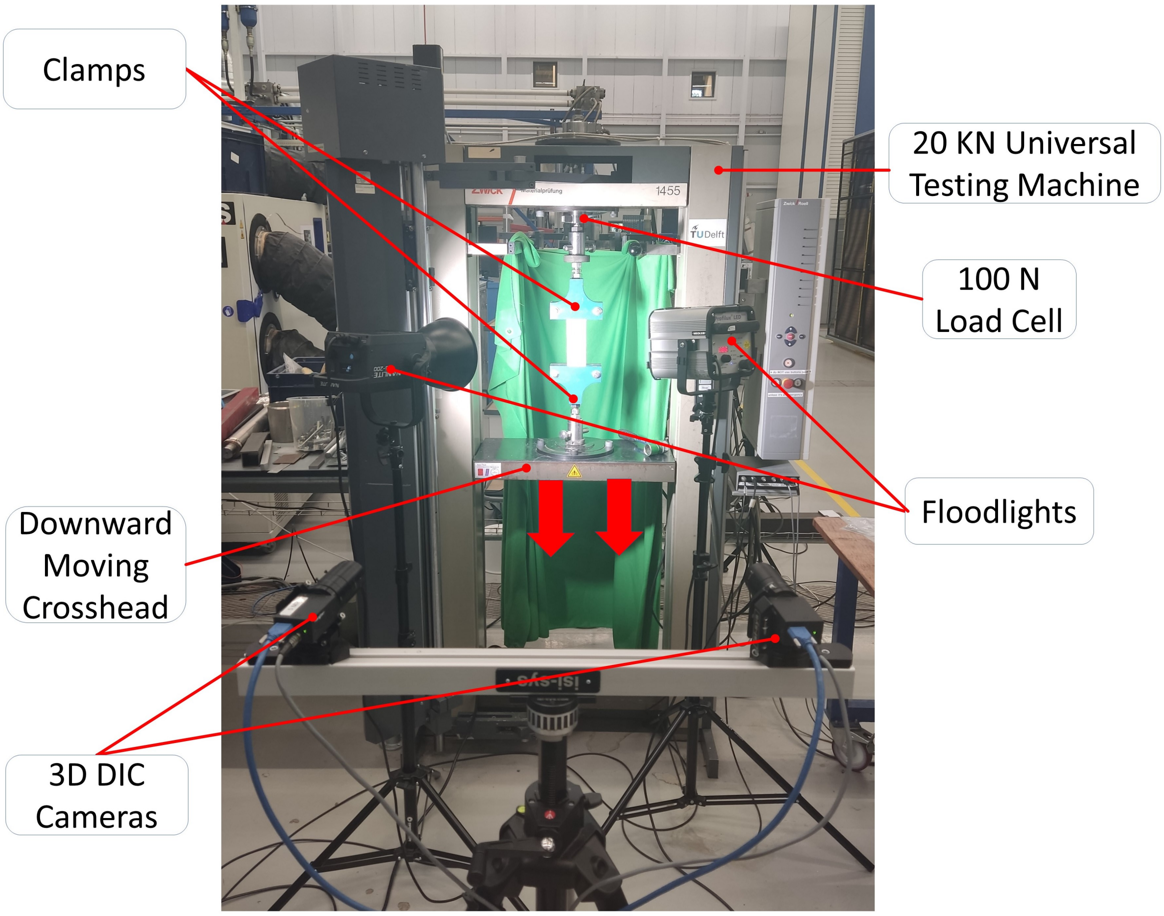

Figure 5.2: Testing Equipment Setup

5.2. Testing Instrumentation

The load and displacement data were sampled continuously during the test. The software on the universal testing machine sampled this test data at an interval of 0.1s. The testing machine was also connected to the 3D DIC system. The sampling rate of the cameras was one image per second. The analogue output was transferred from the universal testing machine to the DIC system. Photos were taken by the DIC camera using the Vic-Snap8 software [45]. Every time a photo was taken by the DIC cameras, the corresponding load and displacement data from the load cell was saved to that particular picture captured.

5.2.1. Digital Image Correlation

Since an out-of-plane behaviour is observed in the kirigami samples, the depth of field is of primary concern. Therefore, the lowest aperture is used to maximize the depth of field. The relationship between depth of field and camera aperture is shown in Figure 5.3. As the aperture of the DIC cameras was kept to a minimum, multiple floodlights were used to illuminate the samples. The cameras were placed at a distance of 162 cm from the samples. It was placed at this distance as the samples would be extended to 30 mm, and this distance allowed for a field of view that covered the extension behaviour of the longest sample.

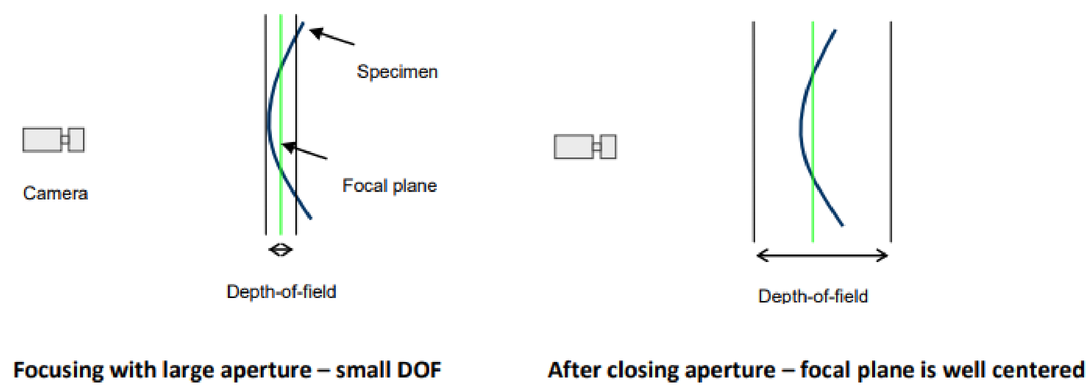

Figure 5.3: The effect of aperture on depth of field (Taken from the Vic3D Manual [25])

5.2.2. Speckle Pattern

Since the specimens being used would be subjected to large displacements, the field of view had to be set so that the specimens stayed in the view of the camera during the entire test. For this reason, the speckle dot size used was 0.66 mm. This pattern was achieved using the speckle rollers of the correlated solution VIC Speckle Pattern Application Kit [25]. This speckle dot size is much larger than what can be achieved by using a fine spray nozzle and is one size above what would typically be used on a sample of this size for lower strain applications, i.e. 0.33mm. The large strain and corresponding large field of view made it imperative to use a larger speckle dot size.

Ideally, a speckle size of 4-5 pixels would be used. However, owing to the large strain of the sample, the resolution of DIC cameras available and the 50 mm lens used, the decision was made to allow for a loss in fine spatial resolution. This meant that finer strain gradients would not be measured. However, the overall strain response would be measured successfully. The speckle size used allowed for a relatively accurate tracking of the strain behaviour near key geometric features such as the hinge region and the tip of the kirigami spikes. This tracking, however, came at the detriment of some aliasing. The speckle size relative to the subset size can be seen in Figure 5.4.

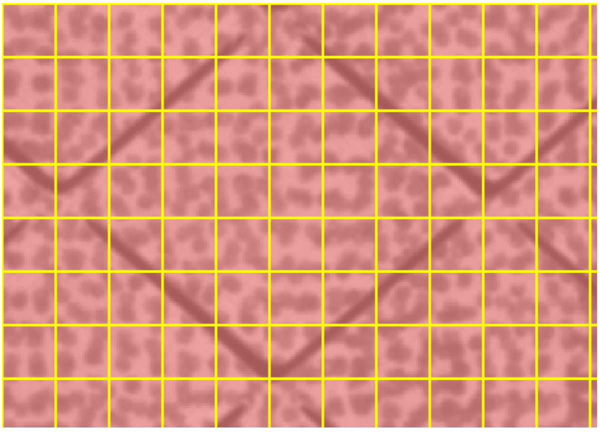

Figure 5.4: Subset Size with relation to the speckle size

As seen in Figure 5.4, the size of the speckle is less than that of the subset or the pixel. However, the DIC software was able to tract the speckles throughout the experiment. A 20 mm calibration plate was used, shown in Figure 5.5, to calibrate the cameras, as it matched the average height and width of the samples.

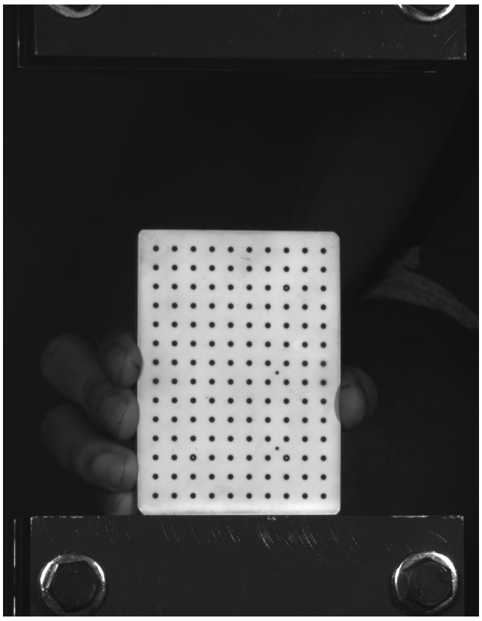

Figure 5.5: 20 mm calibration plate placed between the mounting clamps

The samples painted with the speckle pattern are shown in Figure 5.6. Two coats of white primer paint, followed by multiple passes of the 0.66 mm dot size roller [25] were used to generate the speckle pattern.

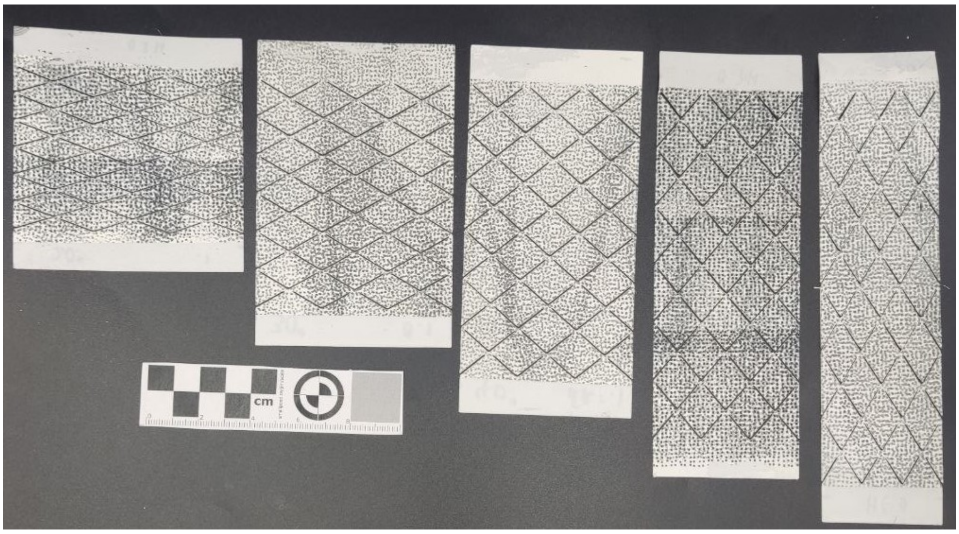

Figure 5.6: DIC Speckle Pattern on the printed samples

To aid the DIC system, the test was done in a stepped manner, instead of using a continuous displacement setting. The rationale behind this was that the sample does not offer too much resistance to the loads, and the final displacement value was set at 30 mm. If the testing was continuous, there would be a blur in images taken by the DIC system, due to a high strain rate during the test. Therefore, two testing options were present. Option 1: The tests could be performed at extremely low displacement rate. This, however, would take up an extremely large amount of time to complete. Option 2: the test would be performed in a stepped manner, where a displacement rate of 1 mm/s is set. But, after every 1 mm of displacement, the sample is held in place for 1 second, without any displacement and then the test would continue. The displacement controlled test sequence can be seen in Figure 5.7.

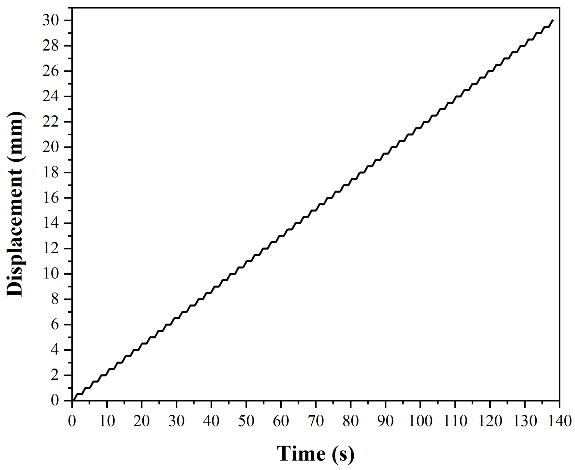

Figure 5.7: Testing Sequence

5.3. Test Procedure

The steps for the test procedure are presented in Figure 5.8. Initially the universal testing machine, the DIC system and the floodlights were set up. The analogue output from the load cell attached to the universal testing machine was connected to the DIC system. Next, the DIC system was calibrated using the calibration plate, shown in Figure 5.5. The calibration plate was placed on top of the bottom clamp. The speckled sample was then clamped to the universal testing machine. The clamps were then adjusted to the initial testing position, ensuring that the sample was held taut. The force and displacement readings were then set to zero, as the starting point of the test.

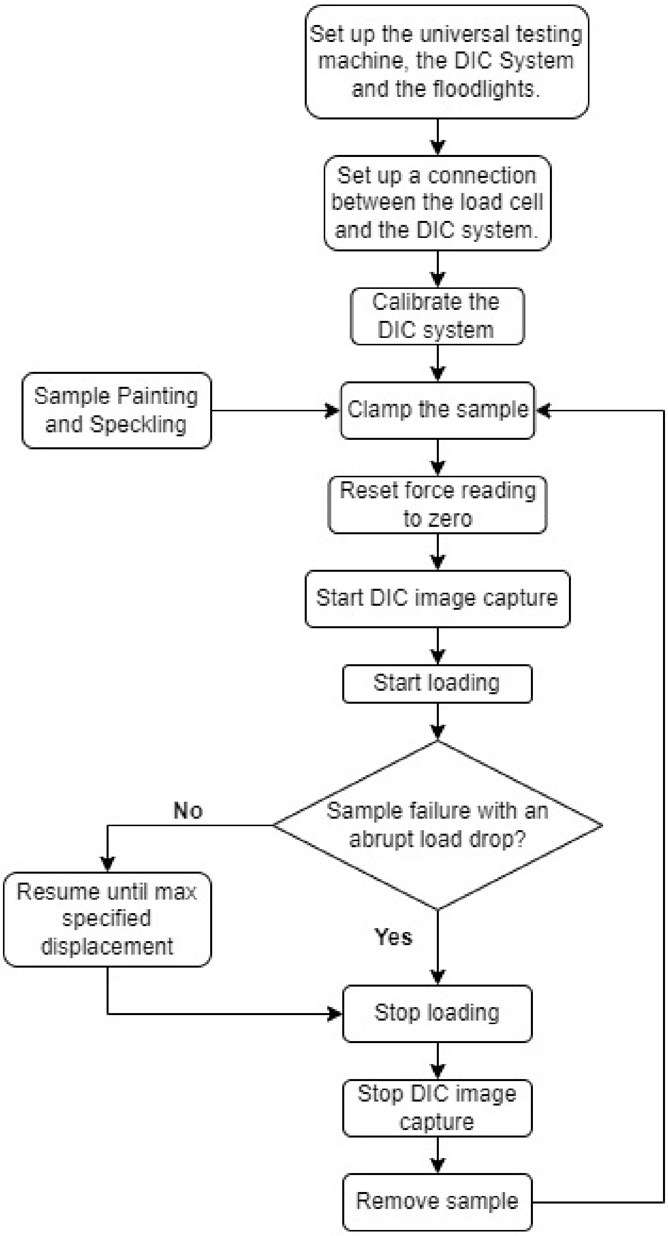

Figure 5.8: Test Procedure Flow Chart

The image capturing process for the DIC system was then commenced. Shortly after, the stepped loading sequence was commenced. The end point for the test was set at a total displacement of 30 mm or, if there was an abrupt load drop, due to sample failure. After the loading had been stopped, the DIC image capture was also stopped and the crosshead was moved back up to its initial position. The sample was then removed from the clamps. The next sample was then mounted to the testing machine and the procedure was repeated.

6

Results and Discussions

In this chapter, the results of the experiments will be presented, and their implications will be discussed. The specifics of the DIC data post-processing are discussed, and the post-processing schemes used to normalize the results are discussed.

6.1. Samples Tested

The aim of this study was to characterize the mechanical response of the buckling-induced kirigami metasurfaces and quantify how this response would vary based on the cut angle and the dimensionless ratio δ/L. The sample types and the number of samples tested are shown in Table 6.1. The characteristic design parameters varied are shown in Figure 4.1.

Cut Angle [γ (°)]	δ/L	Number of Samples
20	0.10	4
30	0.10	4
30	0.15	4
30	0.20	4
40	0.10	4
50	0.10	4
60	0.10	4

Table 6.1: Samples Tested

6.2. Data Post-Processing Scheme

6.2.1. DIC Data Post-processing

The Vic3D-8 software was used to post-process the DIC data obtained from the experiments. The captured speckle images of the samples and their corresponding calibration data were imported into the software. A subset size of 25 and a step size of 7 were set. Due to the high strain of the samples, the incremental correlation setting was used. This setting allows for the correlation between two subsequent images rather than always correlating using the reference image[25].

DIC was used for this experiment to quantify the out-of-plane deflection of the Kirigami metasurfaces. An example of out-of-plane displacement (W), for a 30°cut angle sample, at the end of the tensile test can be seen in Figure 6.1b. This figure also shows us the local coordinate system at the top right.

To numerically quantify this out-of-plane behaviour, data at particular regions on these contours must be sampled. The research question for this project specified that the out-of-plane strain response (E33), the out-of-plane angular deflection (θ) and the applied force required to reach this out-of-plane angular deflection (θ) were of prime concern. This means that the quantities of importance to be extracted from the DIC contours are the displacement in the y-direction (V) and the out-of-plane or z-displacement (W). Using these values, the out-of-plane strain (E33) and the out-of-plane angular deflection (θ) can be calculated.

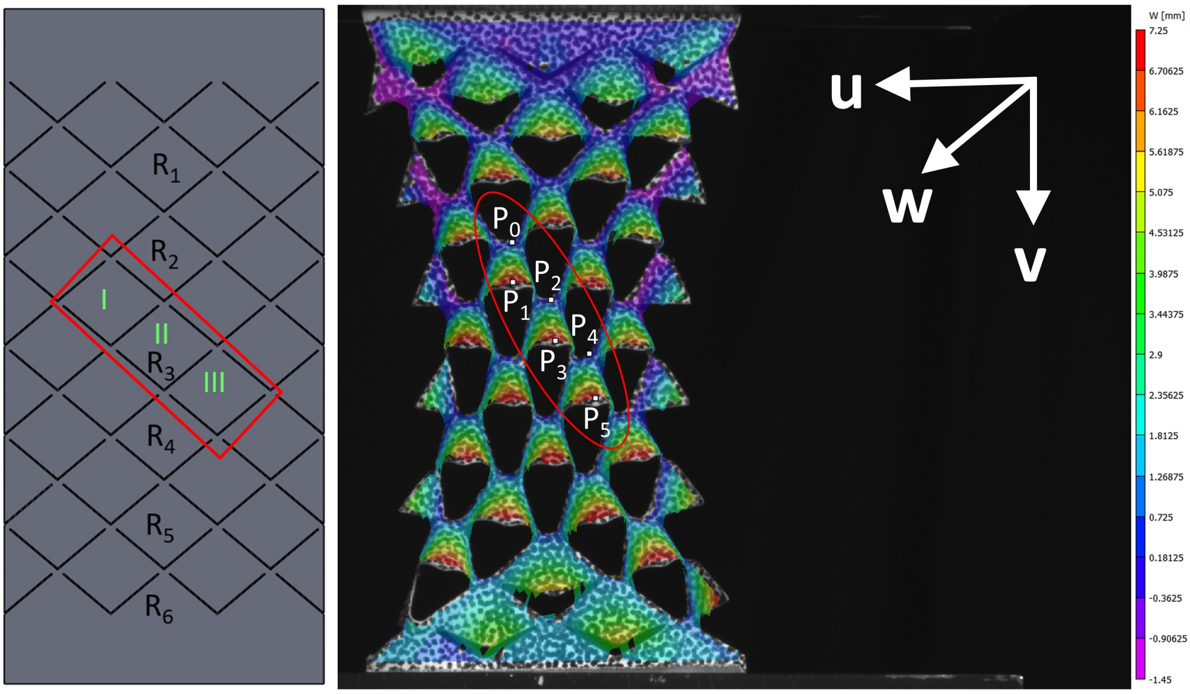

(a) Location of the chosen spikes

(b) Chosen spikes on the Post-Processed DIC Contours

Figure 6.1: DIC Post-Processing Specifics

Ideally, if the kirigami metasurface were an infinite sheet, each spike would display the same out-of-plane behaviour. However, for experimental testing, a finite sample was used. This meant that every spike might have shown a different displacement behaviour due to manufacturing effects or differences in paint thickness across different samples. Therefore, three central spikes were selected for data sampling to account for this variance. These spikes are demarcated as I, II and III in Figure 6.1a. The same spikes would be chosen across all the sample types.These three spikes were chosen as they are minimally affected by direct edge effects, such as lateral compression, and averaging out their out-of-plane response would give a good measure of the actual out-of-plane deflection behaviour.

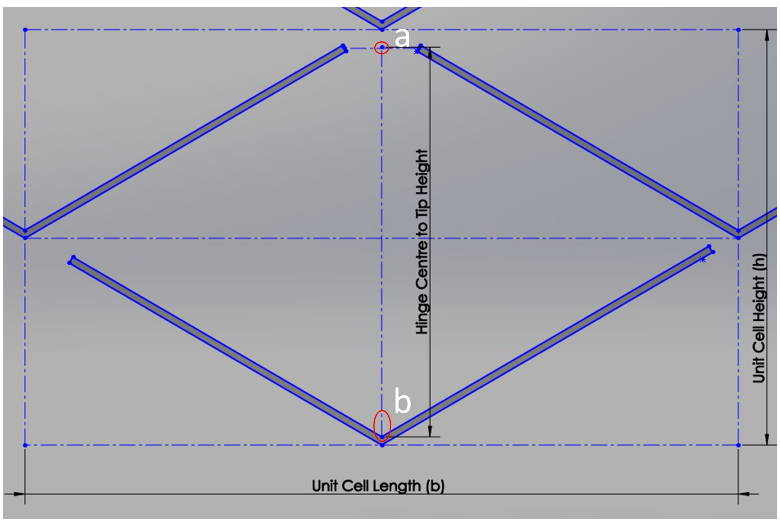

Figure 6.2: Unit Cell Close up

The six points, labelled from 0 to 5 in Figure 6.1b are the points from which the longitudinal in-plane displacement, V and the out-of-plane displacement, W values will be extracted.

Points $\mathbf{P_0}$,$\mathbf{P_2}$ and $\mathbf{P_4}$ from Figure 6.1b are located at the centre of the hinge length at **point a** in Figure 6.2. Points $\mathbf{P_1}$, $\mathbf{P_3}$ and $\mathbf{P_5}$ from Figure 6.1b are located as close to the tip of the spike as possible at **point b** in Figure 6.1b. The words "as close to the tip as possible" are used because the speckle pattern is random, and the speckle dots placed on the painted samples might not always align at the spike tips. Measuring the results in this manner helps to calculate the out-of-plane angular deflection. The way this is done is explained as follows.

The longitudinal in-plane, V and out-of-plane, W displacement values are collected from points a and b throughout the test. In Figure 6.3 I, a_v and a_w represent the V and W displacement values at point a. b_v and b_w represent the V and W displacement values at point b. They give a scalar representation of the displacement values and show their direction. a_v and b_v would move downwards in the v-direction and a_w and b_w would move in the out-of-plane w-direction during the test. These points, labelled 0 to 5, as seen in Figure 6.1b, for the three spikes, as seen in Figure 6.1a, represent the hinge and spike tip locations. These points are shown for each sample tested in Appendix A. They show the locations of these points at the start and the end of the tensile test.

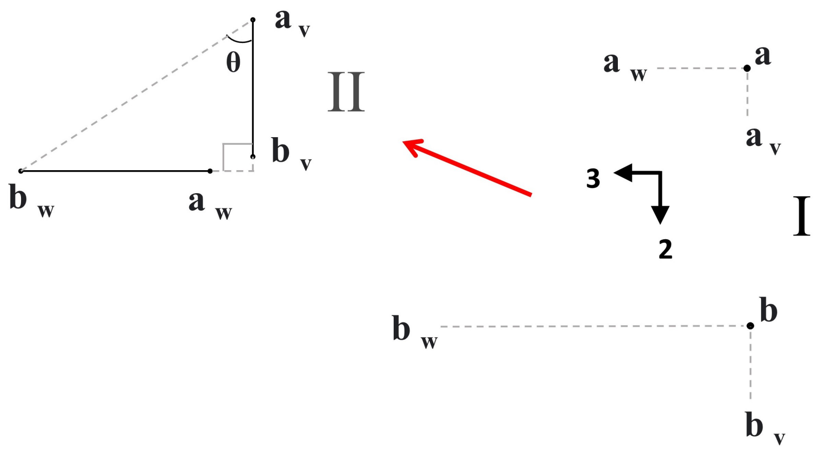

Figure 6.3: spike unit cell data post-processing

If we then subtract a_w from b_w and a_v from b_v, we would get the arms of a right-angled triangle, as shown in Figure 6.3. We can then find the out-of-plane deflection angle (θ):

$$\theta = \tan^{-1}\left(\frac{b_w - a_w}{b_v - a_v}\right) \tag{6.1}$$

The out-of-plane displacement (W_{chev}) for the tips of the spike can be given by subtracting a_w from b_w. To normalize this out-of-plane displacement (N_w) value, so as to achieve a fair and relative comparison between all the sample types, we do the following:

$$N_w = \left(\frac{b_w - a_w}{H}\right) \tag{6.2}$$

where H = Hinge Centre to Tip distance, visually shown in Figure 6.2. The H values for all sample types are given in Table 6.2.

Cut Angle [Y	δ/L	Hinge Centre to Tip (mm)
20	0.1	9.60
30	0.1	14.07
30	0.15	13.70
30	0.2	13.32
40	0.1	18.09
50	0.1	21.52
60	0.1	24.24

Table 6.2: Hinge Centre to Tip

The decision to sample data from the hinge centre and the spike tip and then subtract them was done as during the test, as the entire sample moves out-of-plane. If a relative measurement isn't made, the displacement results wouldn't be accurate at the tips.

6.2.2. DIC Result processing and Normalisation

The data received after post-processing the DIC images and extracting the required displacements from the desired locations is shown in Figure 6.4.

P2		P3		P1		P4		P5		P0	
V [mm]	W [mm]	V [mm]	W [mm]	V [mm]	W [mm]	V [mm]	W [mm]	V [mm]	W [mm]	V [mm]	W [mm]
0	0	0	0	0	0	0	0	0	0	0	0
-0.17808	0.374432	-0.13431	1.17437	-0.09351	0.741614	-0.24049	0.476349	-0.20448	1.21292	-0.1232	0.098689
-0.1697	0.377166	-0.12567	1.20788	-0.08541	0.782614	-0.23607	0.455517	-0.19559	1.22824	-0.12053	0.113882
-0.28772	0.674456	-0.15738	2.12581	-0.08494	1.53818	-0.42099	0.647465	-0.3006	2.07543	-0.18685	0.251318
-0.30066	0.705959	-0.15095	2.27285	-0.07191	1.66978	-0.44761	0.656881	-0.31091	2.22076	-0.19364	0.297603
-0.38666	0.851712	-0.17427	2.71324	-0.0675	2.02319	-0.58101	0.724555	-0.39008	2.57011	-0.24056	0.348295
-0.44289	0.944282	-0.18839	3.01142	-0.06036	2.29627	-0.67675	0.760705	-0.44527	2.81473	-0.27102	0.407854
-0.49437	0.983933	-0.21043	3.1771	-0.06271	2.42266	-0.7547	0.749957	-0.49621	2.93141	-0.29878	0.396391
-0.59547	1.07344	-0.24213	3.54903	-0.06496	2.78334	-0.91722	0.82691	-0.59755	3.29073	-0.35771	0.48132
-0.59889	1.09001	-0.23819	3.56457	-0.05599	2.76343	-0.91962	0.809705	-0.6018	3.30219	-0.3575	0.455317
-0.7516	1.16192	-0.29351	4.01695	-0.06448	3.15787	-1.15546	0.852793	-0.75183	3.66638	-0.44355	0.535376
-0.75846	1.18922	-0.29969	4.06698	-0.06297	3.18487	-1.16887	0.887648	-0.75856	3.69792	-0.44296	0.550831
-0.86429	1.19537	-0.33477	4.31016	-0.06491	3.4036	-1.33014	0.900995	-0.86209	3.93366	-0.49981	0.559066
-0.92097	1.22019	-0.35552	4.43748	-0.06486	3.5244	-1.41106	0.918487	-0.91472	4.02797	-0.52875	0.565678
-0.97781	1.24043	-0.37673	4.59038	-0.07001	3.64494	-1.50195	0.931405	-0.97627	4.16902	-0.56106	0.611718

Figure 6.4: Post-processed DIC Displacement Data Output

From this data, we take the displacements across the 3 spikes as shown in Table 6.3 and average them to get the actual longitudinal in-plane (V) and out-of-plane (W) displacements, as shown in Equation 6.4 & Equation 6.5 respectively.

$$\begin{array}{|c|c|c|} \hline \mathbf{P_1 - P_0} & \mathrm{V}_{1-0} = \mathrm{V}_1 - \mathrm{V}_0 & \mathrm{W}_{1-0} = \mathrm{W}_1 - \mathrm{W}_0 \\ \hline \mathbf{P_3 - P_2} & \mathrm{V}_{3-2} = \mathrm{V}_3 - \mathrm{V}_2 & \mathrm{W}_{3-2} = \mathrm{W}_3 - \mathrm{W}_2 \\ \hline \mathbf{P_5 - P_4} & \mathrm{V}_{5-4} = \mathrm{V}_5 - \mathrm{V}_4 & \mathrm{W}_{5-4} = \mathrm{W}_5 - \mathrm{W}_4 \\ \hline \end{array} \tag{6.3}$$

Table 6.3: The Displacements across the chosen 3 spikes

$$V_{avg} = \frac{\mathrm{V}_{1-0} + \mathrm{V}_{3-2} + \mathrm{V}_{5-4}}{3} \tag{6.4}$$

$$W_{avg} = \frac{\mathrm{W}_{1-0} + \mathrm{W}_{3-2} + \mathrm{W}_{5-4}}{3} \tag{6.5}$$

From these averaged displacements, we can calculate the out-of-plane deflection angle(θ) as:

$$\theta = \tan^{-1}\left(\frac{\mathrm{W}_{\mathrm{avg}}}{\mathrm{V}_{\mathrm{avg}}}\right) \tag{6.6}$$

During the test, the Vic-Snap software[45] is used to capture images for DIC. While capturing these images, it also records the force and displacement data it receives from the universal testing machine in the form of a CSV file. This is highlighted in Figure 6.5. The bold text in Figure 6.5 is the point at which the force and displacement values are zeroed.

Time_1	Time_0	Dev2/ai0	Dev2/ai1	Dev2/ai2	Dev2/ai3	Dev2/ai4	Dev2/ai5	Dev2/ai6	Dev2/ai7	Channe	Force	Displacem
139.5	139.5	-0.001	-0.0382	-10.6511	-0.0362	-0.0004	-0.0001	-0.0001	0.0433	0	-0.0405	-43.1904
140.5	140.5	0.0003	-0.0408	-10.6511	-0.0369	-0.0004	-0.0001	-0.0004	0.0427	0	-0.0433	-43.1904
141.5	141.5	-0.0007	-0.0379	-10.6511	-0.0365	-0.0004	-0.0001	0.0006	0.043	0	-0.0401	-43.1904
142.5	142.5	-0.0001	-0.0398	-10.6511	-0.0365	-0.0004	-0.0004	-0.0001	0.0433	0	-0.0422	-43.1904
143.5	143.5	-0.001	-0.0448	-10.6511	-0.0369	-0.0004	-0.0001	-0.0004	0.0433	0	-0.0475	-43.1904
144.5	144.5	0.0013	-0.0448	-10.6511	-0.0365	-0.0007	-0.0004	0.0003	0.0427	0	-0.0475	-43.1904
145.5	145.5	0.0003	0.0108	-0.0241	-0.0001	-0.0001	0.0003	0.0003	0.044	0	**0.0114**	**-0.0975**
146.5	146.5	-0.0014	0.1794	0.0861	0.0006	-0.0001	0.0003	0.0003	0.0433	0	0.1902	0.3491
147.5	147.5	-0.0004	0.1482	0.0821	0.0006	-0.0001	0.0003	-0.0001	0.0437	0	0.1571	0.3331
148.5	148.5	-0.0004	0.2452	0.1847	0.0006	-0.0004	-0.0001	-0.0004	0.044	0	0.2599	0.749

Figure 6.5: Force-Displacement Analogue Data

This displacement data for each sample is divided by its respective gauge length, as shown in Table 4.2, to get the longitudinal in-plane strain (ε_{22}). The W_{avg} value, as shown in Table 6.3, is divided by is respective Hinge Centre to Tip value (H), as shown in Table 6.2 to get the Normalized Displacement (N_w), as shown in Equation 6.2.

6.2.3. Data Interpolation and Plotting

From the normalized data, four data variables such as the Applied Force, the longitudinal in-plane strain (ε_{22}), the normalized displacement (N_w) and the out-of-plane deflection angle (θ), for each of the four samples of each sample type, as shown in Table 6.1, were exported to the OriginPro [46] graphing and analysis tool. This data was then interpolated to keep the x-axis values the same across the four samples for each sample type. The mean and standard deviation from the response of these four samples was found. The results were then plotted, as shown in section 6.3.

6.2.4. Strain Response with and without paint

A concern while using DIC for plane stress elastomeric samples was to what extent the applied paint affected the mechanical response of the samples. This was a concern as the thickness of the samples without paint was between 0.35 and 0.45 mm. The thickness of the samples with paint applied, however, was between 0.55 and 0.58 mm. Therefore, after the main panel of tests using DIC were completed, some additional tests were done to observe the strain response of the non-painted samples vs the painted samples, as can be seen in Figure 6.6

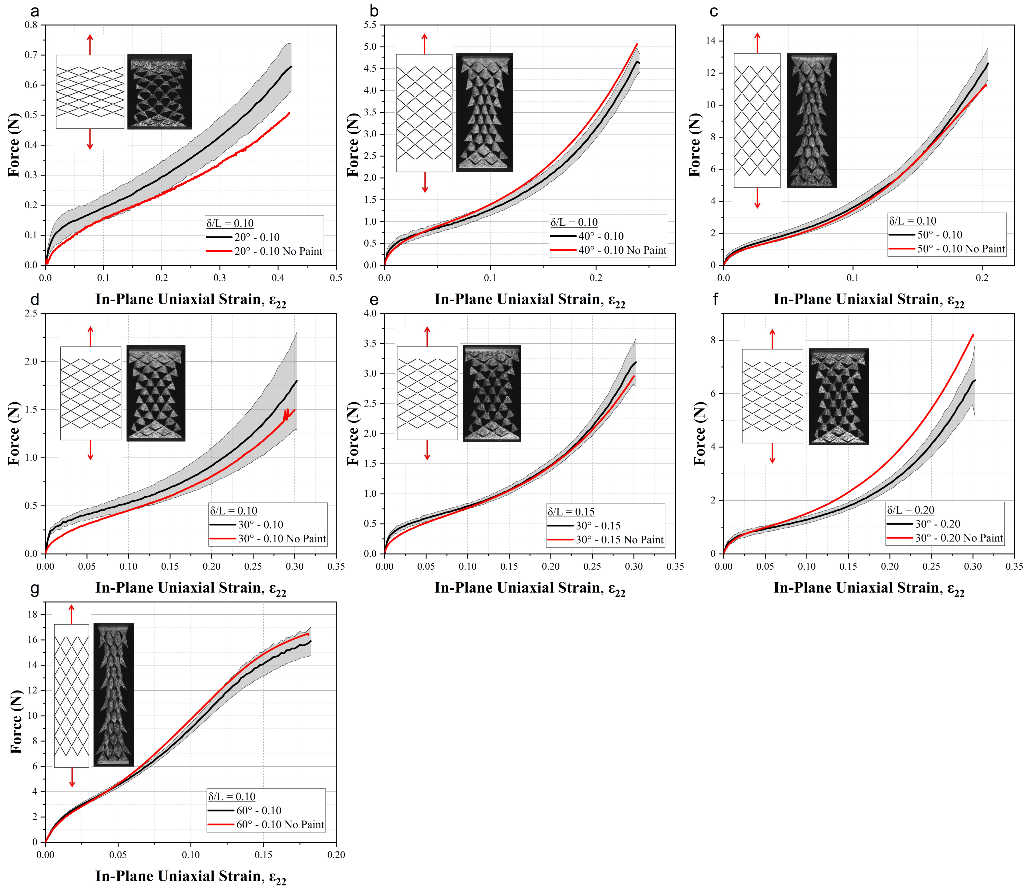

Figure 6.6: **The Applied force plotted as a function of the In-Plane Uniaxial Strain,** ε_{22}
All samples have a δ/L of 0.1 apart from figures e and f, with a δ/L of 0.15 and 0.20 respectively.
(i) The painted samples [(Shown with error bars) in grey]
(ii) The Unpainted Samples [Red]

What we observe is that in most cases, the strain response of the unpainted samples is within the range of the strain response of the painted samples. This is only not the case in Figure 6.6a and f, i.e. the 20 degree and 30 degree 0.20. This could be due to variability in prints or tiny defects. Though the 2 cases do not fit within the envelope, they still follow the same behaviour.

6.3. Out of plane Mechanical Response

The plots in Figure 6.7 and Figure 6.10 represent the main results of this thesis. They give the experimentally quantified mechanical response of the angled cut pattern, buckling-induced kirigami metasurfaces, for different cut angles (γ), shown in Figure 6.7, and show the effect of varying the δ/L ratio, shown in Figure 6.10. These resulting plots will be explained in this section, and their behaviours will be analysed.

6.3.1. Fixed δ/L = 0.10 and varying cut angles (γ)

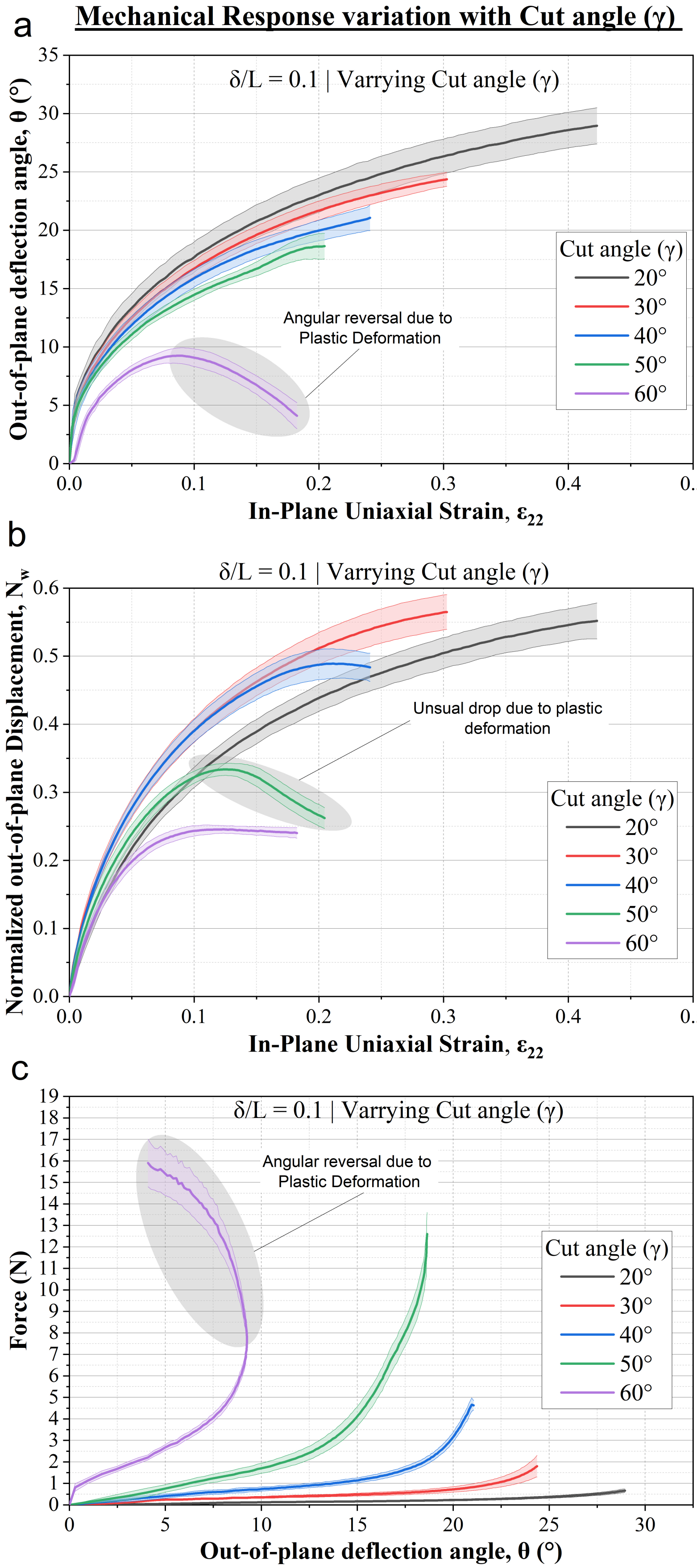

Figure 6.7: **Mechanical behaviour characterisation of the kirigami spikes for different cut angles (γ) at δ/L of 0.10**
a. Out-of-plane deflection angle, θ of the spikes plotted as a function of In-plane uniaxial strain, ε_{22}
b. Normalized Out-of-plane displacement, N_w of the spikes plotted as a function of the In-plane uniaxial strain, ε_{22}
c. The Applied force plotted as a function of the Out-of-plane deflection angle, θ

The goal of the test was to observe the sample behaviour in uniaxial, in-plane tension, and the goal was not to test to failure. Therefore, all samples have been stretched to 30 mm. This stop point of 30 mm was chosen as it was the limit of the field of view of the DIC cameras, and by this point, we observed the complete out-of-plane behaviour of the samples. However, after this 30 mm displacement, most samples began to deform plastically at the hinges and break due to tensile necking.

In Figure 6.7 a and b, we can see that all the sample types display a parabolic behaviour. The 20-degree sample being the shortest, in the 22 direction, is strained the most. In Figure 6.7 a, we observe that the 20 and 30-degree cut angle samples have an overlapping response from 0.15 to about 0.25 strain. The 20, 30 and 40-degree samples do not indicate any hints of plastic deformation. However, 50 and 60-degree samples show indications of plastic deformation. The 50-degree sample displays an unusual jump at 0.15 strain as highlighted in Figure 6.7 a. We can also observe that the out-of-plane deflection angle of the 60-degree sample decreases after a strain of 0.088. Looking at Figure 6.7 b, we can observe that the 40 and 60-degree samples begin to plateau in their normalized displacement response. However, the 50-degree samples undergo a drop in their normalized out-of-plane displacement.

If we take a look at Appendix A and the DIC contours of the 50 and 60-degree samples, i.e. Figure A.25 and Figure A.33, we can see the pictures of the samples at the start and end of the test. If we look closely at the samples, we can see an inwards collapse of the samples as the test proceeds, as shown in Figure 6.8. This happens as the spikes start to buckle out-of-plane. The distance between points c and d at the horizontal hinge ends decreases as the test goes on. After exceeding a certain displacement, the tips of the spikes stop moving further out-of-plane and the hinges collapse inwards. The whole sample forms an hourglass shape. This decreasing width during sample elongation occurs due to shear force along the length of the cut, caused by the mechanical instabilities created because of the cut geometry [8].

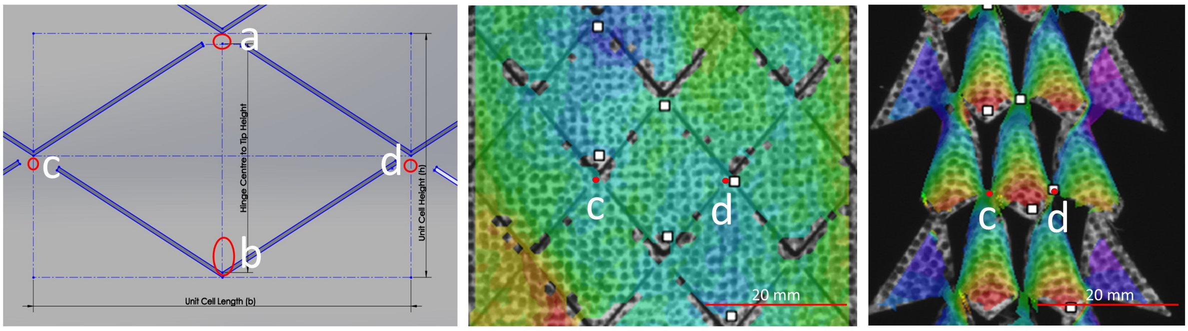

Figure 6.8: Tracking the deflection for a 50 degree sample

Looking at Figure 6.7 b, we observe that the 30-degree sample achieves the highest out-of-plane normalized displacement value compared to the other sample types and at lower strain values than even the 20-degree sample.

When we look at the Figure 6.7 c plot for force vs out-of-plane deflection angle, we observe that the greater the cut angle, the greater the applied force required for the kirigami spikes to reach a particular out-of-plane deflection angle. The 50-degree sample begins to plateau after a particular applied force, and for the 60-degree sample, we can witness a complete angular reversal after 7.5 N of force.

Observing the sample surface after testing, we can see the paint cracking at the hinge of the 60-degree sample and discolouration, as shown in Figure 6.9. This confirms that plastic deformation did happen at this location.

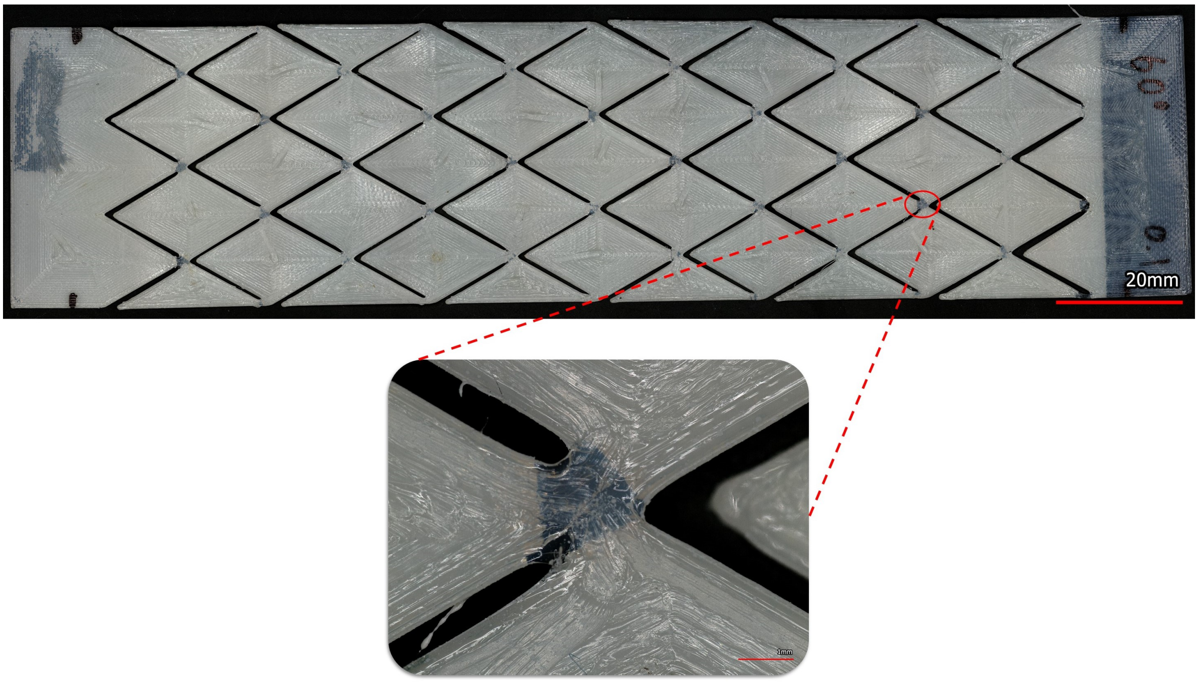

Figure 6.9: Plastic Deformation at the hinges in the 60 degree sample

The same behaviour near the hinge of the other samples was not observed in the 50-degree samples. However, it is difficult to tell as the samples have been painted over, and we cannot observe their surface similarly.

6.3.2. Fixed cut angle (γ) = 30°and varying δ/L

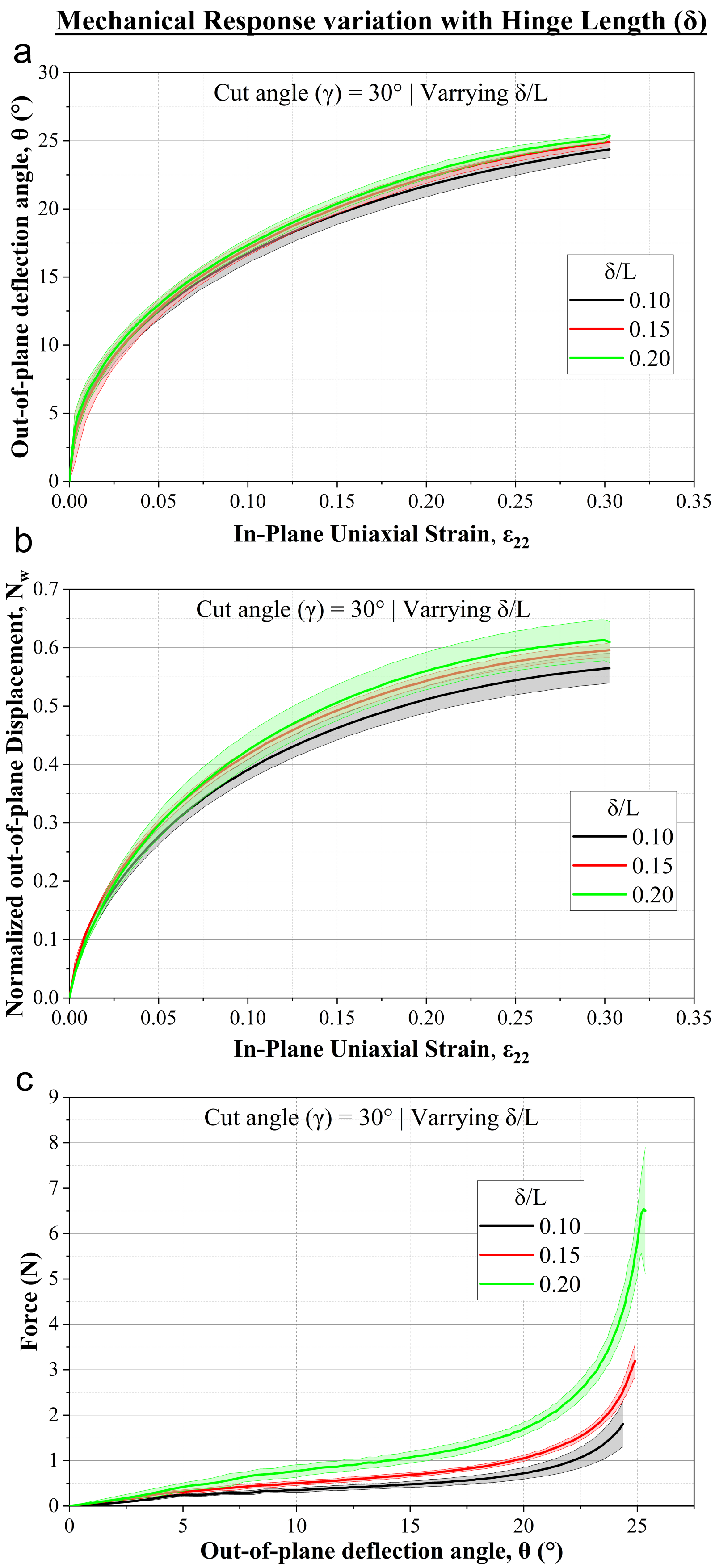

Figure 6.10: **Mechanical characterisation of the Kirigami spikes for different δ/L values at a cut angle (γ) of 30°**
a. Out-of-plane deflection angle, θ of the spikes plotted as a function of In-Plane Uniaxial Strain, ε_{22}
b. Normalized out of plane strain, N_w of the spikes plotted as a function of In-Plane Uniaxial Strain, ε_{22}
c. The Applied force plotted as a function of the Out-of-plane deflection angle, θ

In Figure 6.10, we observe the effects of increasing the hinge length (δ) while keeping the same cut angle (γ). The 30-degree cut angle was chosen for this sample type. In Figure 6.10 a and b, we observe that the deflection angle and the normalized out-of-plane displacement values progressively increase with an increase in δ/L ratio. Each progressive δ/L plot is an offset of the previous. Finally, however, they all plateau at the same strain levels.

In Figure 6.10 c, we observe a similar trend where the applied force required to reach a particular angular deflection progressively increases with increasing the δ/L ratio. The plots display a similar behaviour of being offsets of each other. However, after a deflection angle of 22.5°, the applied force increases exponentially in the case of the 0.20 δ/L samples.

It is logical that the samples with the greater hinge area would require a greater force to achieve a similar deflection since their stiffness increases. Hence, the conclusion is that increasing the hinge area would also increase the sample stiffness, and hence a proportionally greater compressive force would be required to push the spikes back downwards.

6.4. Observations regarding the effects of FFF on the bistability

The observation was made that the kirigami unit cells tended to pop in the direction of the printing. This meant the direction opposite to the flat print bed. Apart from the one-off cases where the popping was random due to defects, the predominant case was popping in the direction of the printing.

A rationale for this behaviour can be that a bias in the stability of the kirigami metasurface is created towards the printing direction due to the thickness increase as we approach the centre of a kirigami spike, as seen in Figure 6.11. This thickness increase at the centre results from the print settings where a concentric type infill was used. This causes a tendency of the nozzle to push material towards the centre while printing. Additionally, since the filament retraction option is disabled, material blobs tend to seep out during the print.

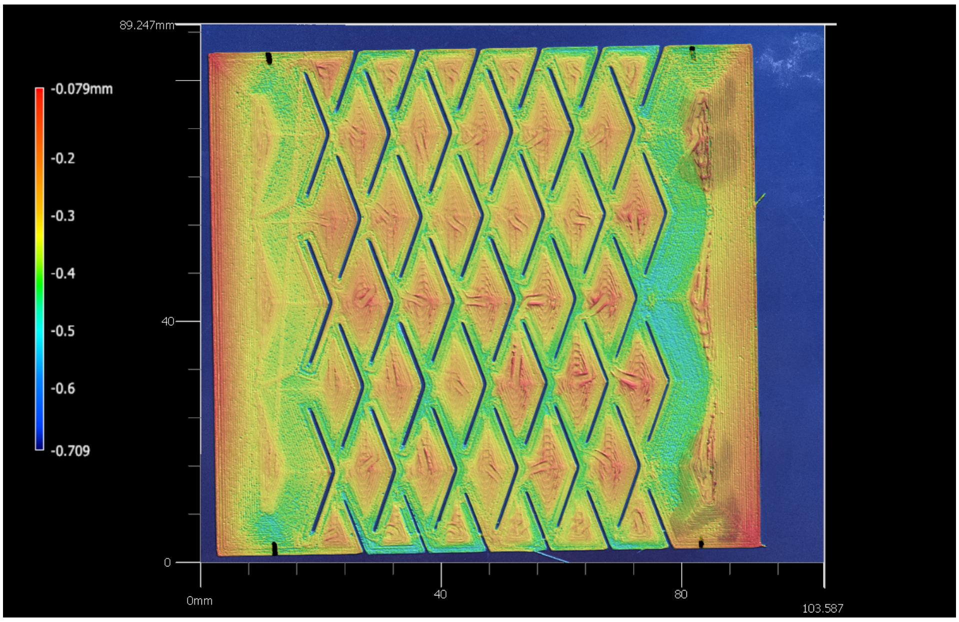

Figure 6.11: 20-Degree Sample Height Map

This print direction surface was also the surface on which paint was applied for the DIC speckling. This further increased the thickness and subsequently biased the popping of the unit cell spikes towards the print direction.

6.5. Aerodynamic Applications: Drag Force Approximation & Comparison

A use case for these elastomeric kirigami metasurfaces is drag steering and drag braking. If kept within the elastic range, such metasurfaces can be morphed in quite a controlled manner. The morphing is controlled by varying the applied force. This section investigates the potential drag force that can be generated by these angled cut, buckling-induced kirigami metasurfaces and shows how they vary with cut angle and hinge length.

The calculation of the Drag coefficient (c_d), as given by the Equation 6.7 [47], is usually done either using CFD or experimentally using a wind tunnel, where the Drag Force (F_d), can be measured.

$$c_d = \frac{2F_d}{\rho v^2 A} \tag{6.7}$$

where F_d is the drag Force, A is the reference Area and v is the velocity.

The drag coefficient Equation 6.7 is simply a rearrangement of the Drag force equation, given in Equation 6.8.

$$F_d = \frac{c_d \rho v^2 A}{2} \tag{6.8}$$

The area in Equation 6.8 is directly proportional to the Drag Force (F_d). Therefore, the amount of drag generated depends on the *frontal area of the object* [48]. Therefore, with all the other factors remaining the same, in Equation 6.8, we can use the projected area of the kirigami unit cells as the extension takes place to quantify the proportional Drag Force.

Cut Angle (°)	δ/L	Area of One kirigami spike (mm^2)
20	0.1	115.57
30	0.1	154.48
30	0.15	137.61
30	0.2	121.73
40	0.1	173.95
50	0.1	171.65
60	0.1	147.87

Table 6.4: Area of one unit cell for different sample types

Table 6.4 gives the geometrical area of a single kirigami spike for all the different sample types tested. The area is highlighted by the black lines in Figure 6.12 is this geometrical area. Only this section is considered, as it is the approximate surface that will project an area when the out-of-plane deflection of the kirigami spikes occurs.

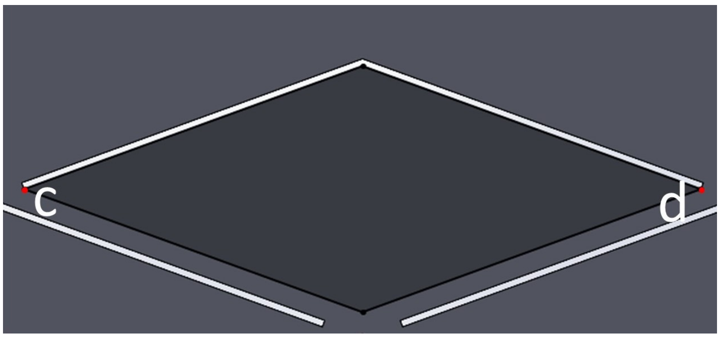

Figure 6.12: Effective geometric area of one Kirigami spike

The projected area of these kirigami spikes can be given by multiplying their geometric area with the cosine of the angle between the local surface normal and the line of sight. This angle value is given by subtracting the θ value from Figure 6.7 and Figure 6.10 from 90°, as shown in Equation 6.9. The actual projected area during extension of the sample would, however, be lesser than what is calculated. This happens as the entire kirigami spike area, as shown in Figure 6.12, would not deflect outwards. Points c and d, in Figure 6.12 would still be connected to the main sample and the actual projected area would be a curved area, as shown in Figure 6.13.

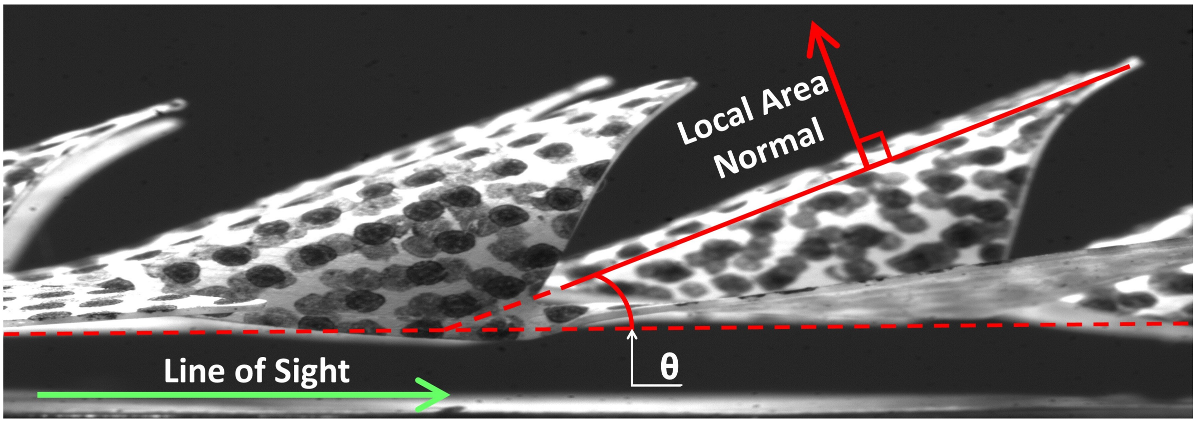

Figure 6.13: Projected area side view

Figure 6.13 shows the projected area, the line of sight and the deflection angle (θ). A rough estimate of the projected area can be calculated as follows:
A_o - Geometric Area of One Kirigami spike
A_p - Projected Area

$$\begin{aligned} A_p &= A_o \times \cos(90 - \theta) \\ &= A_o \times \sin\theta \end{aligned} \tag{6.9}$$

In the aerodynamic use case for these kirigami metasurfaces, the line of sight direction, as shown in Figure 6.13, would represent the direction of the oncoming air flow.

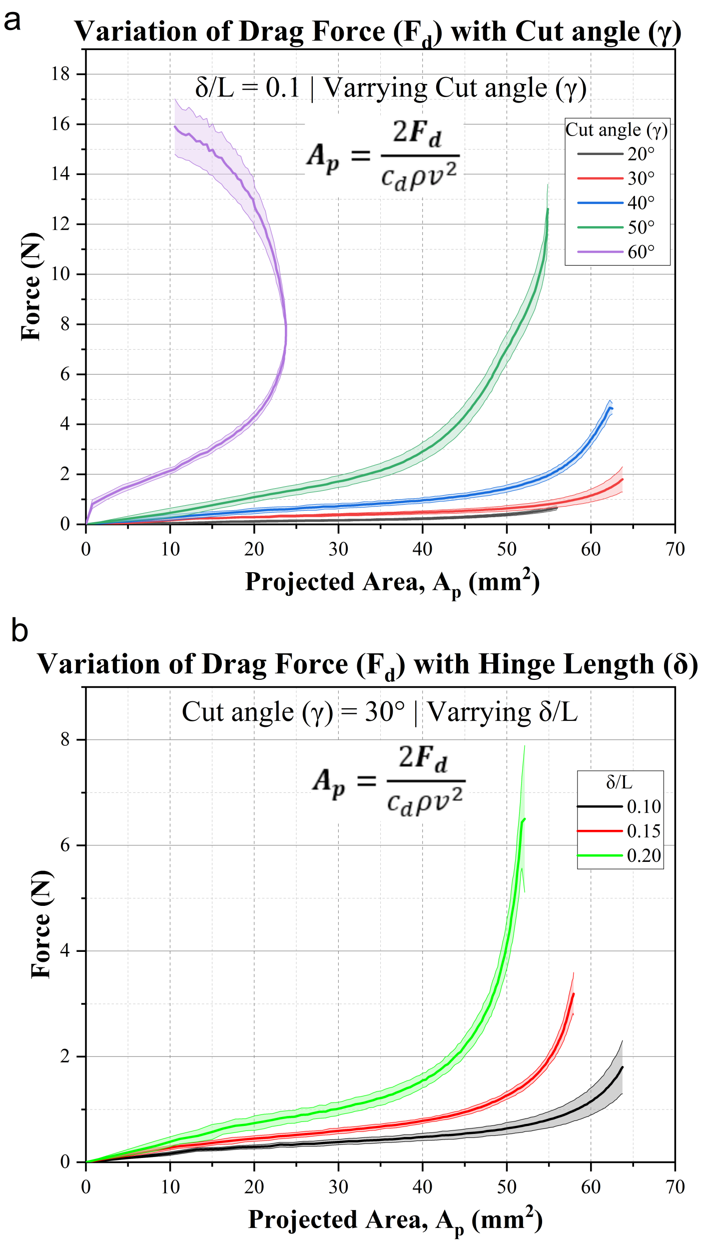

Figure 6.14: **Force Vs Projected Area to make comparisons in the proportional Drag Force**
a. The applied force plotted as a function of the projected area for different cut angles (γ) at δ/L = 0.10
b. The applied force plotted as a function of the projected area for different δ/L values at a cut angle (γ) = 30°

Using the plot obtained in Figure 6.14, we can compare the drag forces generated by different unit cell cut angles. Furthermore, we can also observe how the drag force changes with increasing the δ/L value.

We infer from Figure 6.14 a, that samples with lower cut angles can put forth a greater projected area and hence would allow for more drag force. The 30-degree sample gave the highest projected area and for a relatively low applied force. From Figure 6.14 b, We observe that increasing the δ/L ratio decreases the projected area as the characteristic Length (L) of the kirigami spike decreases. Therefore, its effective geometric area also decreases, as calculated in Table 6.4.

Taking another look at Figure 6.14 a, we can see that the 40-degree sample closely matches the maximum projected area of the 30-degree sample. The maximum projected area obtained by the 30-degree sample is 63.6 mm^2, and the maximum projected obtained by the 40-degree sample is

62.6 mm^2. We can also see that the 50-degree sample gives a slightly smaller maximum projected area than the 20-degree sample, with both hovering close to 55 mm^2. Similar to the point made about the out-of-plane stiffness in the previous section, we need to consider whether these deflected spikes could withstand such aerodynamic loads for the potential drag forces they can generate without the spikes getting pushed back downwards. In this regard, the 40 and 50-degree samples might provide greater resistance to being pushed back down by the incoming air.

Drag Force Comparison: Linear cut Vs Angled cut Unit cells

In subsection 2.2.3, we observed that the maximum calculated out-of-plane deflection angle, θ for the linear cut solar film was **39.18 degrees**. As observed in the previous section, the sample with a 30-degree cut angle gave the highest projected area. Now, if we compare a similarly sized linear cut pattern with this 30-degree angled cut pattern studied, we appropriate the cut dimensions as shown in Figure 6.15.

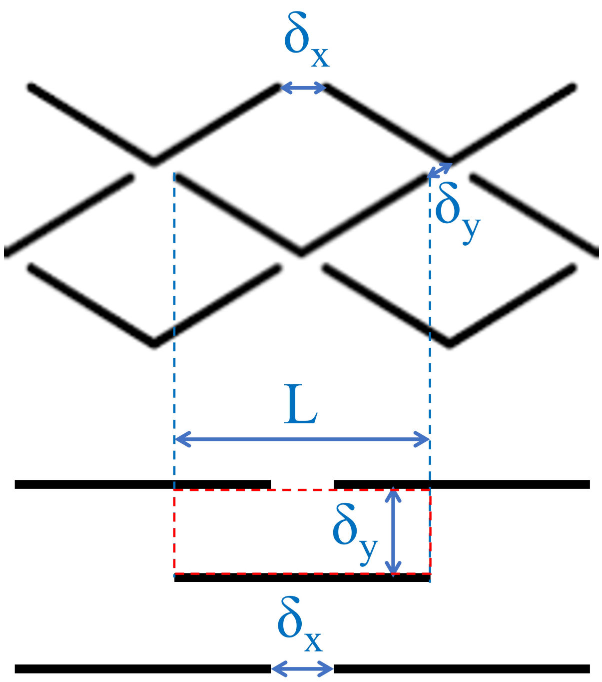

Figure 6.15: Linear cut pattern initial area highlighted in red

The characteristic length (L) of the linear cut would be 23.13 mm, the horizontal hinge length (δ_x) would be 2.60 mm, and the vertical hinge length (δ_y) would be 1.50 mm. This would ensure a similar δ/L ratio of 0.1.

The effective geometric area of one linear cut kirigami unit cell, highlighted in red in Figure 6.15, is 34.70 mm^2. Then, using Equation 6.9, the maximum projected area is calculated as **21.92** mm^2.

This maximum projected area for the 30-degree angled cut pattern kirigami sample is 63.6 mm^2. Compared to the maximum projected area of the linear cut sample, we observe a 2.90 times increase. This means that the angled cut kirigami metasurface could give a **2.90 times increase in drag force**, based on these projected area calculations alone.

7

Conclusions, Recommendations and Future Work

7.1. Conclusions

Two main research questions were posed at the beginning of this work, outlined in section 3.3. These questions have been addressed sufficiently, and certain conclusions will now be presented based on the observations and interpretations made through the course of this project.

1. What design features are achievable for angled cut pattern, elastomeric kirigami metasurface using FFF?

The main challenges that affect the manufacturing of angled cut kirigami metasurfaces using FFF AM are the slit width, the hinge length and the thickness of the surfaces. Parameters such as the slit width and surface thickness depend significantly on the print nozzle being used, i.e., the nozzle diameter. The minimum slit widths achievable depend on the minimum line width used, and the minimum thickness achievable depends on the minimum layer height used.

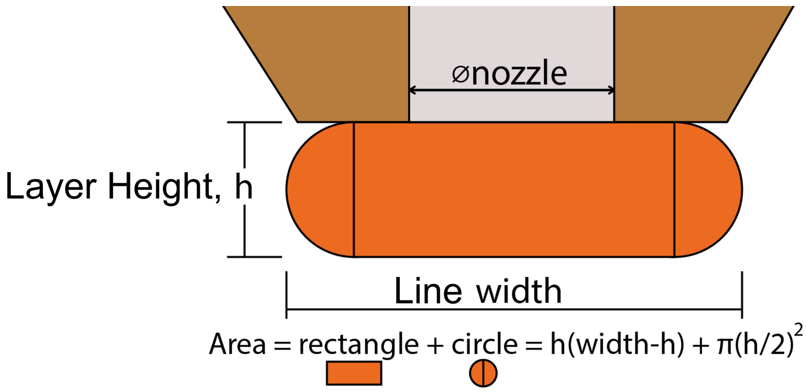

Figure 7.1: Print bead characteristics [26]

However, the line width cannot be lower than the layer height [49]; otherwise, the shape of the extruded bead becomes unpredictable. A thinner line width would give better dimensional accuracy and, therefore, the ability to achieve lower slit widths. However, a lower line width would also mean a worse bonding between adjacent print lines leading to defects such as gaps. Such gaps, when located at the hinges, will exponentially reduce the structural integrity of the kirigami metasurface. Slit width size also affects the overall area of hinges. Hence, a lower slit width is preferable, as this maximizes the hinge area that can be achieved. The minimum safe extrusion width while printing is 1.05 times the nozzle diameter (Safe, meaning it allows for sufficient bonding between consecutive extruded print beads [49]) and the minimum layer height while printing is 0.25 times the nozzle diameter. With the current 0.4 mm diameter nozzle, a minimum layer height of 0.1 mm and a minimum line width of 0.441 mm could be used. In this work, the minimum average slit width achieved was 0.5 mm, and the minimum average thickness achieved was around 0.4 mm. The term average is used because these values were inconsistent across all samples. A hinge length of 1.5 mm was achieved as the minimum that allowed for buckling before tensile failure was reached.

2. What is the mechanical response of the manufactured kirigami metasurfaces, and how does FFF affect them?

As can be observed in section 6.3, the out-of-plane behaviour of the Kirigami samples has been quantified. The effect of the cut angle on the response has been shown. The lower cut angles allow for a greater out-of-plane deflection angle. The lower the cut angle, the lower the force required to reach a particular out-of-plane deflection angle. The 30-degree cut angle sample gives the highest normalized displacement for the out-of-plane normalized displacement. The effect of increasing the δ/L ratio seems to give a slight improvement in out-of-plane deflection and displacement response. However, the applied force required to achieve this out-of-plane deflection angle response increases with increasing the δ/L ratio. This suggests that a greater hinge length would allow for stiffer samples. After their out-of-plane deflection, these samples would be more resistant to compressive loads at the spiked. The effect of the FFF manufacturing process on the kirigami metasurfaces was a bias created in the popping direction. Due to the manufacturing specifics of elastomeric TPE, an increasing thickness gradient was observed in the direction of the printing, which subsequently biased the popping of the unit cell spikes towards the printing direction. The effect of the FFF manufacturing process on the bistability of the kirigami metasurfaces was a bias created in the popping direction. Due to the manufacturing specifics of elastomeric TPE, an increasing thickness gradient was observed in the direction of the printing. This subsequently biased the popping of the unit cell spikes towards the printing direction.

3. What comparisons can be made between the area projected by linear and angled cut pattern kirigami metasurfaces?

From Figure 6.5, we observe that angled cut pattern kirigami metasurfaces put forth greater projected areas than similarly sized linear cut pattern kirigami metasurfaces. The maximum projected area of the 30-degree angled cut angle pattern kirigami metasurface was 2.9 times the maximum projected area of the linear cut pattern kirigami metasurface. Therefore, it stands to reason that the amount of drag force that can be generated by angled cut kirigami metasurfaces is much greater than the drag forces that can be generated by linear cut kirigami metasurfaces.

7.2. Significance of current work

This works also aims to be the starting point in the use of FFF additive manufacturing and the design and material deposition freedom it offers to tailor the response of the unit cells for angled cut pattern kirigami metasurfaces. The out-of-plane mechanical behaviour of these metasurfaces is experimentally characterized. The extent to which they can be strained is demonstrated, and the effect of the characteristic geometric parameters on the out-of-plane mechanical response is observed.

This work also provides a guide on how these angled-cut kirigami metasurfaces can be manufactured using FFF, the preferable printing practices, and the setting to be used. It also highlights the challenges of Digital Image Correlation for high-strain, elastomeric kirigami metasurfaces with large amounts of out-of-plane deflection behaviour. Finally, it highlights what compromises need to be made when studying these structures in such a manner and shows techniques on how to post-process and use the large amounts of data collected.

This work also makes an estimation on the drag forces that can be generated using these angled cut kirigami metasurfaces and provides a path forward on how research in this area can be extended.

7.3. Limitations and Improvements

In this section, a few limitations of the current work are identified and what steps could have been taken in the future to improve them are highlighted.

Due to the pixel size being greater than the speckle size, aliasing would occur. This speckle size to pixel size ratio being lesser than one was due to the required field of view. This large field of view was required to observe the entire sample throughout the entire test displacement of 30 mm. As an improvement, either higher resolution DIC cameras be used, or the field of view be reduced to observe a single-unit cell spike be observed throughout the global displacement of the test. This way, it would be possible to observe a finer speckle size without aliasing occurring. This would occur as the observed speckle pattern would be closer to the camera; hence, the speckle dots would be more prominent for the same pixel size.

Another limitation is the sample size. With the existing clamps available for testing, only three columns of unit cells could be used in the design of the samples to observe all cut angles required for this study. Therefore, only spikes in the central column would be independent of edge effects. As an improvement, it is suggested that horizontally longer clamps be acquired or made for such a test so that larger samples can be used. A 6 x 10 (L x H) unit cell array would be preferred for the sample sizing. This sizing would more closely imitate the Kirigami metasurface used as skins, for example: on the wings of an aircraft.

7.4. Recommendations for Future work

The following recommendations are made based on examination of this thesis research and from the experiences gained during this process. The recommendations are as follows:

1. **DIC focus on the hinge regions.** Observing the stresses at the hinge region of the kirigami metasurfaces. Using a finer speckle pattern and keeping the cameras focused on these regions, the exact strain at which plastic deformation, if at all, occurs can be ascertained.

2. **Fatigue Testing of these Elastomeric Kirigami Metasurfaces.** When strained within the elastic range, these elastomeric kirigami metasurfaces can be reused. However, after a certain number of cycles, creep, and stress relaxation can occur, as the material used is an elastomer [50]. Therefore, a fatigue test can be carried out to find the point at which creep occurs.

3. **Using a lower nozzle diameter.** If we use a lower diameter print nozzle, such as a 0.1 mm nozzle, we can achieve a layer height of 0.025 mm and an extrusion width of 0.105. This would allow for the printing of multi-layer kirigami metasurfaces with lower thicknesses and lower slit widths.

4. **Wind tunnel Test to find an accurate coefficient of Drag.** In section 6.5, approximations and rough calculations are used to determine the drag force that the kirigami metasurfaces could generate. A recommendation for future work would be to test these extended kirigami samples in a wind tunnel to find their exact drag coefficient. Observations could also be made regarding how these kirigami metasurfaces interact with lift and drag generated by the wing and whether they can help delay flow separation and aerodynamic stall.

Tailoring the response of the Kirigami unit cells by influencing or biasing the bistability

Another promising tangent for future research is tailoring the response of each or a particular kirigami spike. Using the print bead deposition and infill pattern freedom of additive manufacturing, we can use the material anisotropy along the print lines to tune the buckling behaviour of the kirigami spikes. By depositing material at different orientations inside a particular unit cell of the kirigami metasurface, we can tune its properties and determine in which direction a particular spike will buckle out-of-plane when a load is applied. Figure 7.2 shows an Abaqus model in which a grid has been applied to a single kirigami unit cell, and material orientation has been varied along the grid.

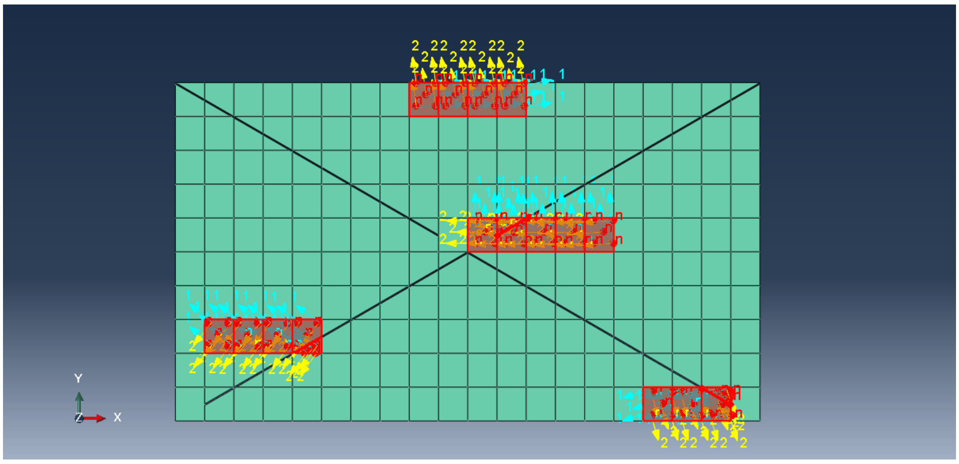

Figure 7.2: Tuning the material anisotropy in a kirigami unit cell on Abaqus

Another way to tailor the response of a kirigami spike is by varying the thickness at the hinges of the unit cells, as shown in Figure 7.3. Thickening the hinges, however, will increase the applied force required to begin the onset of buckling for the out-of-plane deflection of the spikes.

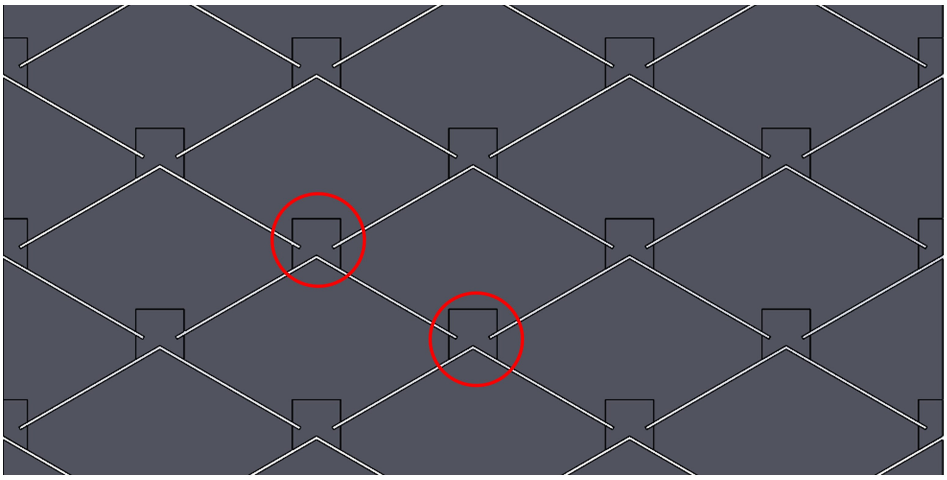

Figure 7.3: Increasing the Hinge Thickness

Bibliography

[1] *Ullagami Gallery- geometric kirigami pop-ups,* .

[2] M. K. Blees, A. W. Barnard, P. A. Rose, S. P. Roberts, K. L. McGill, P. Y. Huang, A. R. Ruyack, J. W. Kevek, B. Kobrin, D. A. Muller, and P. L. McEuen, *Graphene kirigami,* Nature **524**, 204 (2015).

[3] M. Isobe and K. Okumura, *Initial rigid response and softening transition of highly stretchable kirigami sheet materials,* Scientific Reports **6** (2016), 10.1038/SREP24758, arXiv:1604.06876 .

[4] Y. Zhang, Z. Yan, K. Nan, D. Xiao, Y. Liu, H. Luan, H. Fu, X. Wang, Q. Yang, J. Wang, W. Ren, H. Si, F. Liu, L. Yang, H. Li, J. Wang, X. Guo, H. Luo, L. Wang, Y. Huang, and J. A. Rogers, *A mechanically driven form of Kirigami as a route to 3D mesostructures in micro/nanomembranes,* Proceedings of the National Academy of Sciences of the United States of America **112**, 11757 (2015).

[5] Y. Cho, J. H. Shin, A. Costa, T. A. Kim, V. Kunin, J. Li, S. Y. Lee, S. Yang, H. N. Han, I. S. Choi, and D. J. Srolovitz, *Engineering the shape and structure of materials by fractal cut,* Proceedings of the National Academy of Sciences of the United States of America **111**, 17390 (2014).

[6] Y. Tang and J. Yin, *Design of cut unit geometry in hierarchical kirigami-based auxetic metamaterials for high stretchability and compressibility,* Extreme Mechanics Letters **12**, 77 (2017).

[7] S. Shan, S. H. Kang, Z. Zhao, L. Fang, and K. Bertoldi, *Design of planar isotropic negative Poisson's ratio structures,* Extreme Mechanics Letters **4**, 96 (2015).

[8] T. C. Shyu, P. F. Damasceno, P. M. Dodd, A. Lamoureux, L. Xu, M. Shlian, M. Shtein, S. C. Glotzer, and N. A. Kotov, *Supplementary Information A kirigami approach to engineering elasticity in nanocomposites A kirigami approach to engineering elasticity in nanocomposites through patterned defects,* (2015), 10.1038/NMAT4327.

[9] G. P. Choi, L. H. Dudte, and L. Mahadevan, *Programming shape using kirigami tessellations,* Nature Materials 2019 18:9 **18**, 999 (2019), arXiv:1812.08644 .

[10] A. Rafsanjani and D. Pasini, *Bistable auxetic mechanical metamaterials inspired by ancient geometric motifs,* Extreme Mechanics Letters **9**, 291 (2016), arXiv:1612.05988 .

[11] A. Rafsanjani, Y. Zhang, B. Liu, S. M. Rubinstein, and K. Bertoldi, *Kirigami skins make a simple soft actuator crawl,* Science Robotics **3**, 1 (2018).

[12] S. Martin and B. Bhushan, *Fluid flow analysis of a shark-inspired microstructure,* Journal of Fluid Mechanics **756**, 5 (2014).

[13] P. Motta, M. L. Habegger, A. Lang, R. Hueter, and J. Davis, *Scale morphology and flexibility in the shortfin mako Isurus oxyrinchus and the blacktip shark Carcharhinus limbatus,* Journal of Morphology **273**, 1096 (2012).

[14] S. Babaee, S. Pajovic, A. Rafsanjani, Y. Shi, K. Bertoldi, and G. Traverso, *Bioinspired kirigami metasurfaces as assistive shoe grips,* Nature Biomedical Engineering **4**, 778 (2020).

[15] M. A. Dias, M. P. McCarron, D. Rayneau-Kirkhope, P. Z. Hanakata, D. K. Campbell, H. S. Park, and D. P. Holmes, *Kirigami actuators,* Soft Matter **13**, 9087 (2017), arXiv:1707.05477 .

[16] *Journal Club for March 2021: Kirigami metamaterials as a robotic matter | iMechanica,* .

[17] Y. Yang, M. A. Dias, and D. P. Holmes, *Multistable kirigami for tunable architected materials,* Physical Review Materials **2**, 1 (2018), arXiv:1807.06498 .

[18] C. S.-s. S. Milling, *Supporting Information Combining Solid-State Shear Milling and FFF 3D Printing Strategy to Fabricate High-Performance Biomimetic Wearable Fish-Scale,* .

[19] H. Pei, S. Shi, Y. Chen, Y. Xiong, and Q. Lv, *Combining Solid-State Shear Milling and FFF 3D-Printing Strategy to Fabricate High-Performance Biomimetic Wearable Fish-Scale PVDF-Based Piezoelectric Energy Harvesters,* ACS Applied Materials and Interfaces **14**, 15346 (2022).

[20] R. Zhao, S. Lin, H. Yuk, and X. Zhao, *Kirigami enhances film adhesion,* Soft Matter **14**, 2515 (2018).

[21] T. C. Shyu, P. F. Damasceno, P. M. Dodd, A. Lamoureux, L. Xu, M. Shlian, M. Shtein, S. C. Glotzer, and N. A. Kotov, *A kirigami approach to engineering elasticity in nanocomposites through patterned defects,* Nature Materials **14**, 785 (2015).

[22] J. Nakajima, K. Fayazbakhsh, and Y. Teshima, *Experimental study on tensile properties of 3D printed flexible kirigami specimens,* Additive Manufacturing **32**, 101100 (2020).

[23] L. Gamble, A. Lamoureux, and M. Shtein, *Multifunctional composite kirigami skins for aerodynamic control,* Applied Physics Letters **117** (2020), 10.1063/5.0024501.

[24] *Textured steel sheet | Prusa Knowledge Base,* .

[25] *Vic-3D 8 Manual and Testing Guide - Correlated Solutions, Inc.* .

[26] *Layers and perimeters | Prusa Knowledge Base,* .

[27] R. J. R. J. Lang, *Origami design secrets : mathematical methods for an ancient art* (A K Peters/CRC Press, 2012) p. 758.

[28] A. Rafsanjani and K. Bertoldi, *Buckling-Induced Kirigami,* Physical Review Letters **118**, 1 (2017), arXiv:1702.06470 .

[29] N. An, A. G. Domel, J. Zhou, A. Rafsanjani, and K. Bertoldi, *Programmable Hierarchical Kirigami,* Advanced Functional Materials **30**, 1 (2020).

[30] H. Taniyama and E. Iwase, *Design of a kirigami structure with a large uniform deformation region,* in *Micromachines*, Vol. 12 (Multidisciplinary Digital Publishing Institute (MDPI), 2021) pp. 1–14.

[31] A. Rafsanjani, L. Jin, B. Deng, and K. Bertoldi, *Propagation of pop ups in kirigami shells,* Proceedings of the National Academy of Sciences of the United States of America **116**, 8200 (2019), arXiv:1905.00187 .

[32] J. P. Davim, *Materials and surface engineering : research and development* (Woodhead Publishing, 2012) p. 277.

[33] L. Wen, J. C. Weaver, and G. V. Lauder, *Biomimetic shark skin: design, fabrication and hydrodynamic function,* Journal of Experimental Biology **217**, 1656 (2014).

[34] A. W. Lang, M. T. Bradshaw, J. A. Smith, J. N. Wheelus, P. J. Motta, M. L. Habegger, and R. E. Hueter, *Movable shark scales act as a passive dynamic micro-roughness to control flow separation,* Bioinspiration Biomimetics **9**, 036017 (2014).

[35] D. P. Holmes, *Elasticity and stability of shape-shifting structures,* Current Opinion in Colloid and Interface Science **40**, 118 (2019), arXiv:1809.04620 .

[36] S. Sadik and M. A. Dias, *On local kirigami mechanics I: Isometric conical solutions,* Journal of the Mechanics and Physics of Solids **151**, 104370 (2021), arXiv:2009.03448 .

[37] S. Sadik, M. G. Walker, and M. A. Dias, *On local kirigami mechanics II: Stretchable creased solutions,* Journal of the Mechanics and Physics of Solids **161**, 104812 (2022), arXiv:2109.03019 .

[38] M. Moshe, E. Esposito, S. Shankar, B. Bircan, I. Cohen, D. R. Nelson, and M. J. Bowick, *Nonlinear mechanics of thin frames,* Physical Review E **99** (2019), 10.1103/PHYSREVE.99.013002, arXiv:1801.08263 .

[39] A. Lamoureux, *Origami and Kirigami Design Principles for Optical Tracking, Energy Harvesting, and Other Applications,* (2017).

[40] D. W. Bechert, G. Hoppe, and W. E. Reif, *On the drag reduction of the shark skin,* AIAA 23rd Aerospace Sciences Meeting, 1985 (1985), 10.2514/6.1985-546.

[41] D. Turan and J. A. Poulis, *Influence of moisture and CO2 on the material behavior of thermoplastic elastomers for beer bottle closures,* Polymer Testing **92**, 106875 (2020).

[42] C. Hopmann, C. Z. J. o. E. , and undefined 2020, *Characterisation of the quasi-static material behaviour of thermoplastic elastomers (TPE) under consideration of temperature and stress state,* journals.sagepub.com **2020**, 199 (2020).

[43] S. B. Munteanu and C. Vasile, *SPECTRAL AND THERMAL CHARACTERIZATION OF STYRENE-BUTADIENE COPOLYMERS WITH DIFFERENT ARCHITECTURES,* undefined (2005).

[44] *123-3D Filament flexibel transparant 1,75 mm TPE 0,5 kg (Jupiter serie) 123-3D 123-3d.nl,* .

[45] *Vic-Snap - Correlated Solutions, Inc.* .

[46] *Origin: Data Analysis and Graphing Software,* .

[47] *The Drag Coefficient, NASA,* .

[48] *Effect of Size on Drag , NASA,* .

[49] *Slic3r Manual – Flow Math,* .

[50] K. Yamaguchi, A. G. Thomas, and J. J. Busfield, *Stress relaxation, creep and set recovery of elastomers,* International Journal of Non-Linear Mechanics **68**, 66 (2015).

A

Appendix A - Out of plane displacements

Out of plane displacements & Data collection points of the tested samples

This appendix shows the digital image correlation (DIC) contours of the out of plane displacements (W) for the tested samples. In addition, the data collection points used for sampling the results are also demarcated on these contours. For each sample tested, these contours and data collection points are displayed at the start and end of the test.

Samples with δ/L= 0.1

20 Degree Samples

1

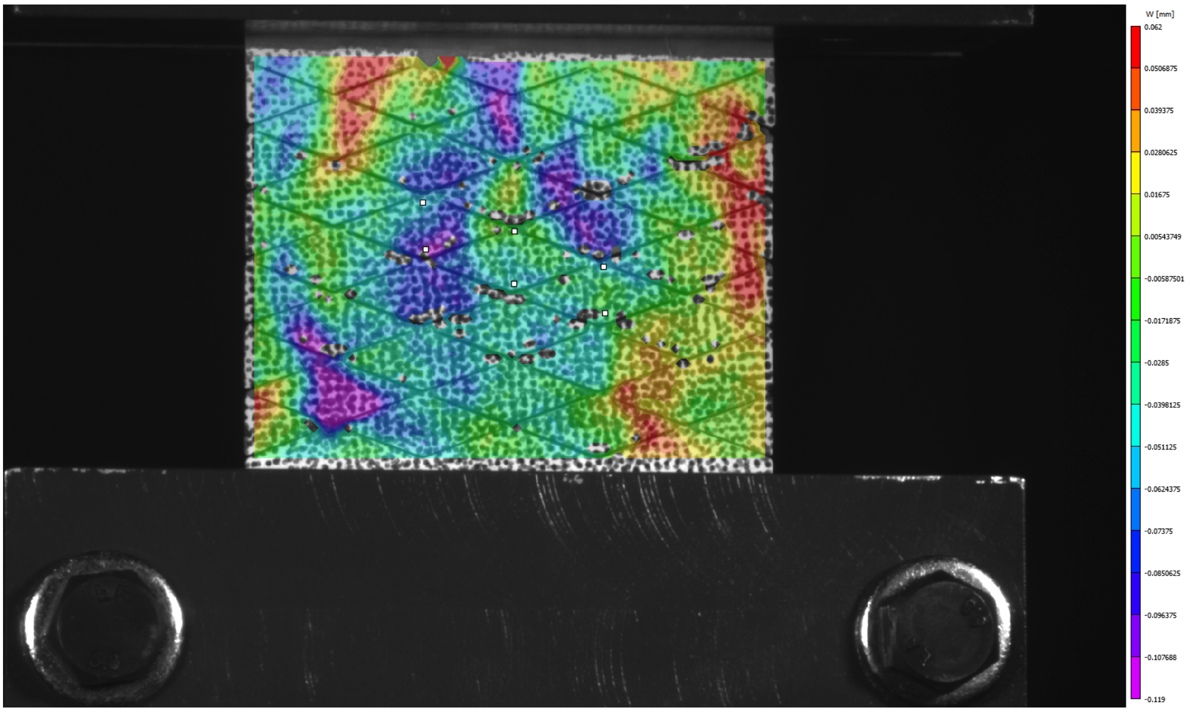

Figure A.1: 20 degree cut angle sample 1 Start

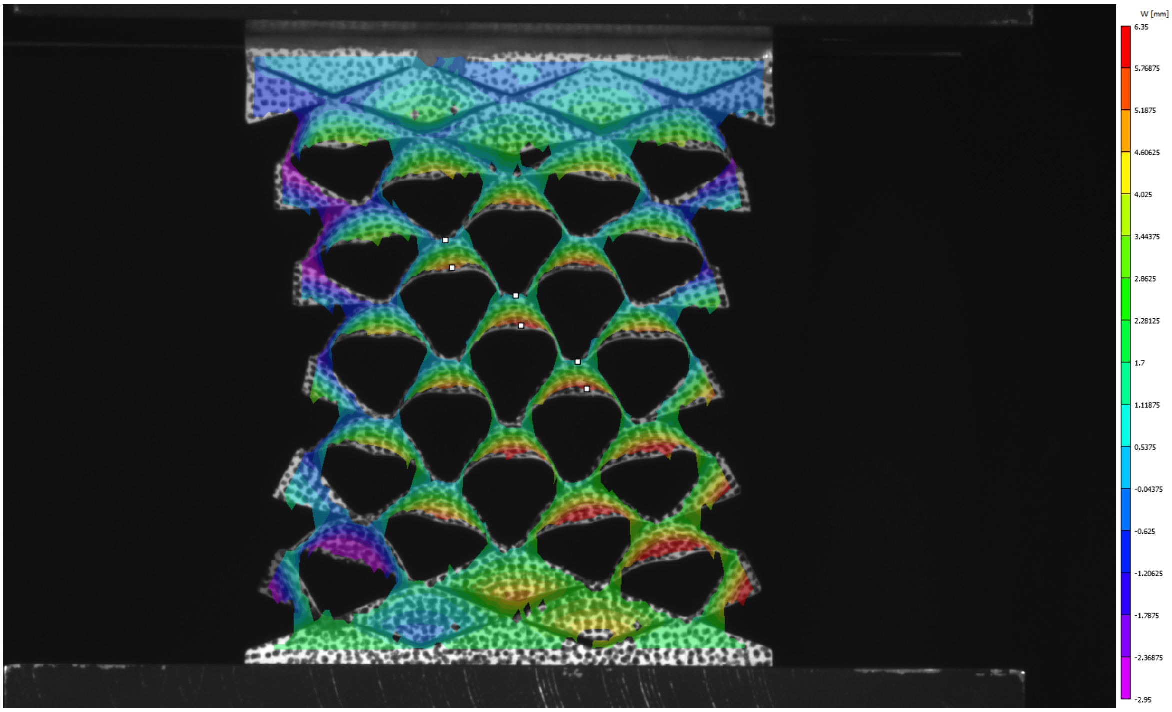

Figure A.2: 20 degree cut angle sample 1 End

2

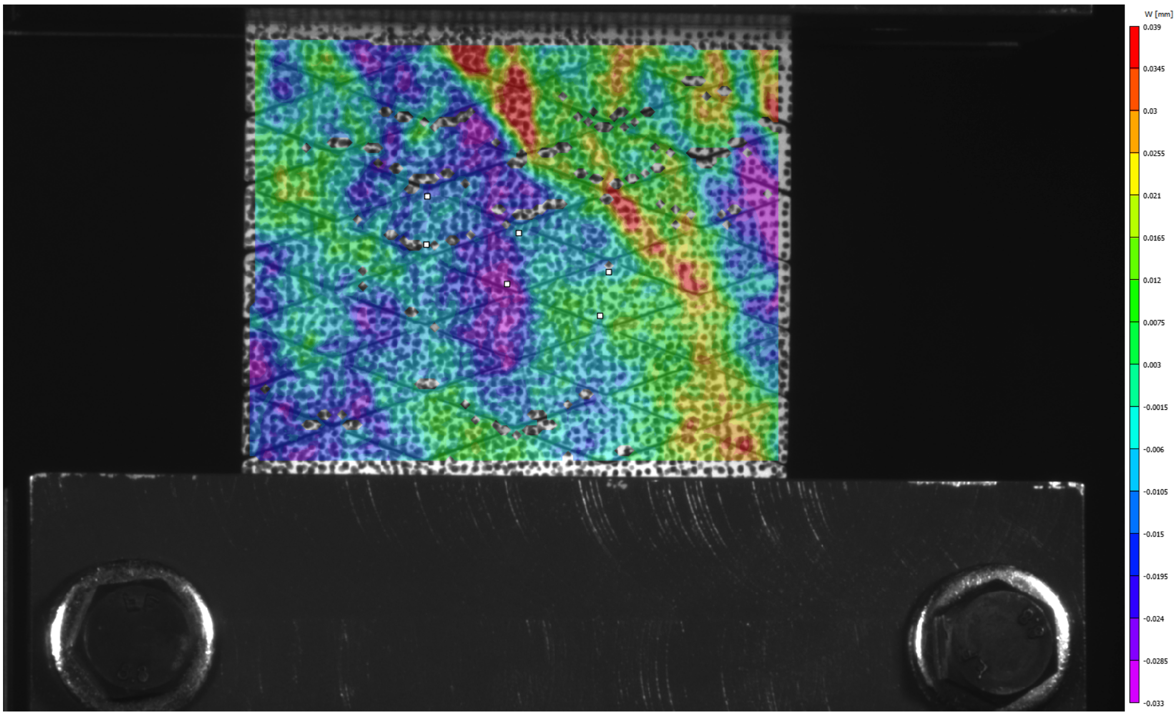

Figure A.3: 20 degree cut angle sample 2 Start

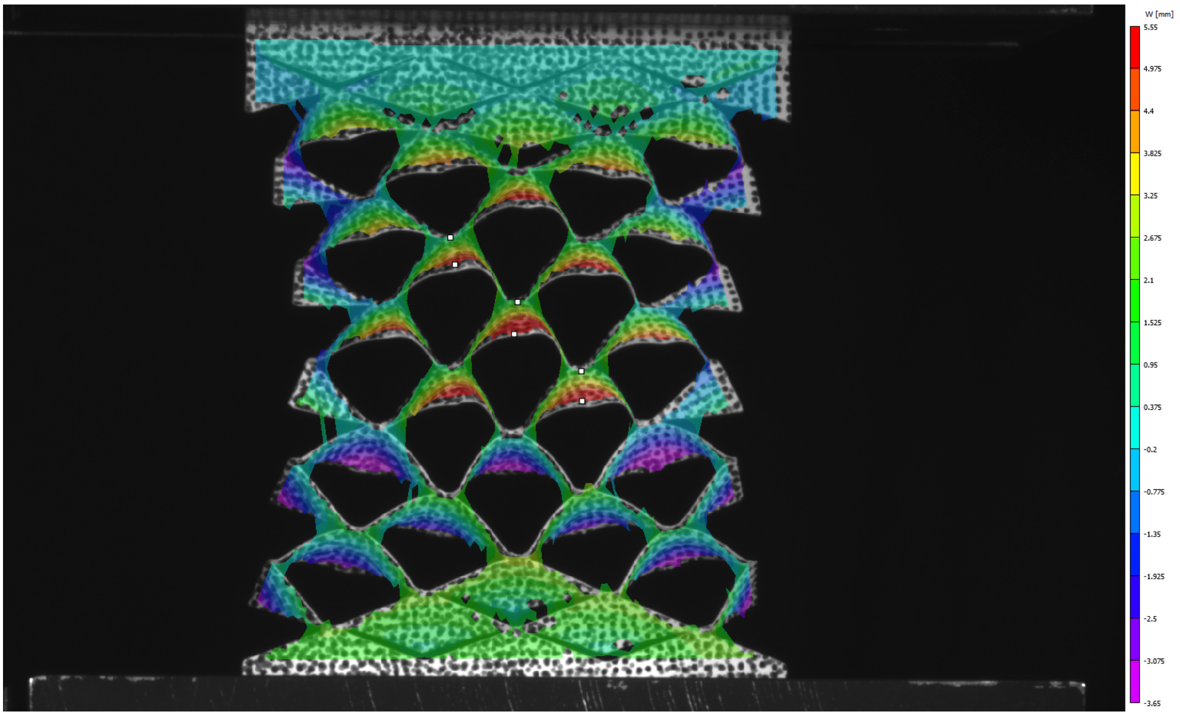

Figure A.4: 20 degree cut angle sample 2 End

3

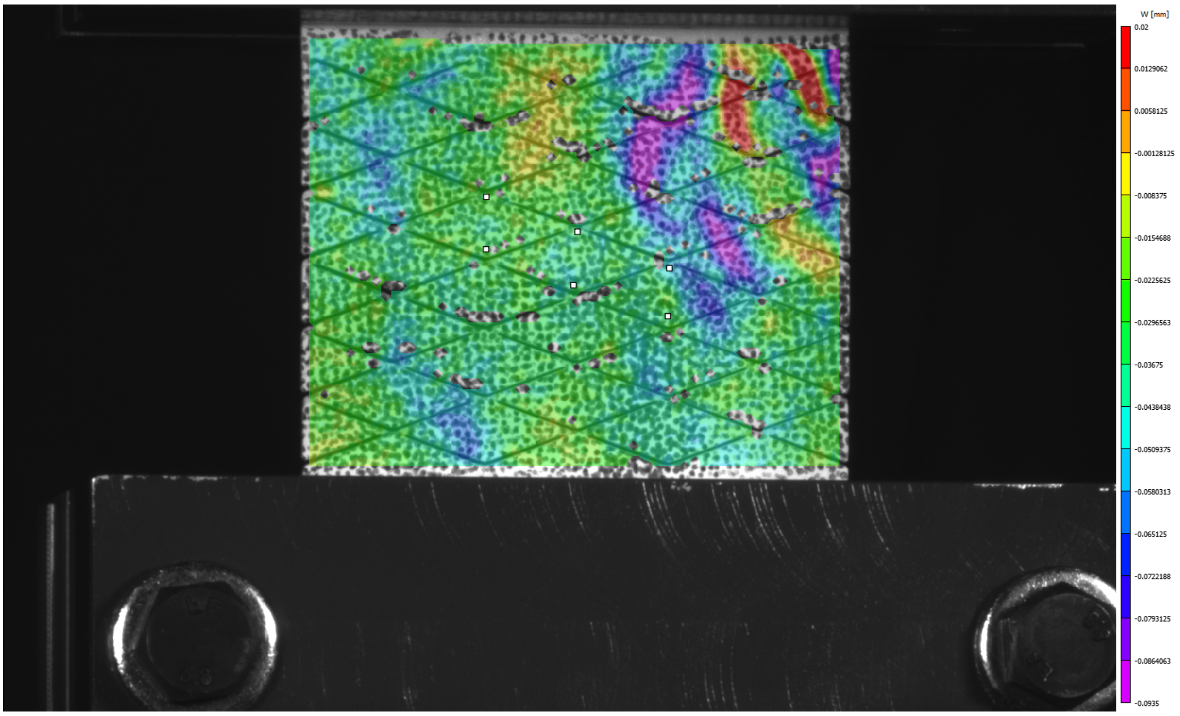

Figure A.5: 20 degree cut angle sample 3 Start

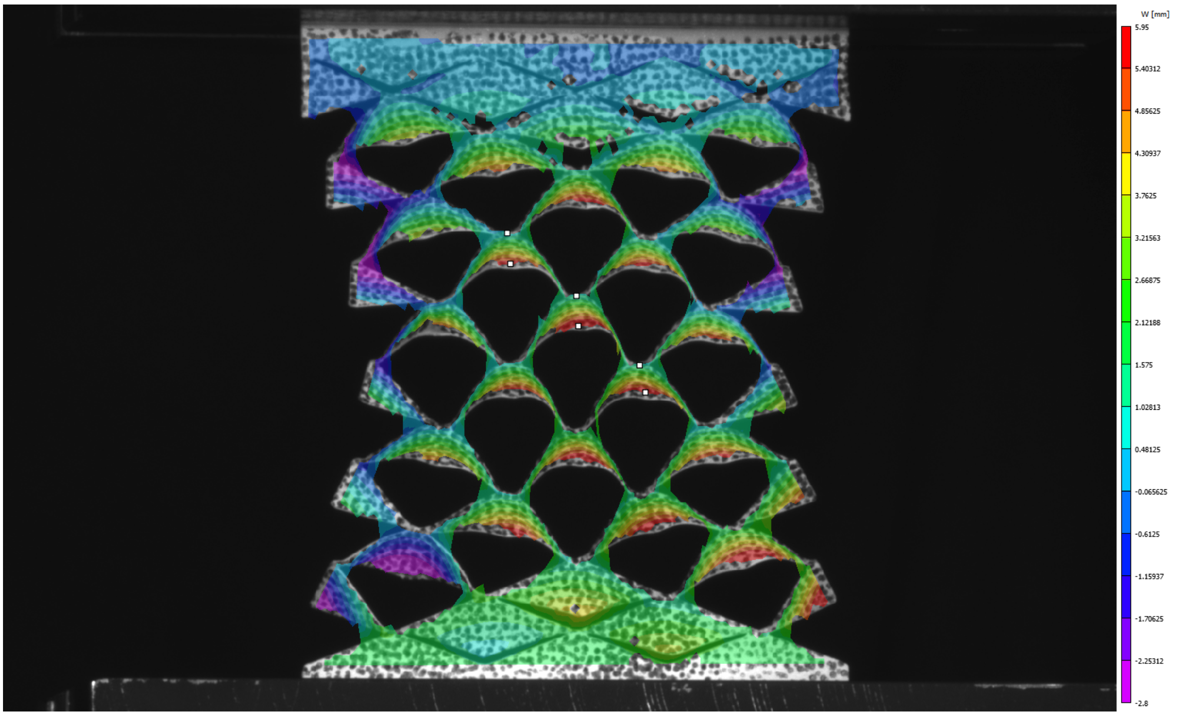

Figure A.6: 20 degree cut angle sample 3 End

4

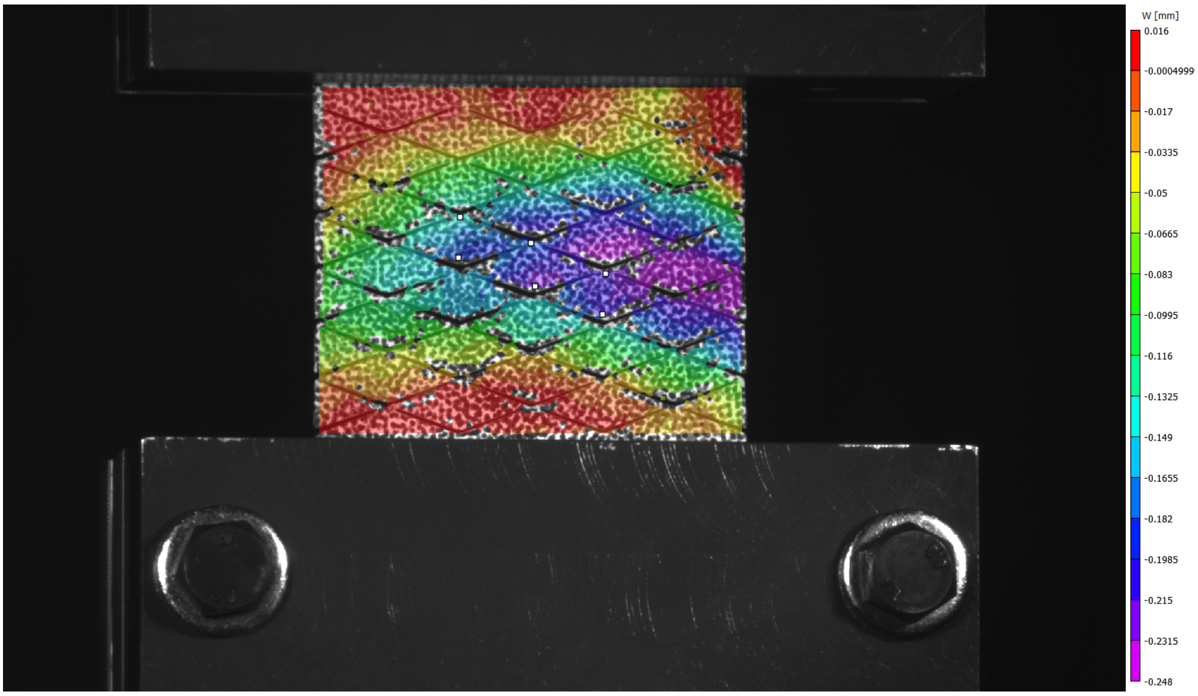

Figure A.7: 20 degree cut angle sample 4 Start

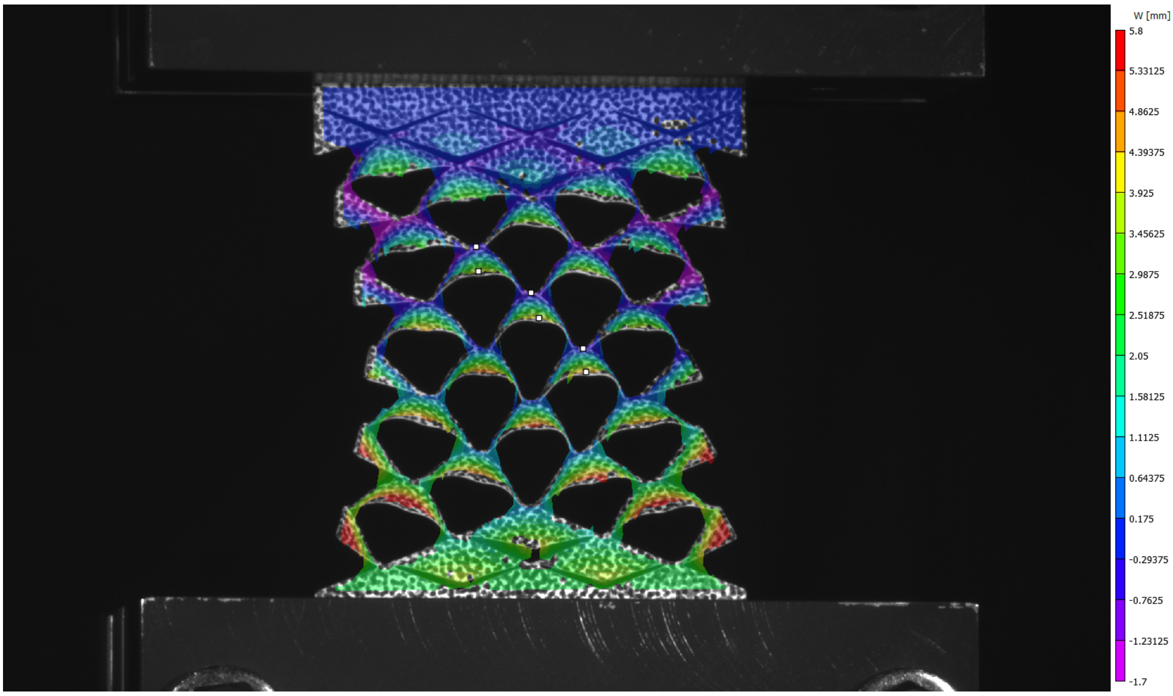

Figure A.8: 20 degree cut angle sample 4 End

30 Degree Samples

1

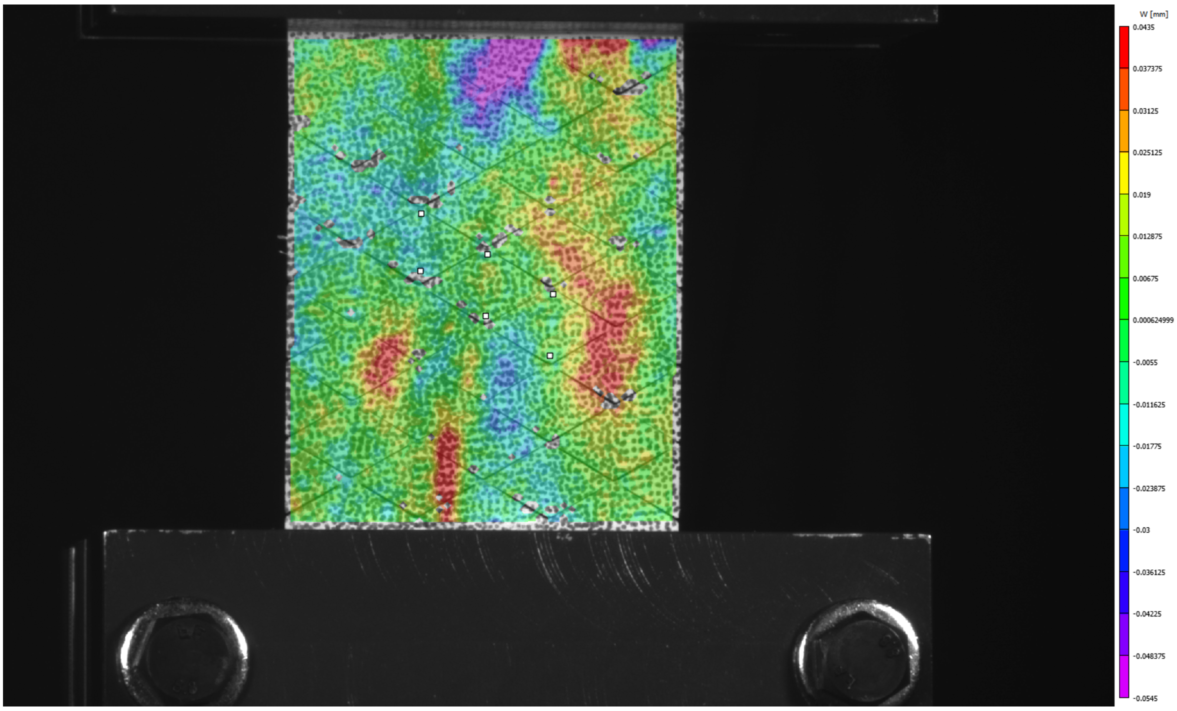

Figure A.9: 30 degree cut angle sample 1 Start

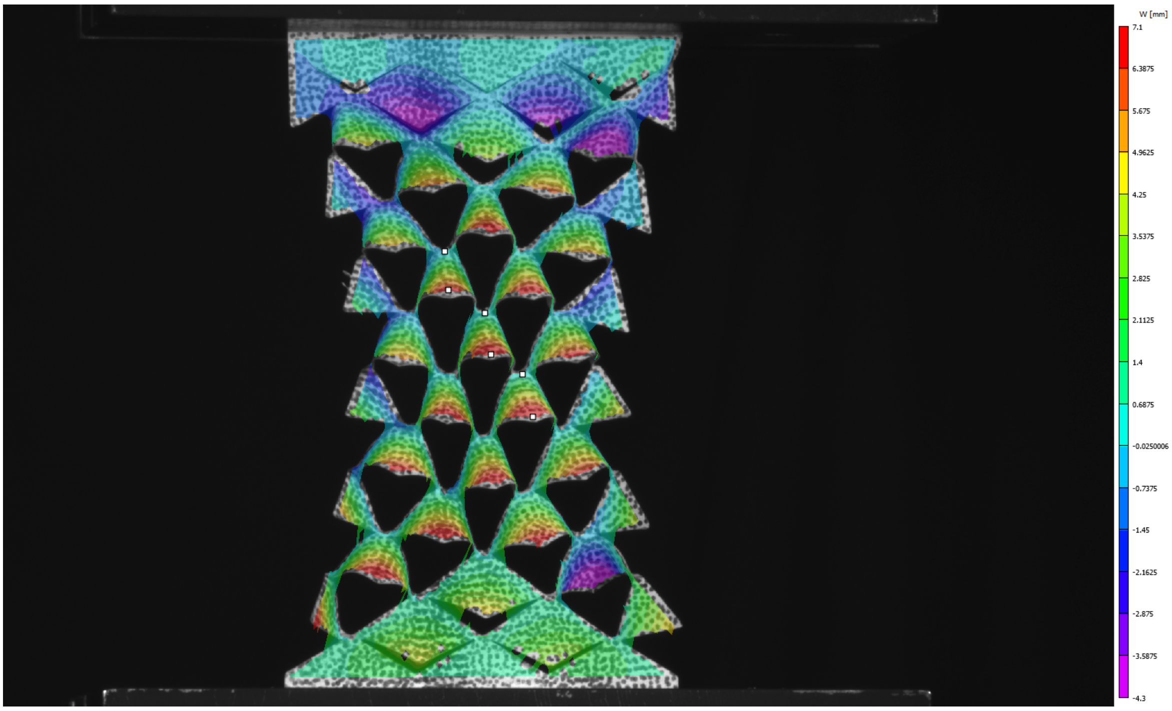

Figure A.10: 30 degree cut angle sample 1 End

2

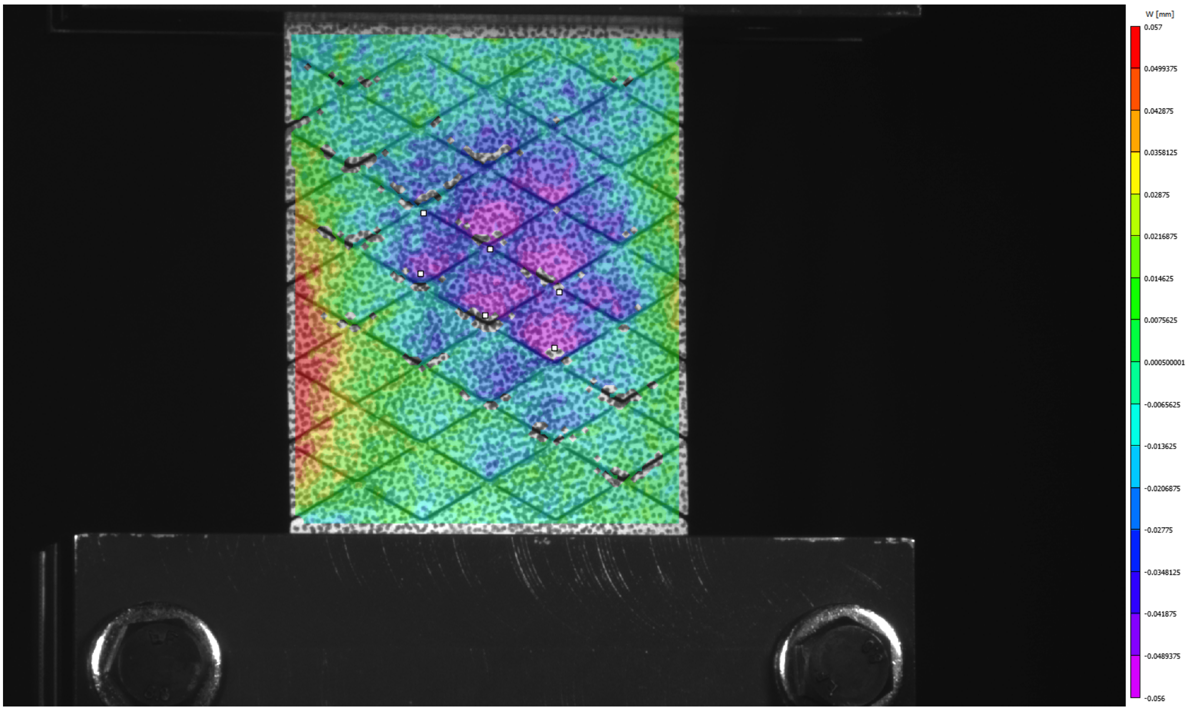

Figure A.11: 30 degree cut angle sample 2 Start

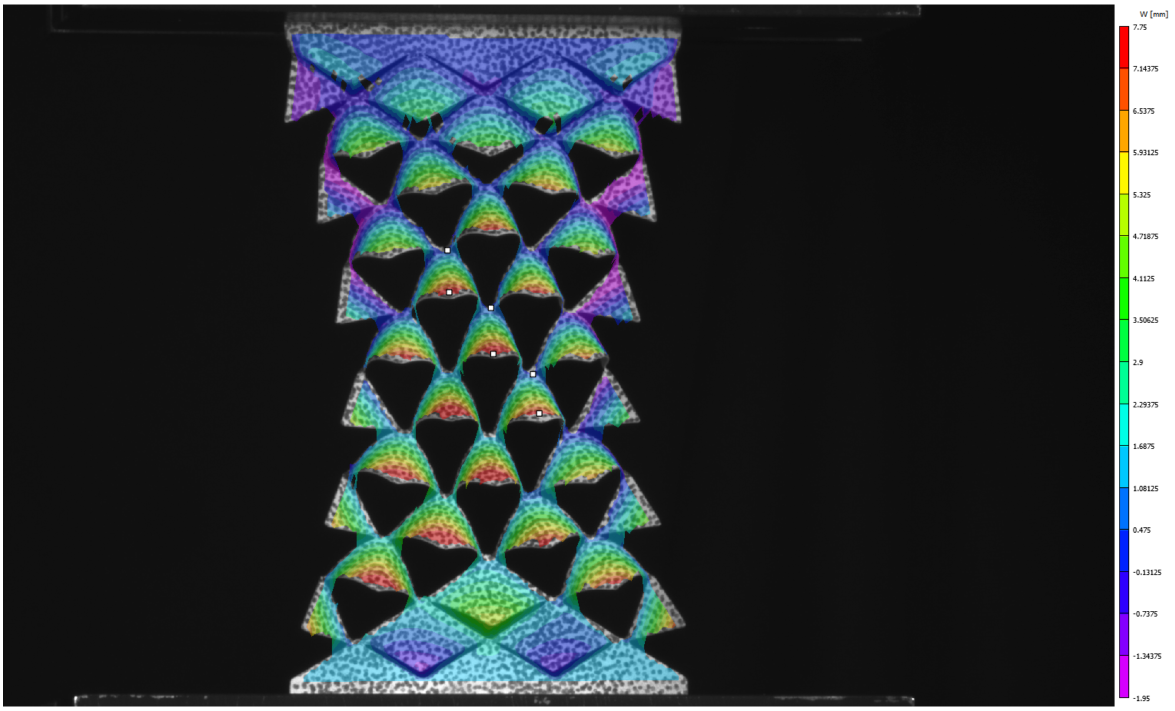

Figure A.12: 30 degree cut angle sample 2 End

3

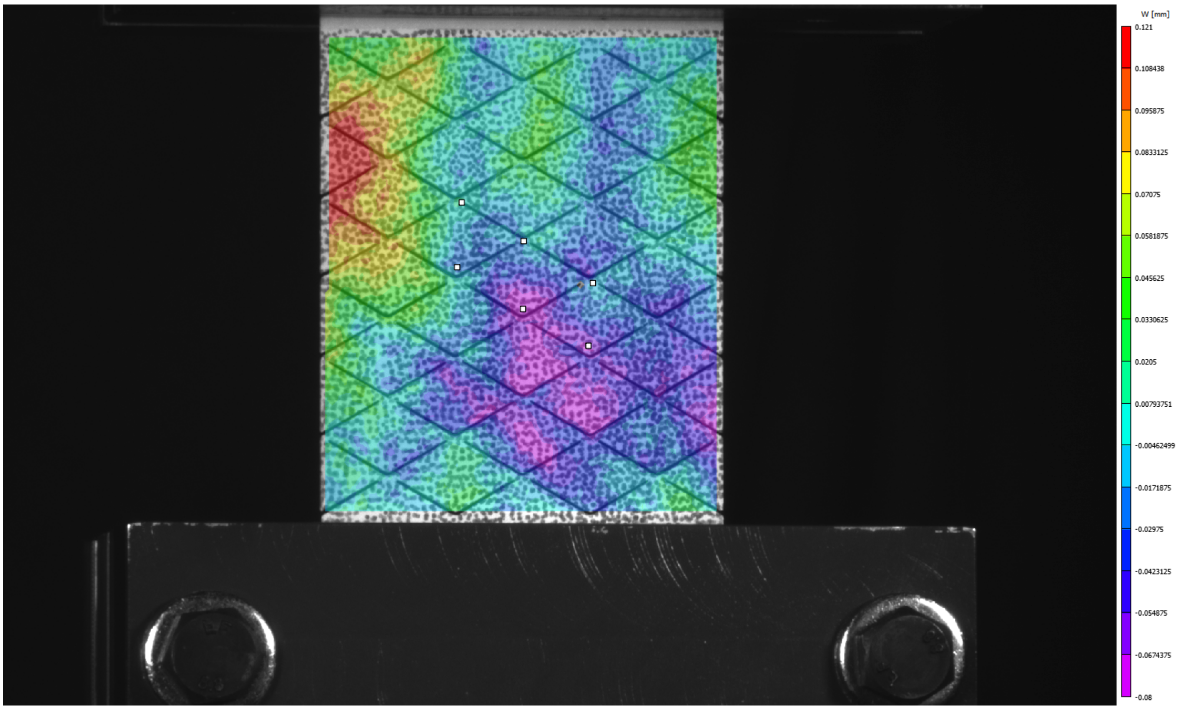

Figure A.13: 30 degree cut angle sample 3 Start

Figure A.14: 30 degree cut angle sample 3 End

4

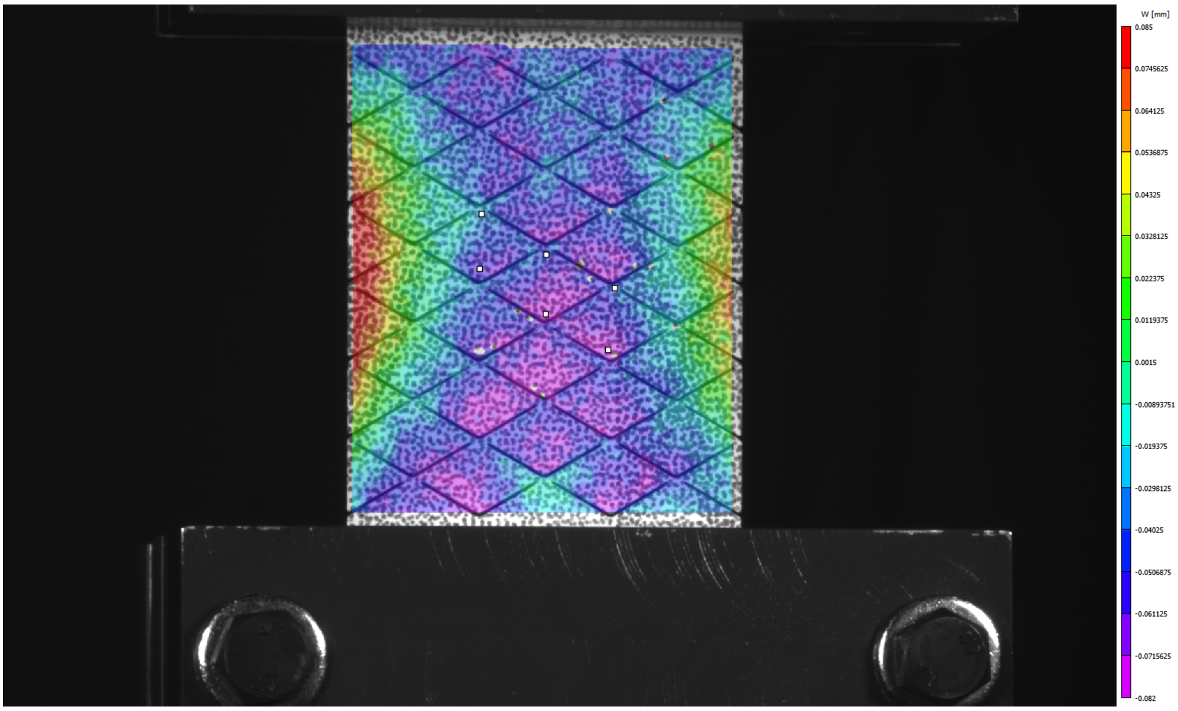

Figure A.15: 30 degree cut angle sample 4 Start

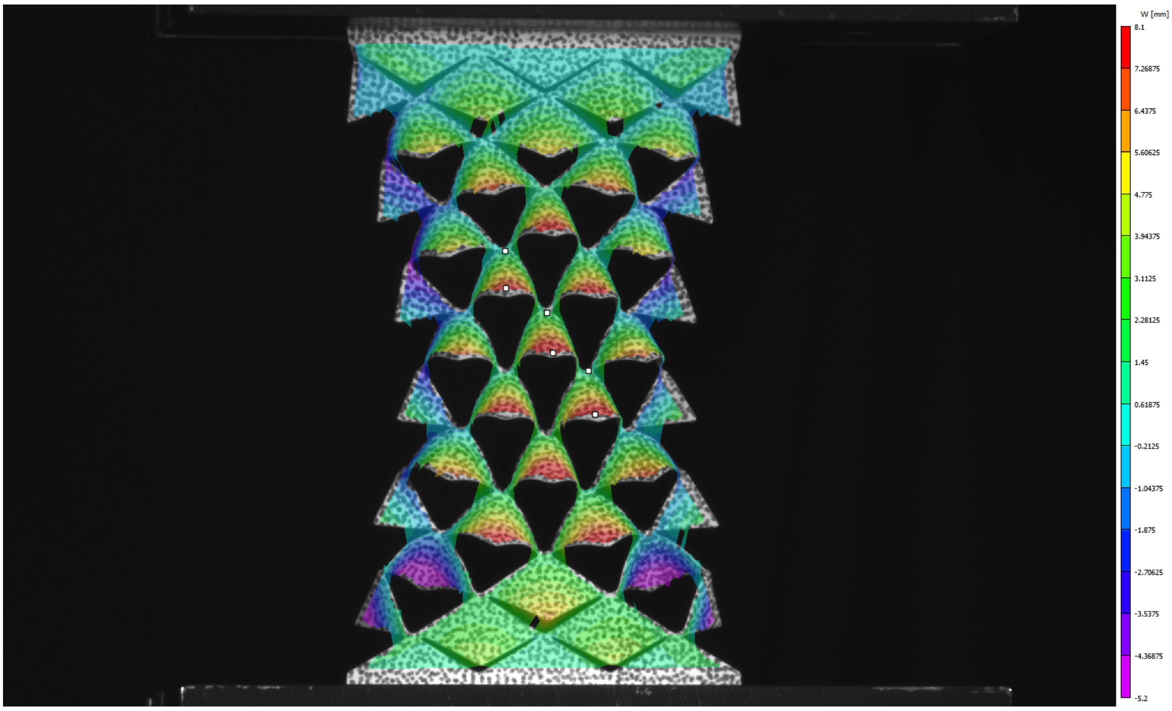

Figure A.16: 30 degree cut angle sample 4 End

40 Degree Samples

1

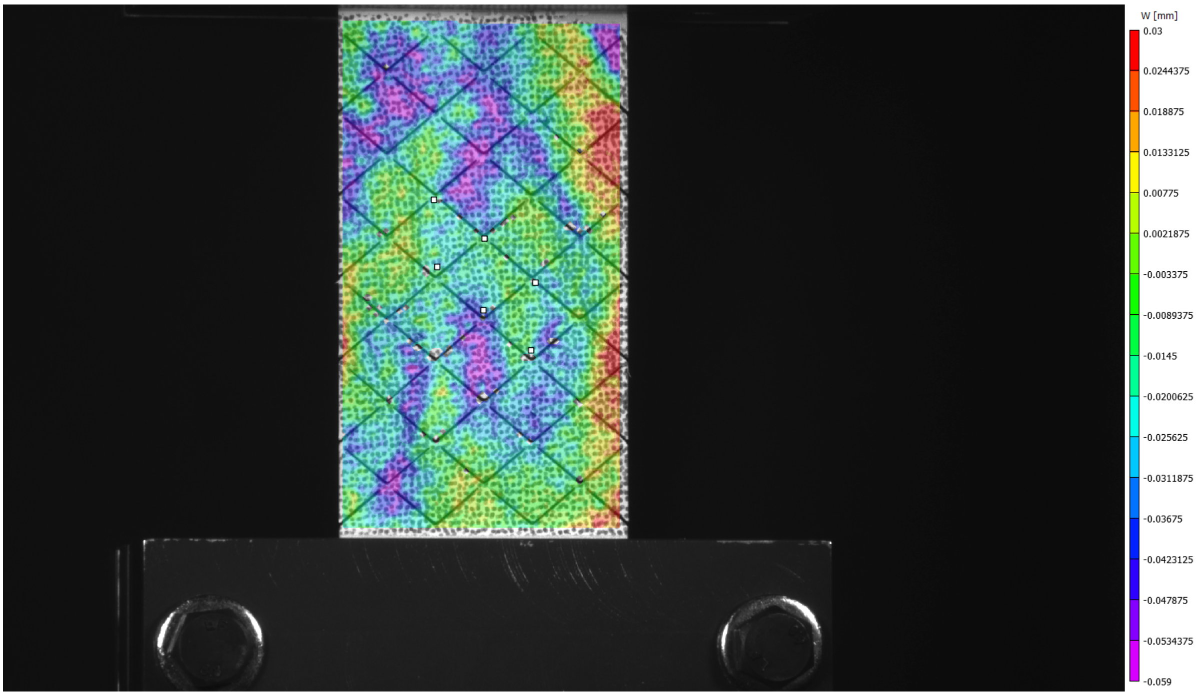

Figure A.17: 40 degree cut angle sample 1 Start

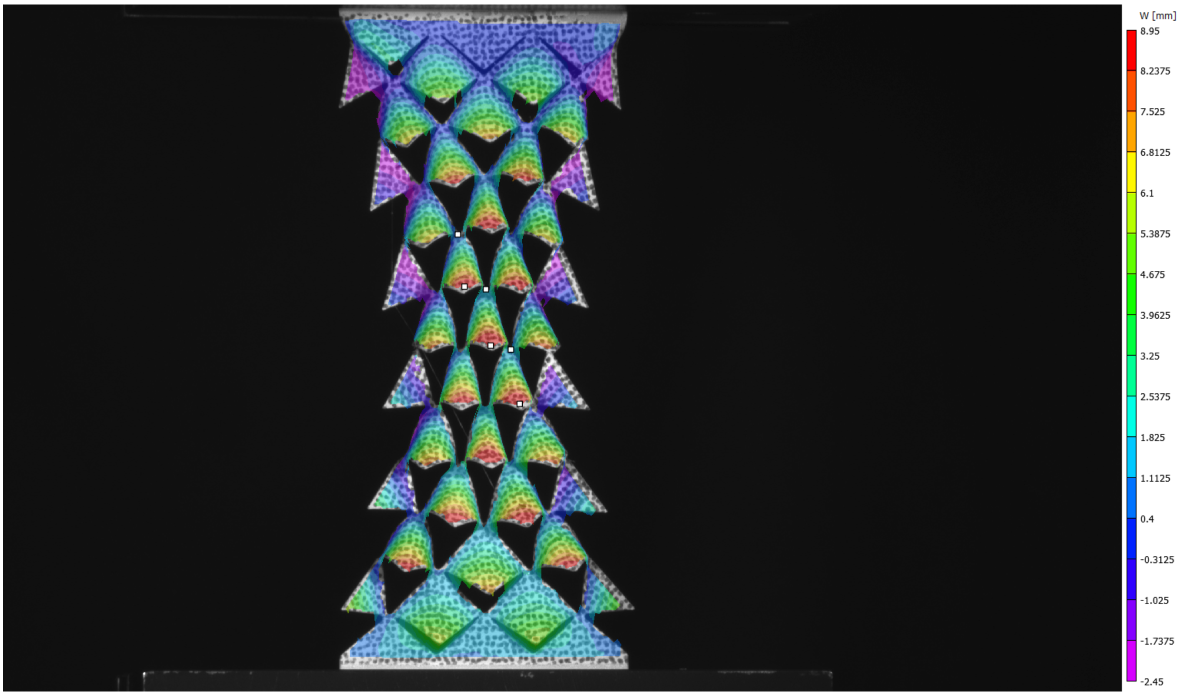

Figure A.18: 40 degree cut angle sample 1 End

2

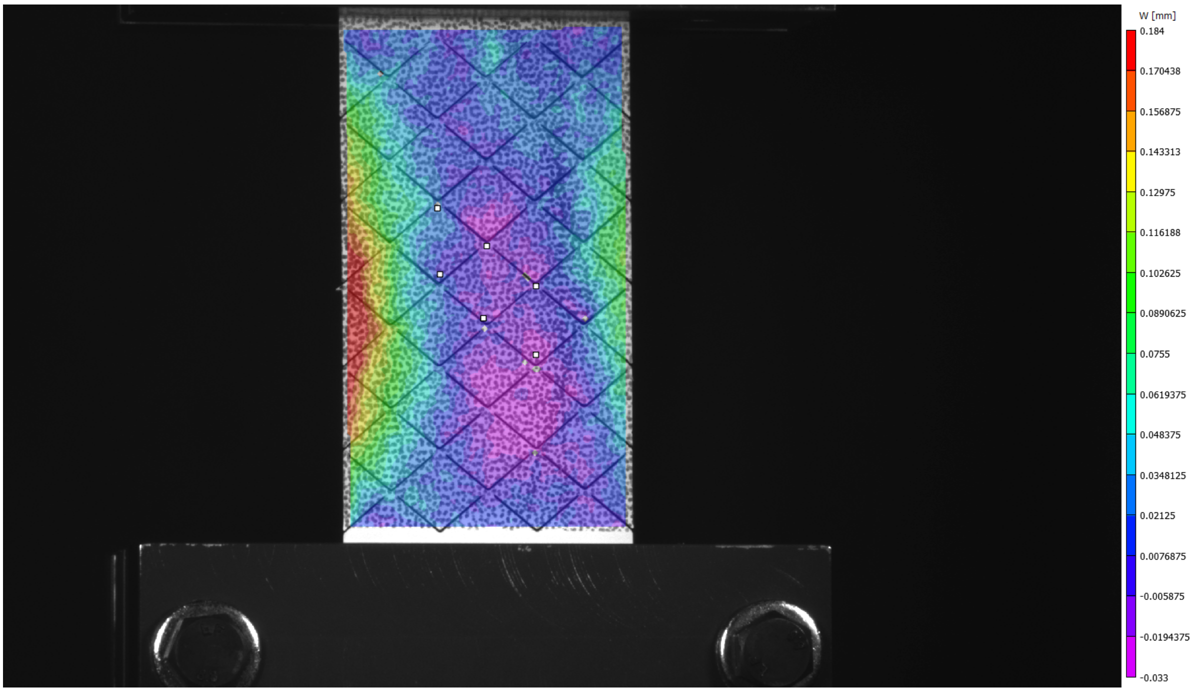

Figure A.19: 40 degree cut angle sample 2 Start

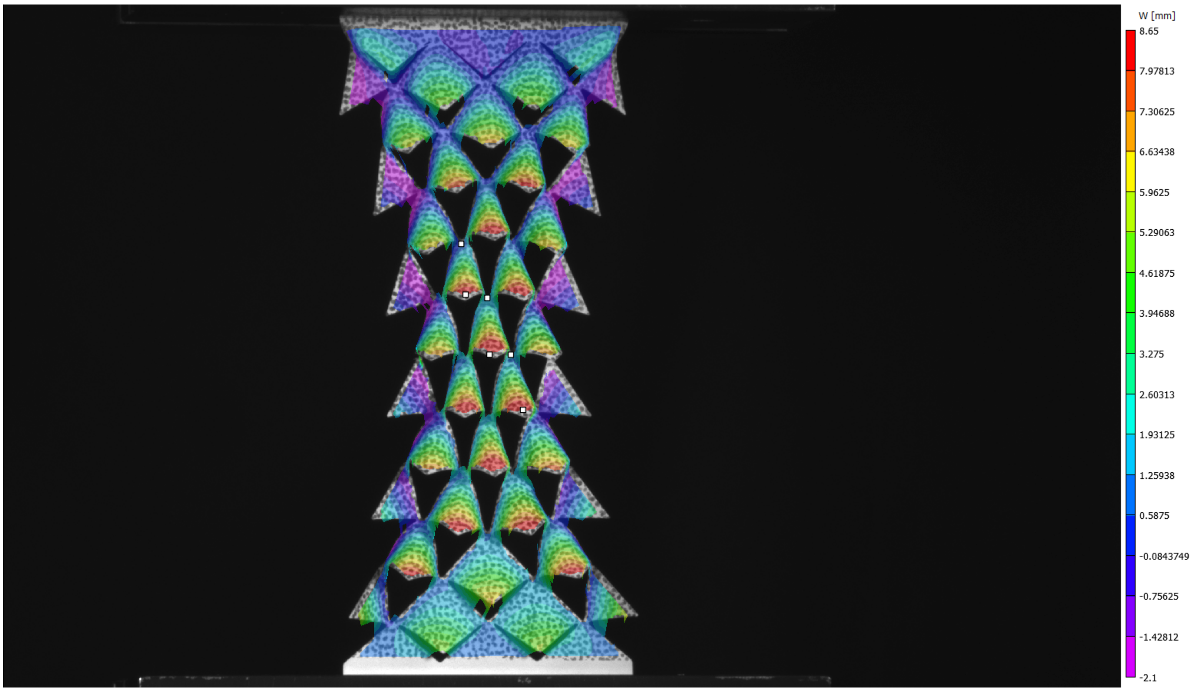

Figure A.20: 40 degree cut angle sample 2 End

3

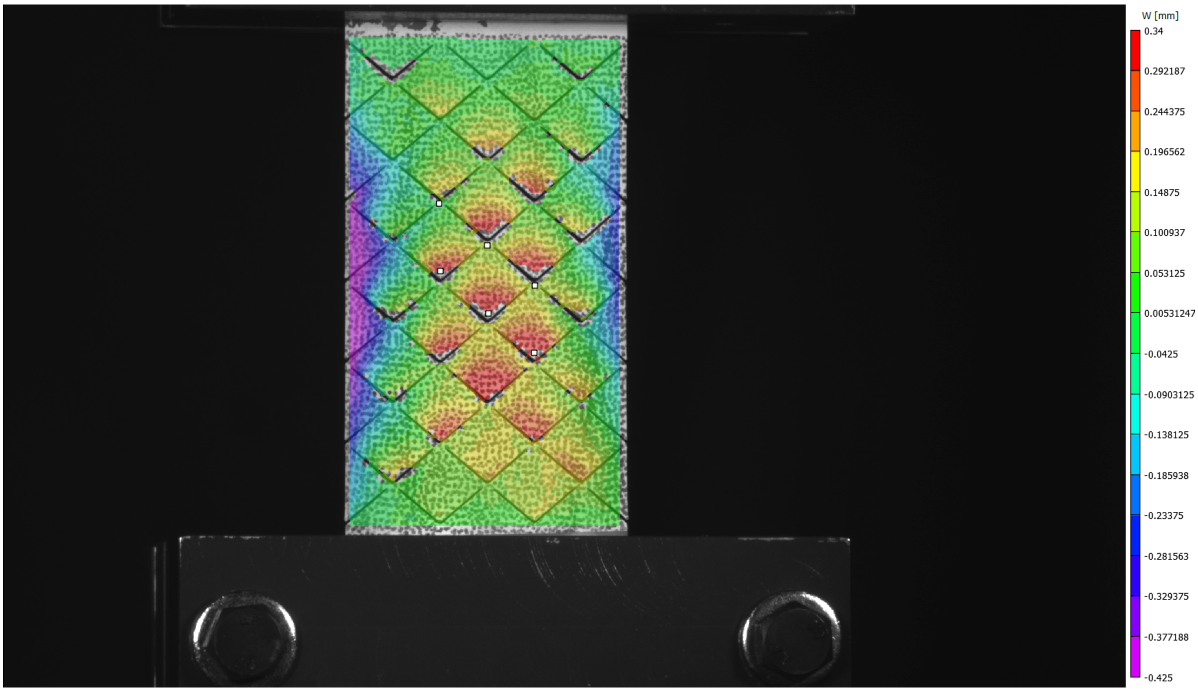

Figure A.21: 40 degree cut angle sample 3 Start

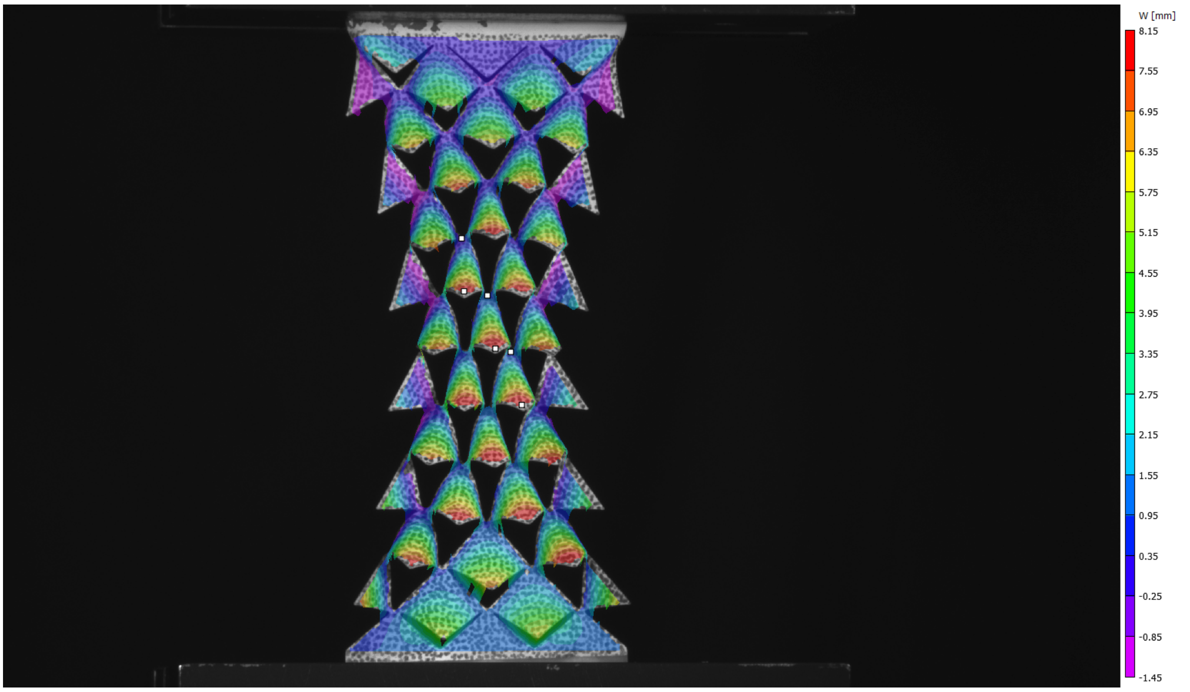

Figure A.22: 40 degree cut angle sample 3 End

4

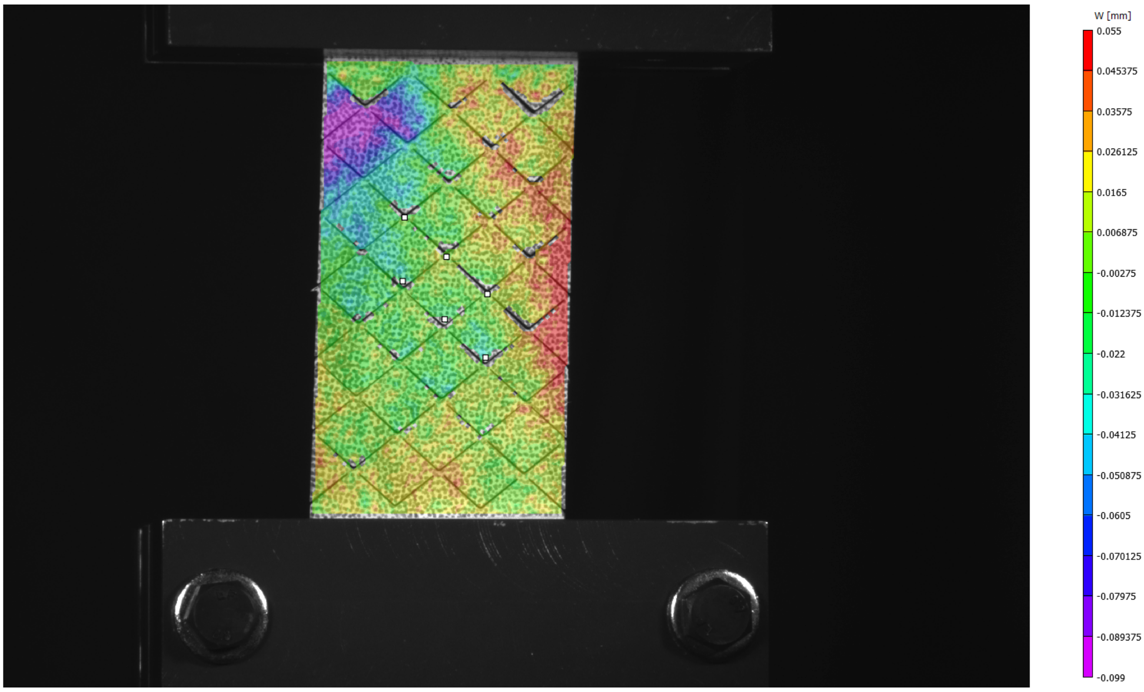

Figure A.23: 40 degree cut angle sample 4 Start

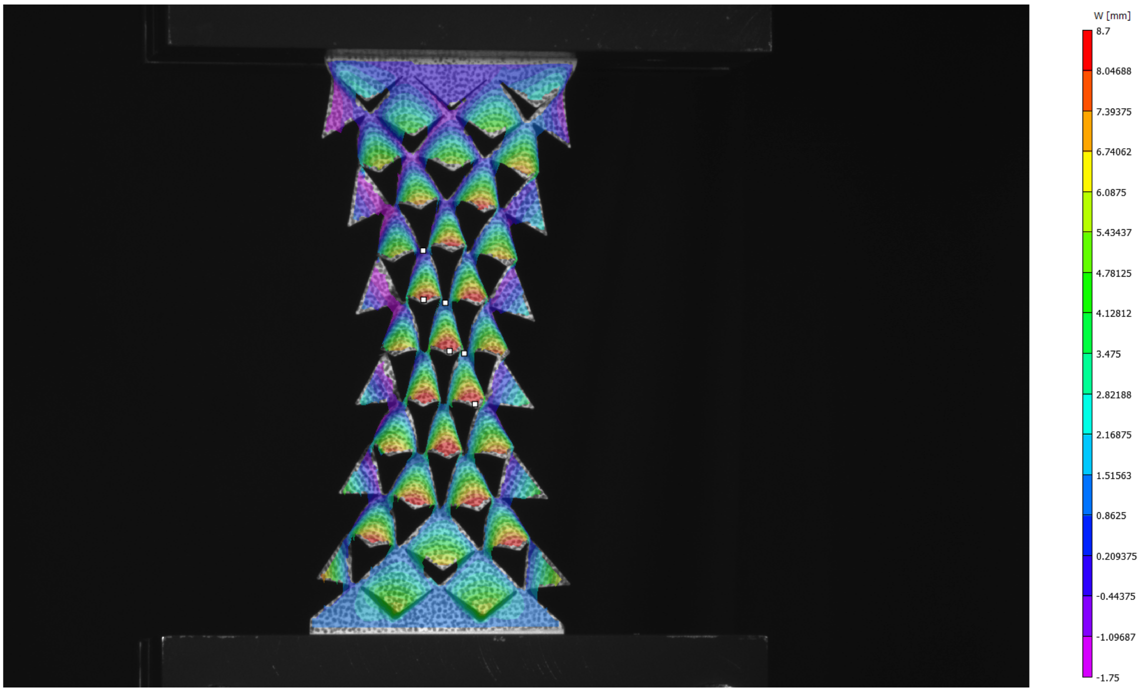

Figure A.24: 40 degree cut angle sample 4 End

50 Degree Samples

1

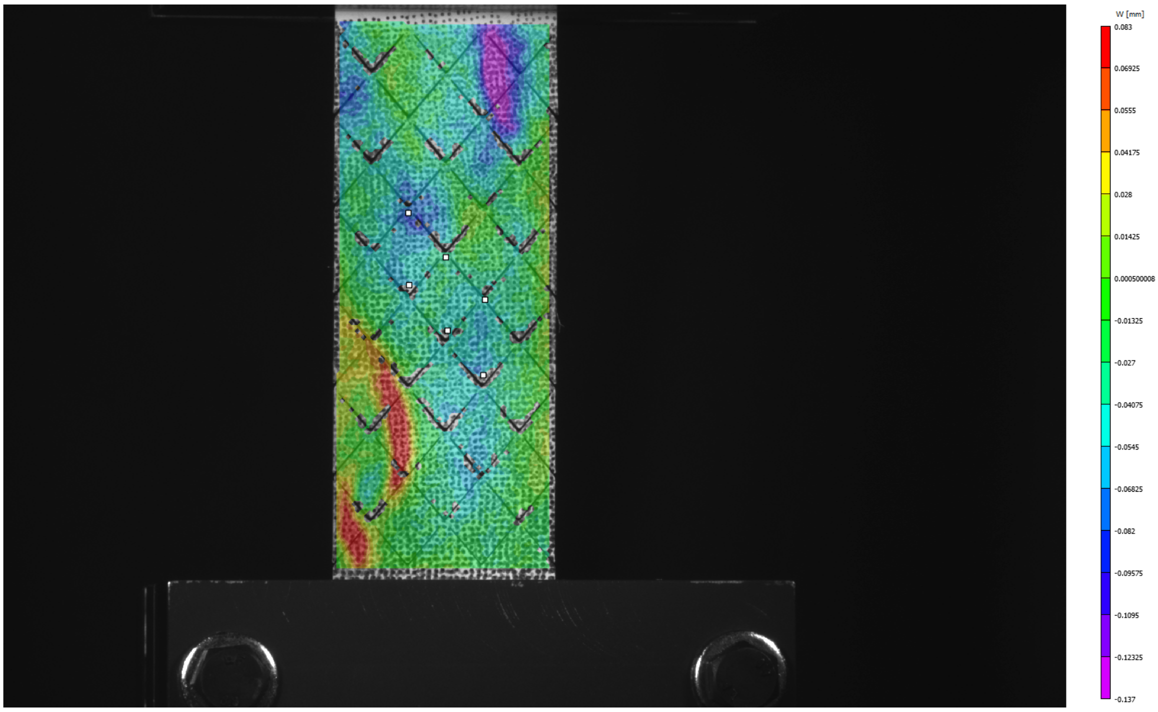

Figure A.25: 50 degree cut angle sample 1 Start

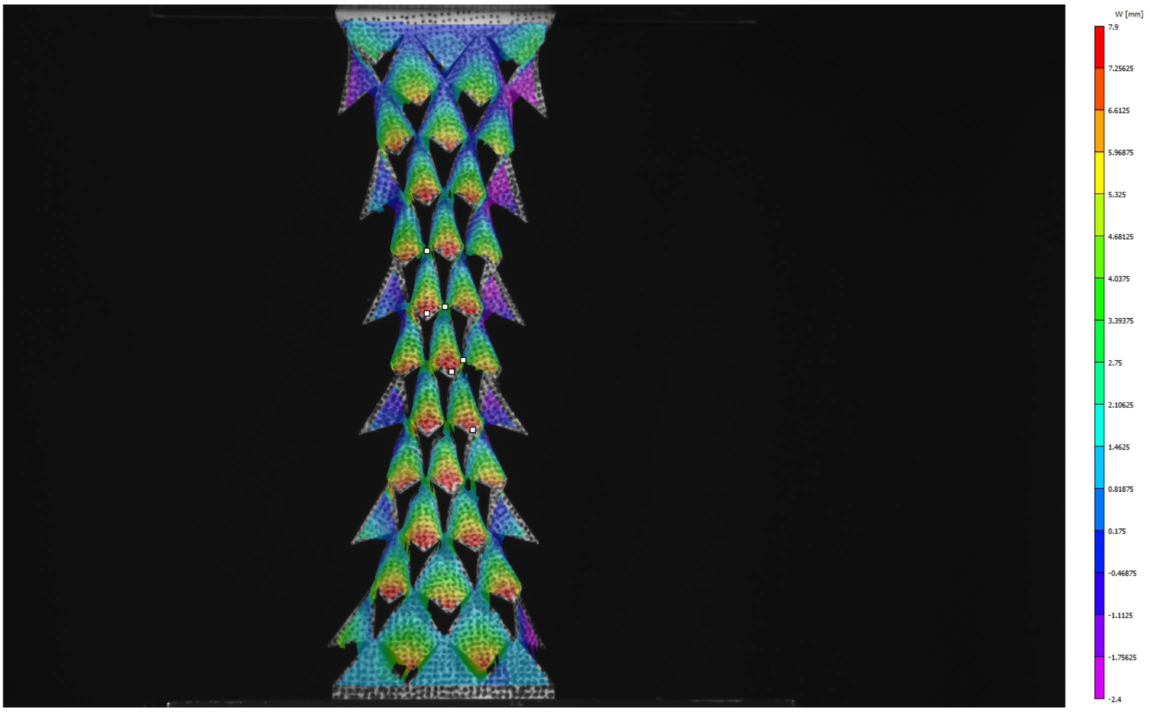

Figure A.26: 50 degree cut angle sample 1 End

2

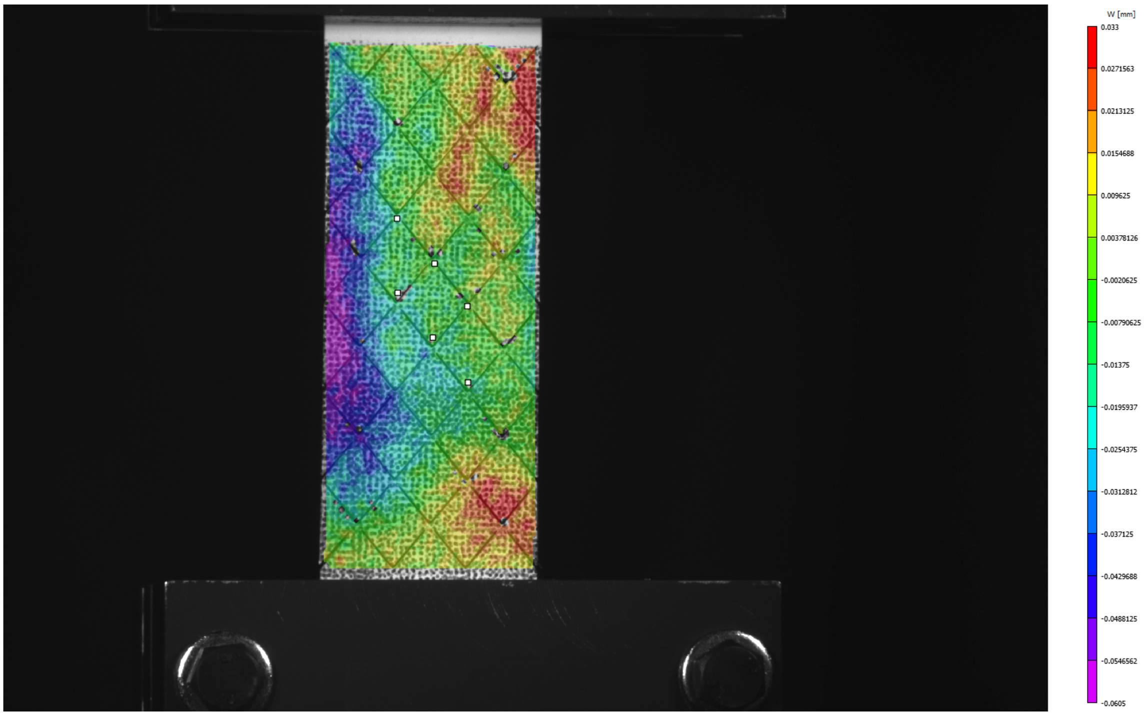

Figure A.27: 50 degree cut angle sample 2 Start

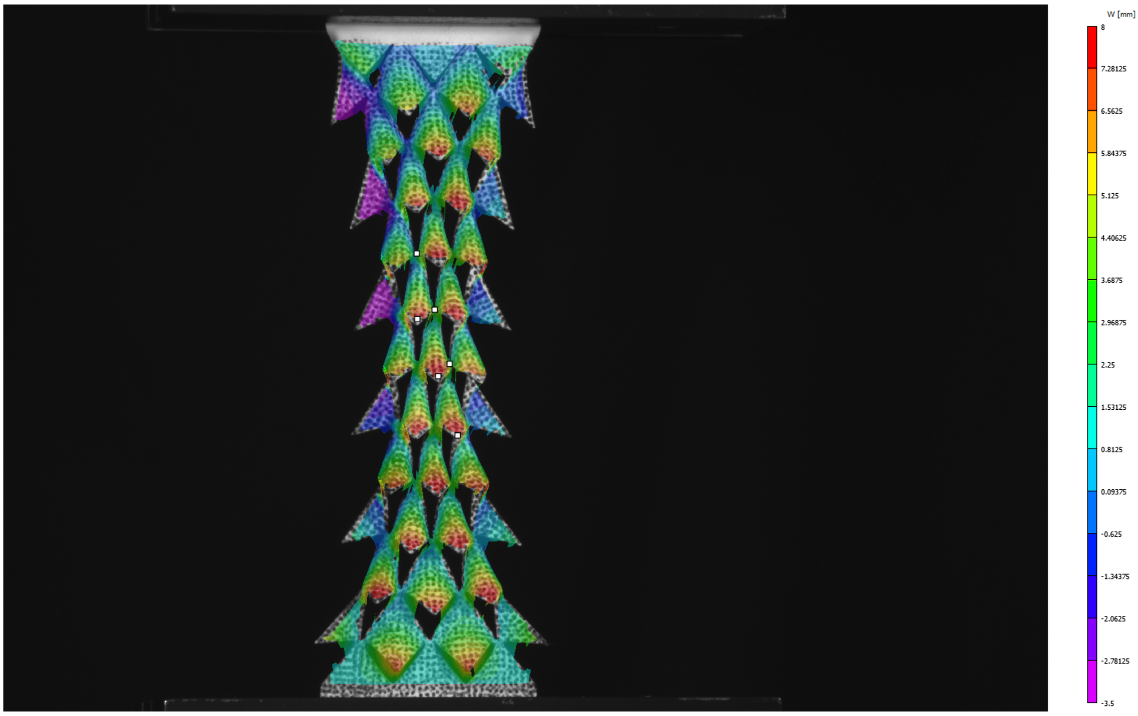

Figure A.28: 50 degree cut angle sample 2 End

3

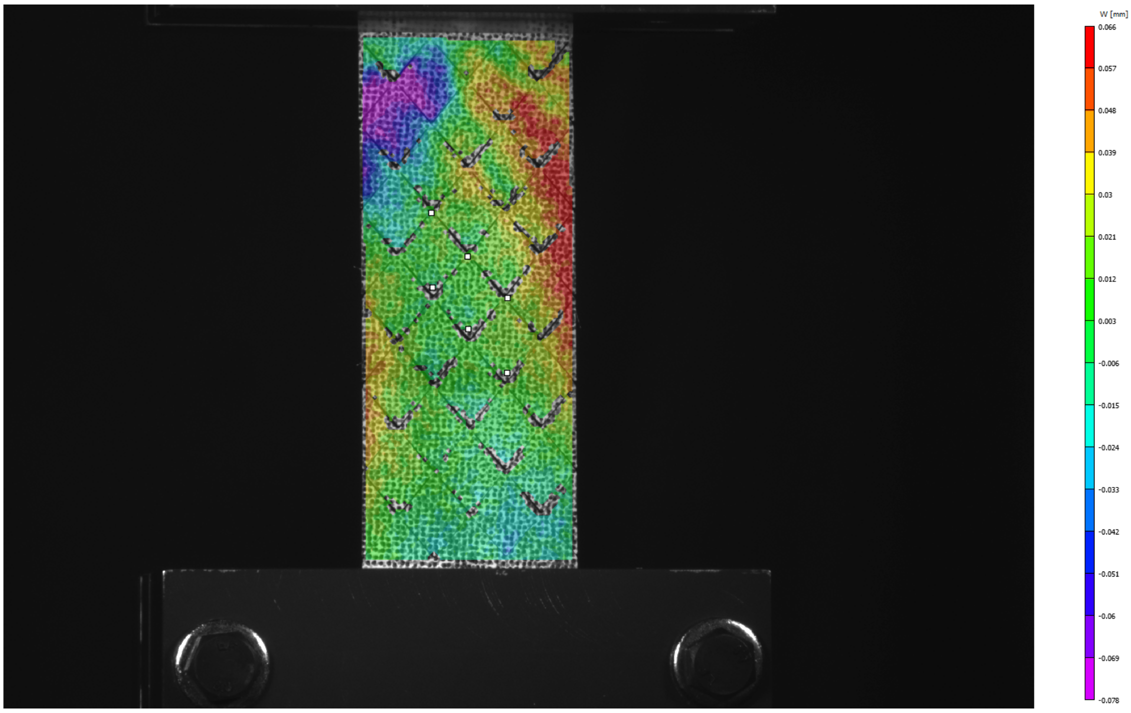

Figure A.29: 50 degree cut angle sample 3 Start

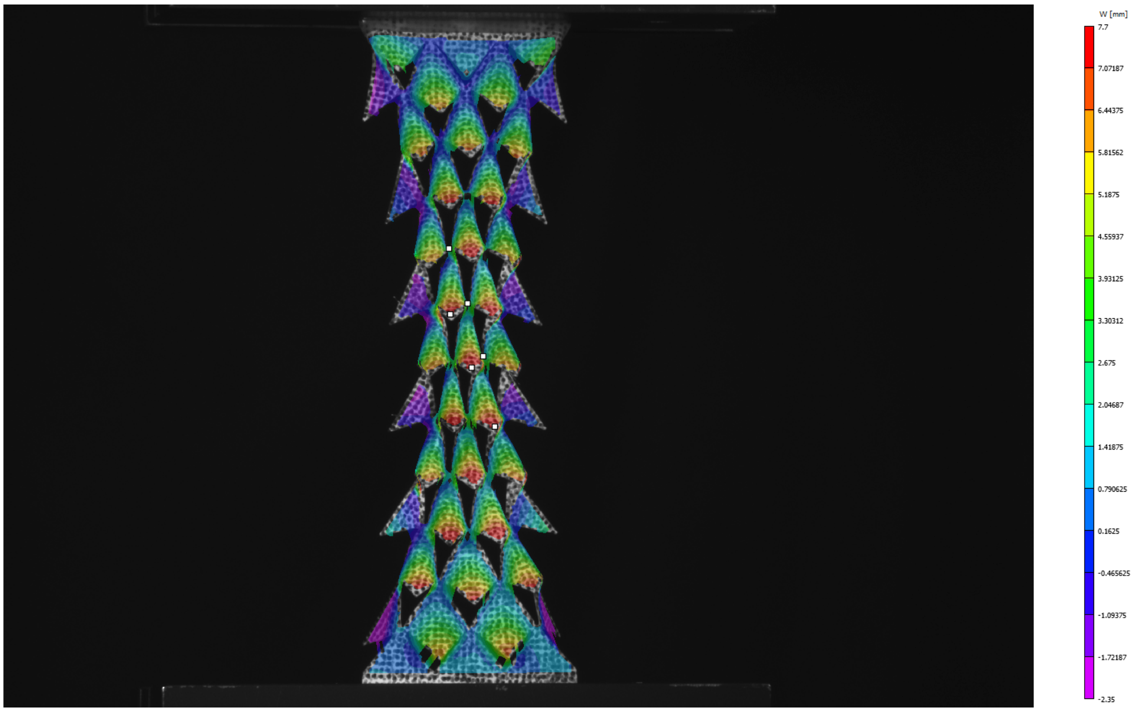

Figure A.30: 50 degree cut angle sample 3 End

4

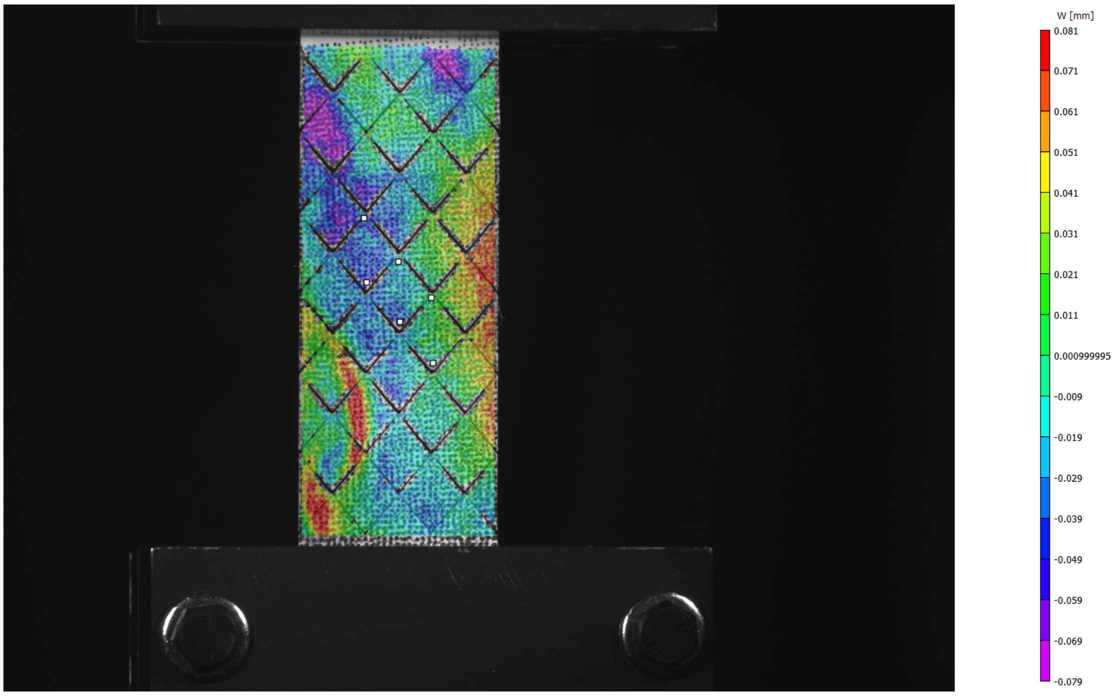

Figure A.31: 50 degree cut angle sample 4 Start

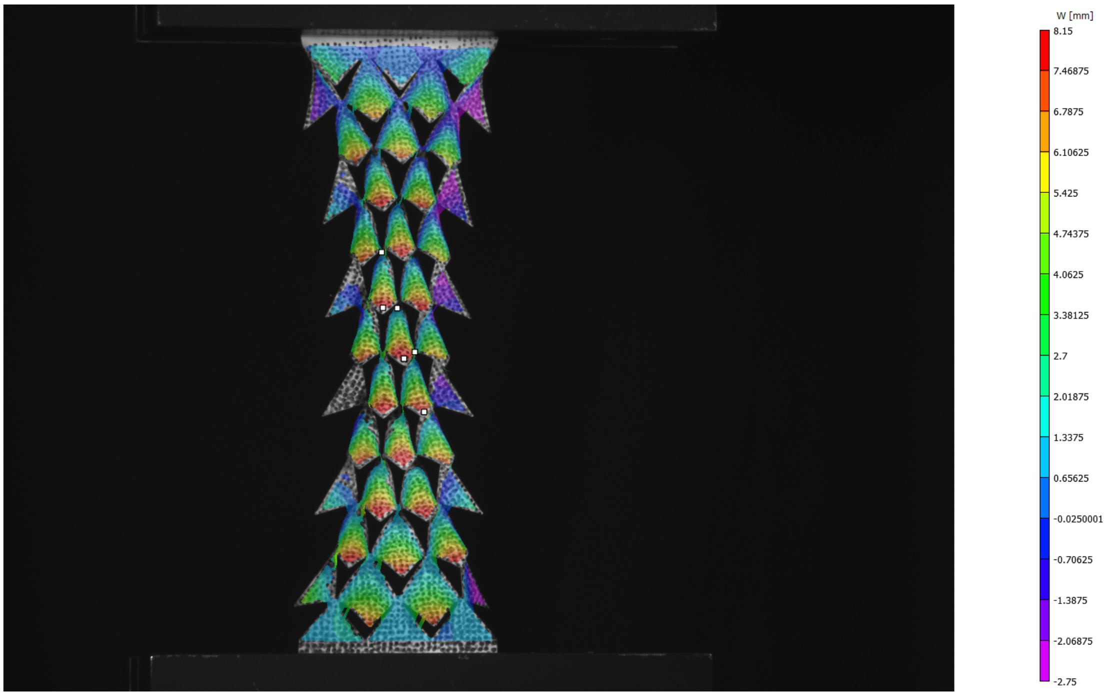

Figure A.32: 50 degree cut angle sample 4 End

60 Degree Samples

1

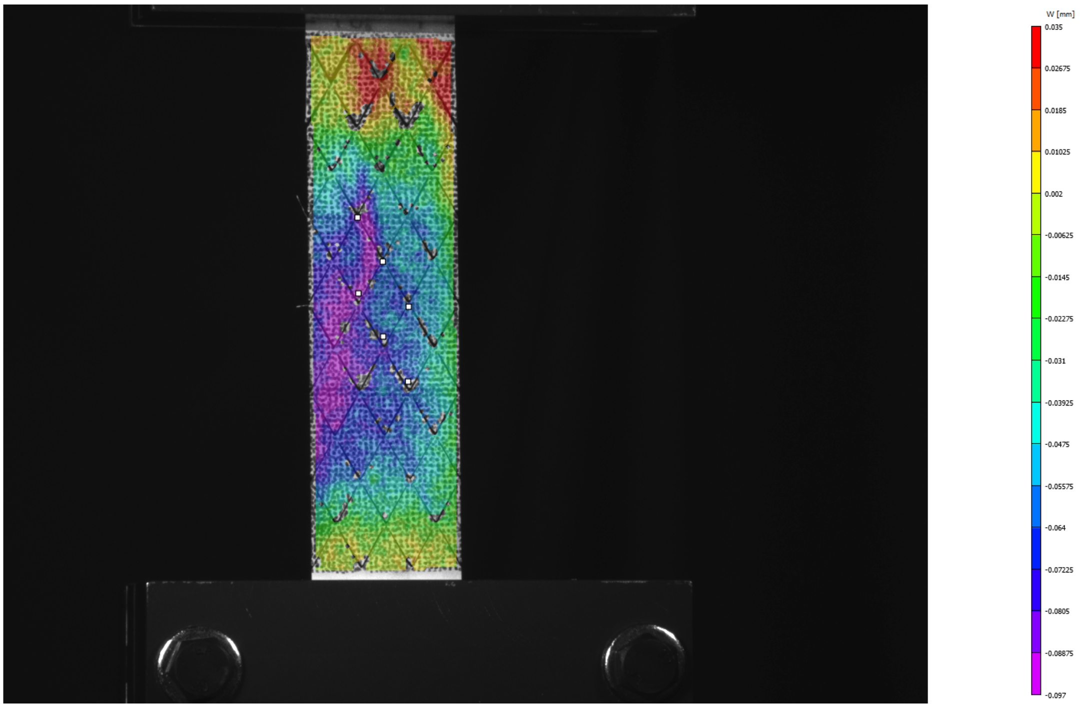

Figure A.33: 60 degree cut angle sample 1 Start

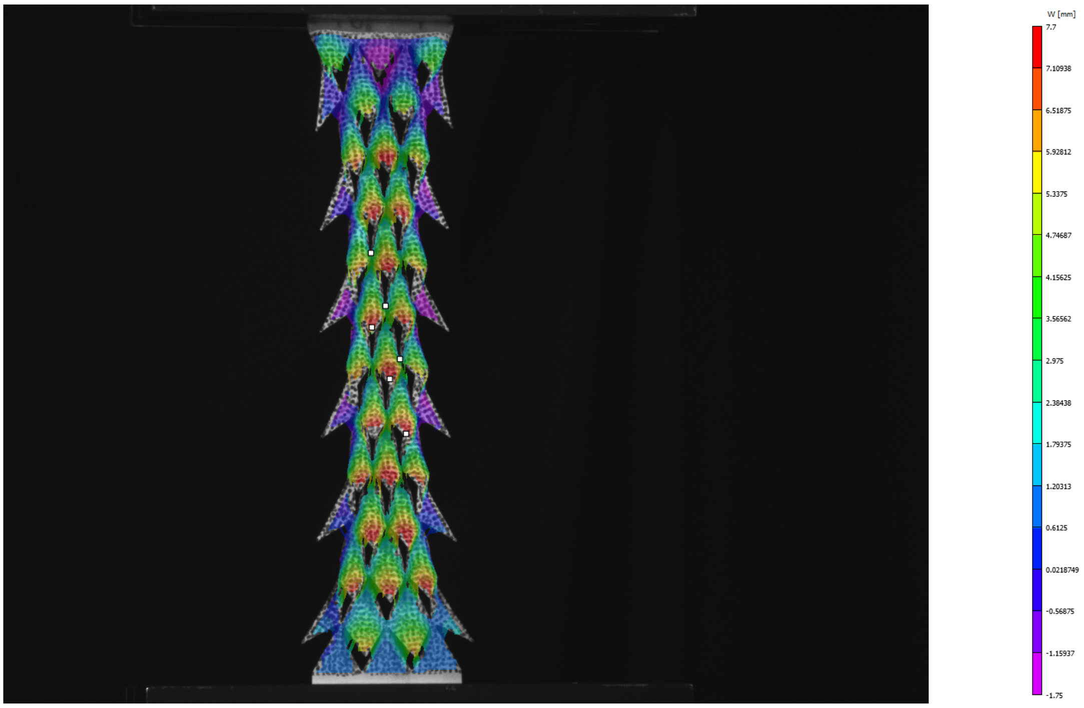

Figure A.34: 60 degree cut angle sample 1 End

2

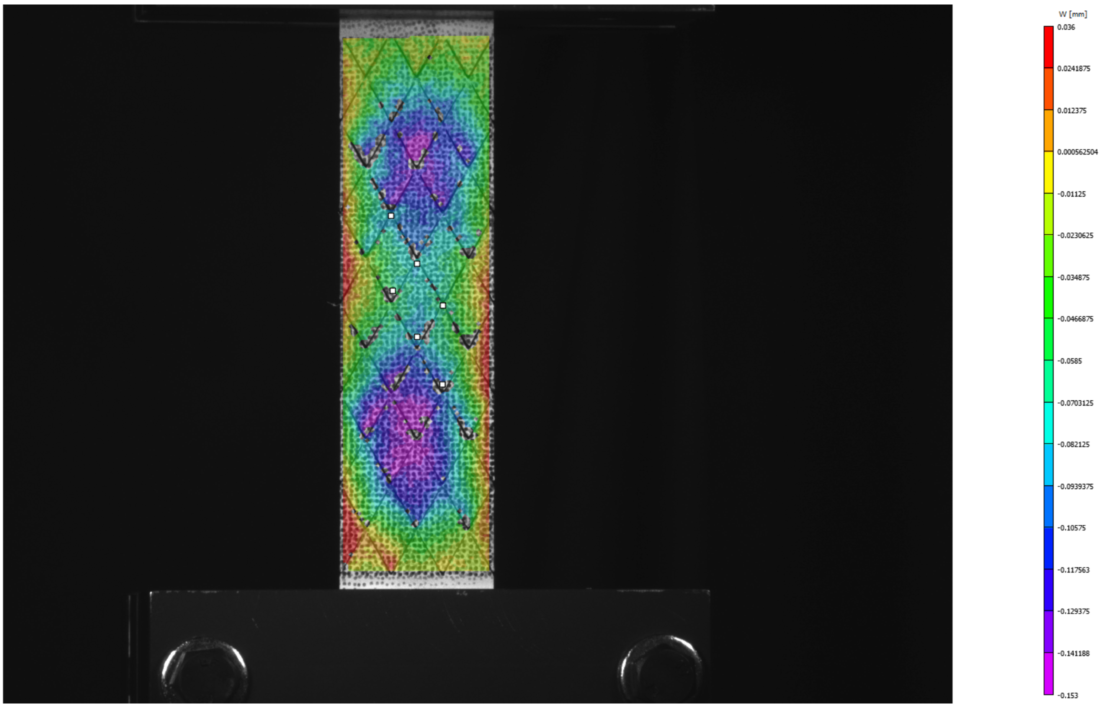

Figure A.35: 60 degree cut angle sample 2 Start

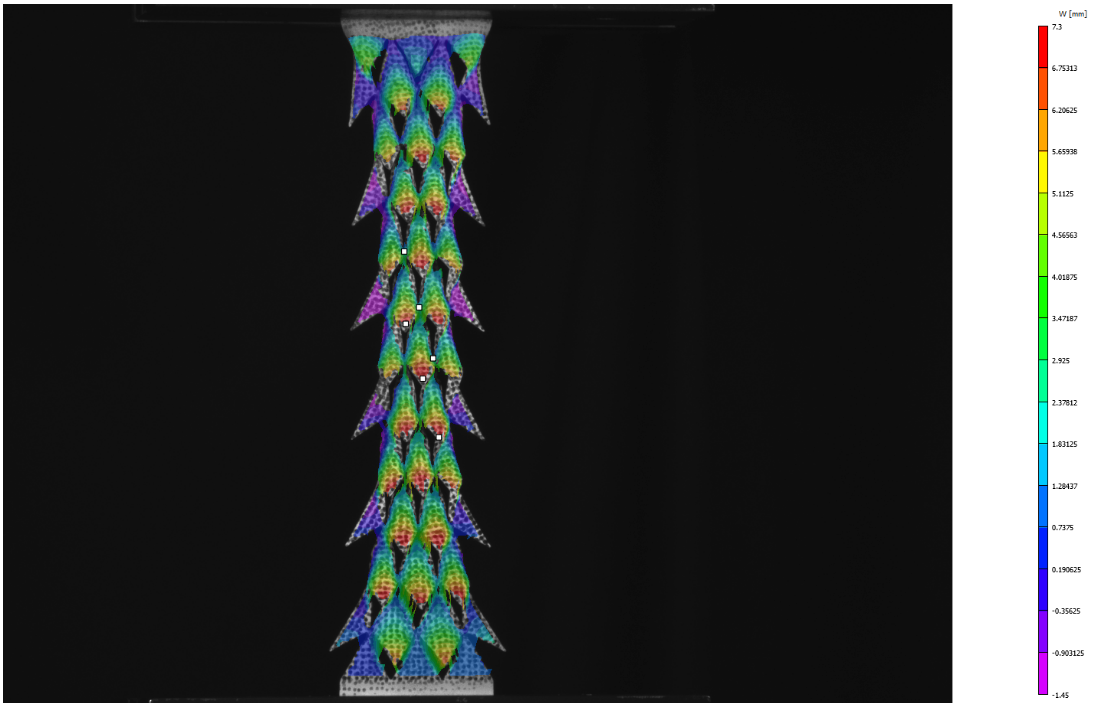

Figure A.36: 60 degree cut angle sample 2 End

3

Figure A.37: 60 degree cut angle sample 3 Start

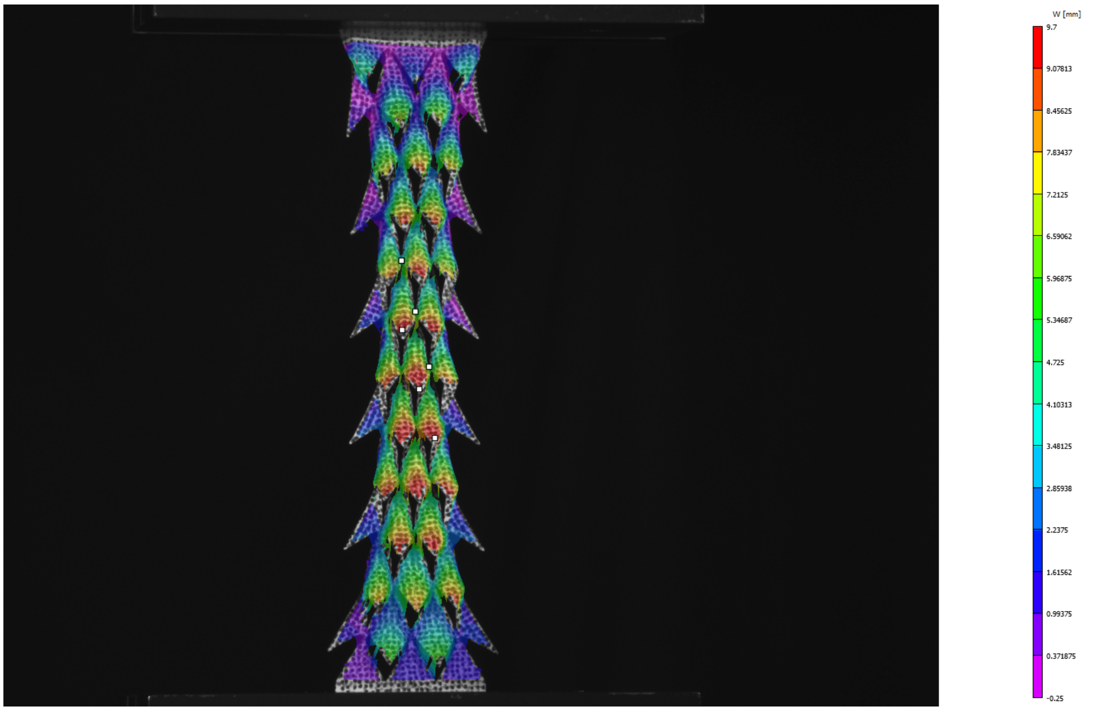

Figure A.38: 60 degree cut angle sample 3 End

4

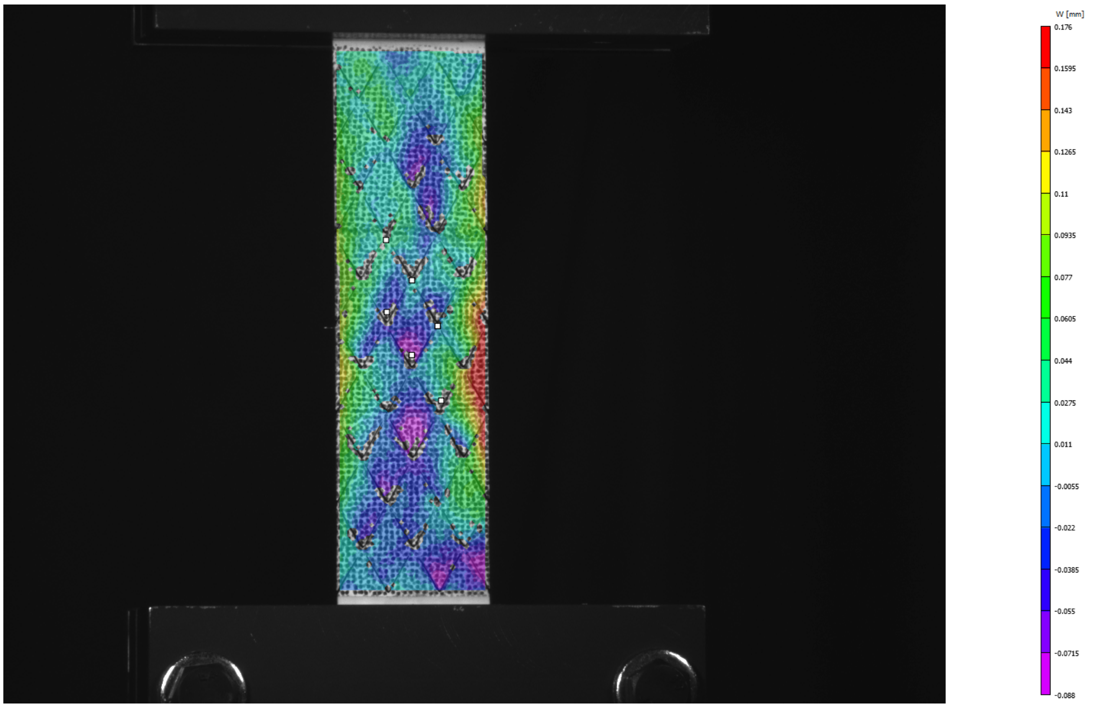

Figure A.39: 60 degree cut angle sample 3 Start

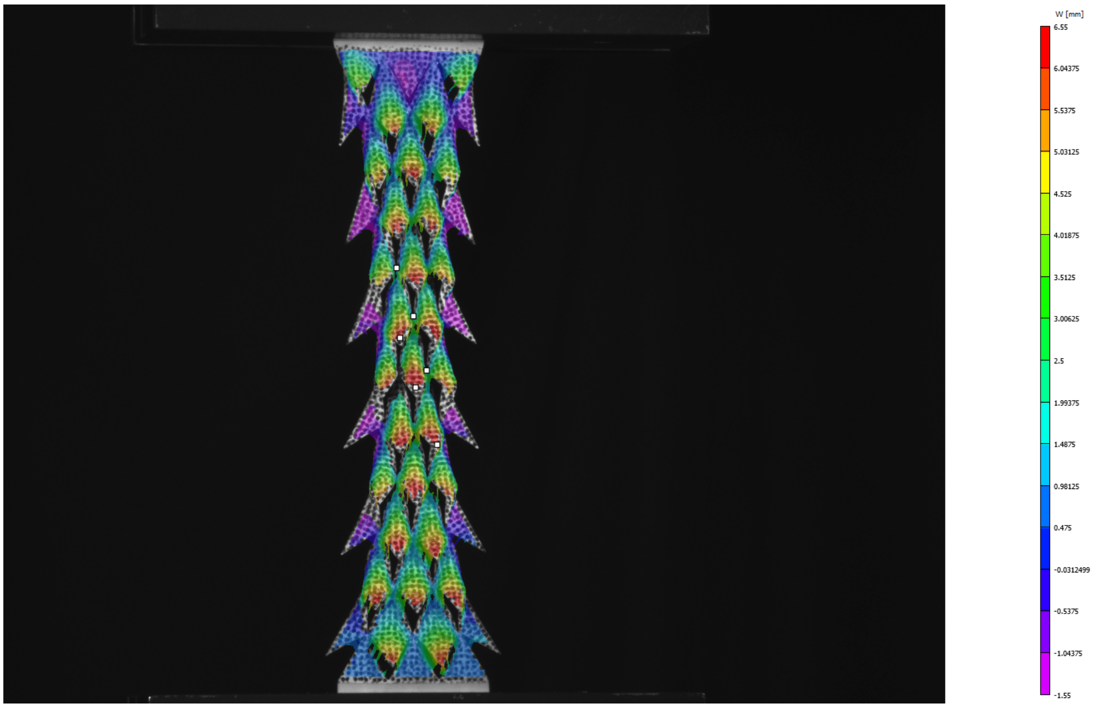

Figure A.40: 60 degree cut angle sample 3 End

Samples with δ/L= 0.15

30 Degree Samples

1

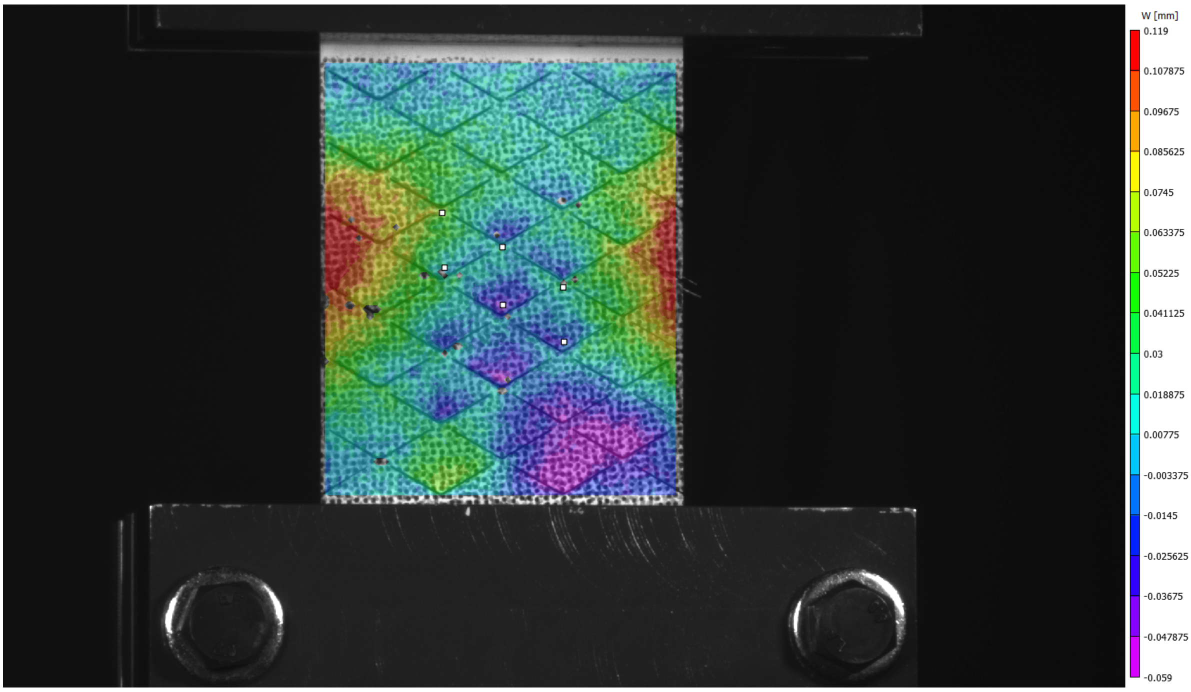

Figure A.41: 30 degree cut angle, δ/L= 0.15 sample 1 Start

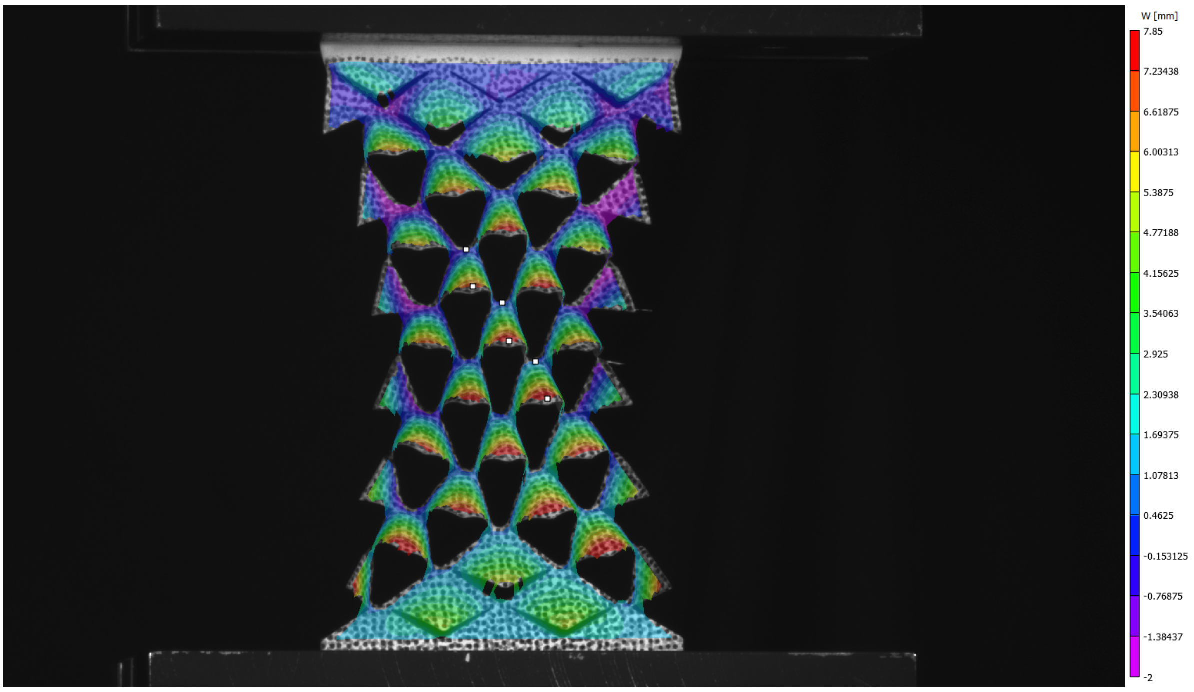

Figure A.42: 30 degree cut angle, δ/L= 0.15 sample 1 End

2

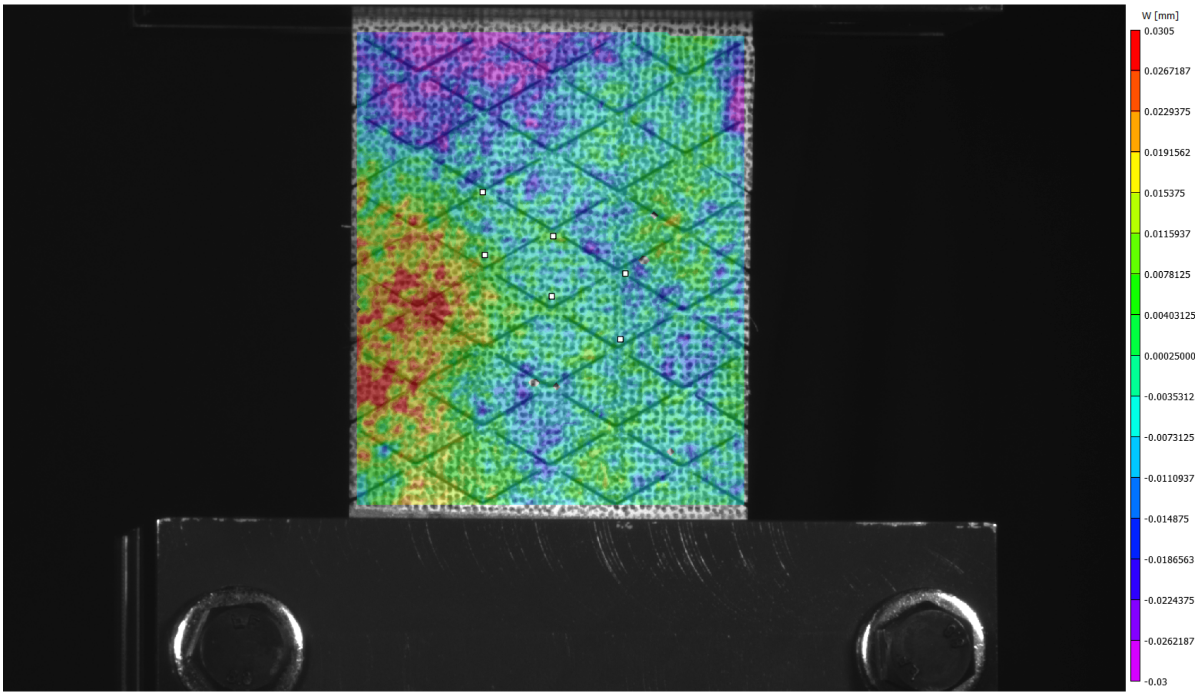

Figure A.43: 30 degree cut angle, δ/L= 0.15 sample 2 Start

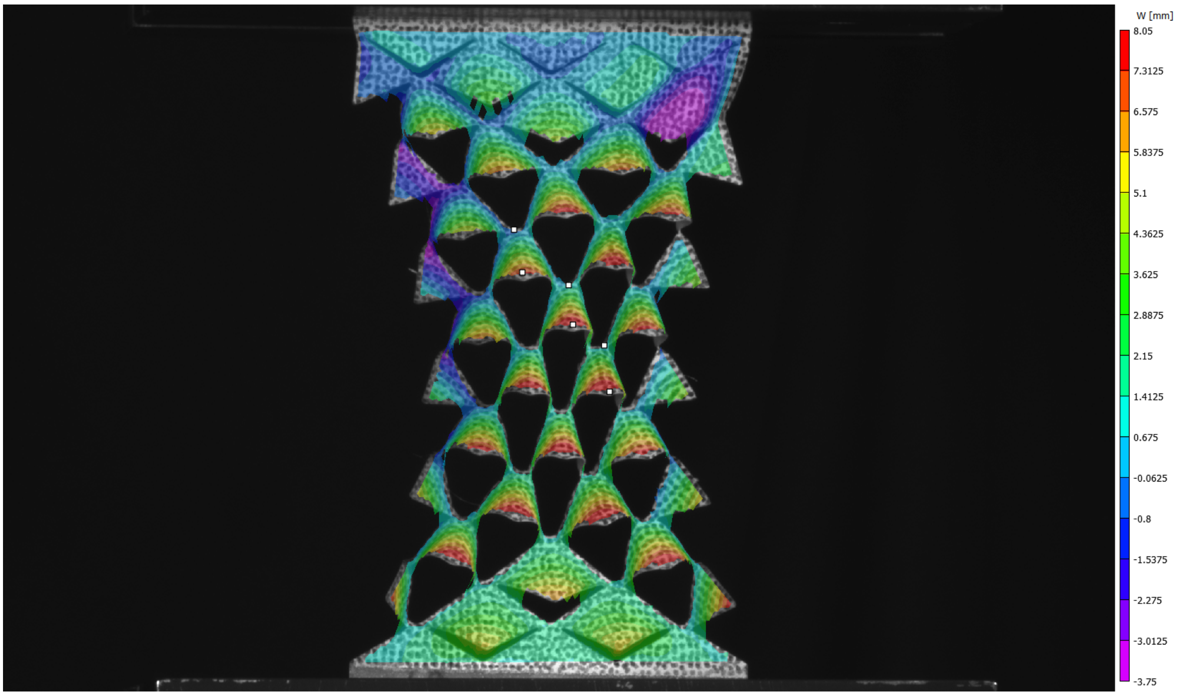

Figure A.44: 30 degree cut angle, δ/L= 0.15 sample 2 End

3

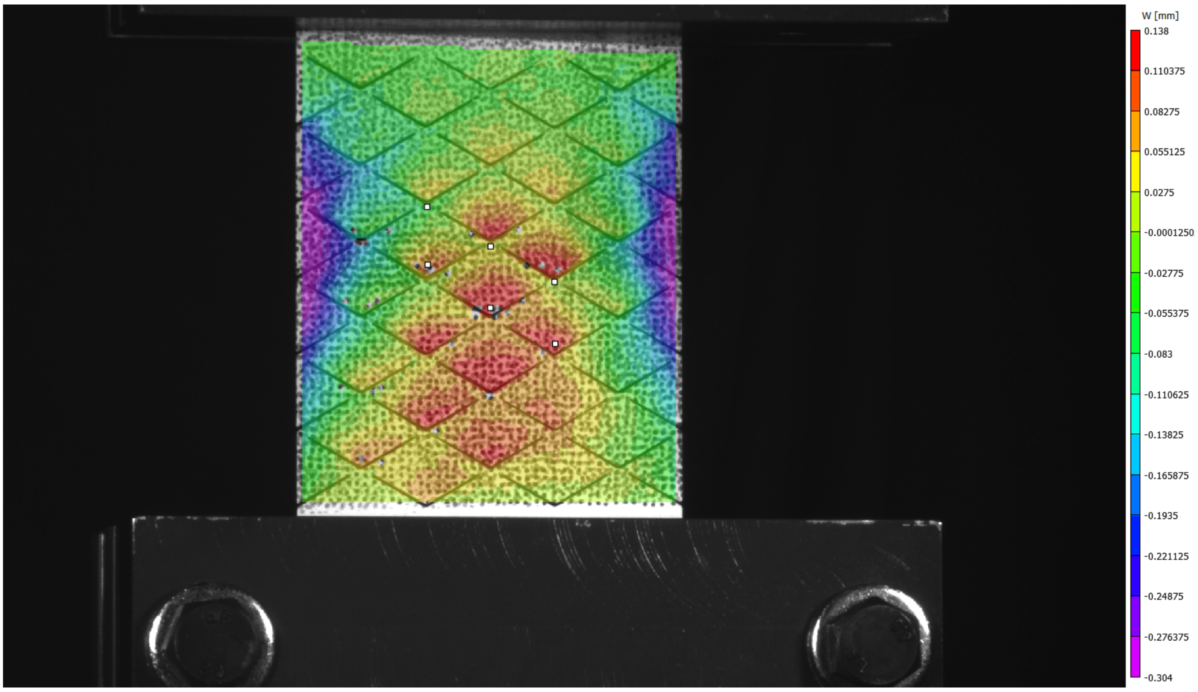

Figure A.45: 30 degree cut angle, δ/L= 0.15 sample 3 Start

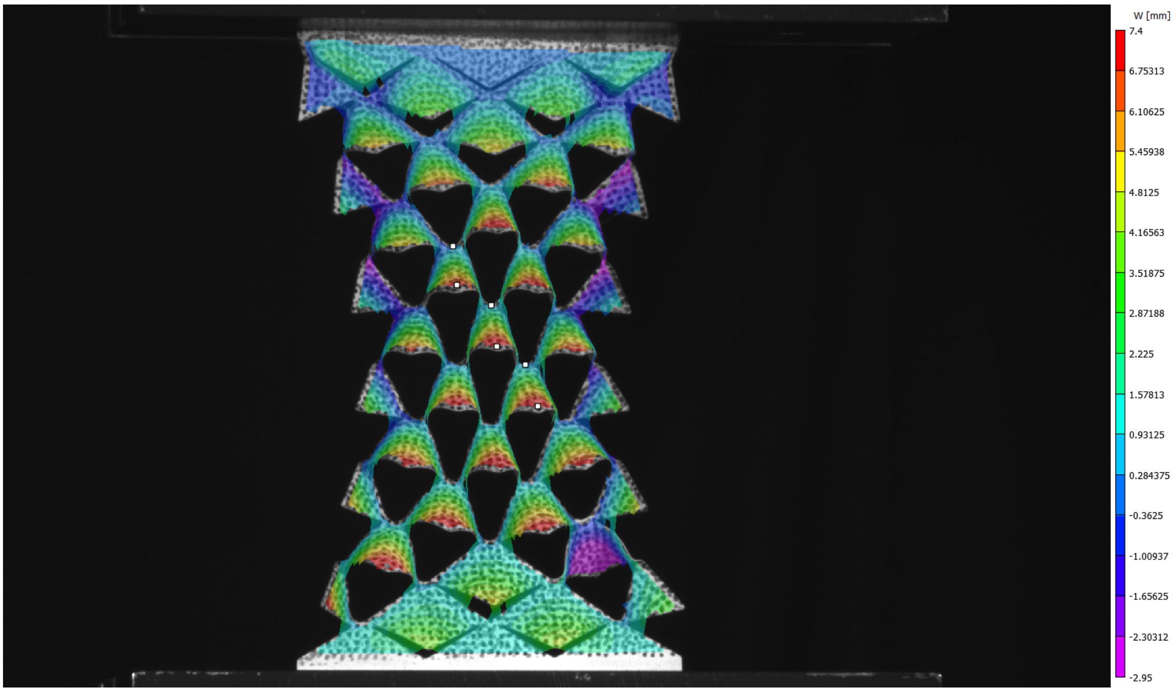

Figure A.46: 30 degree cut angle, δ/L= 0.15 sample 3 End

4

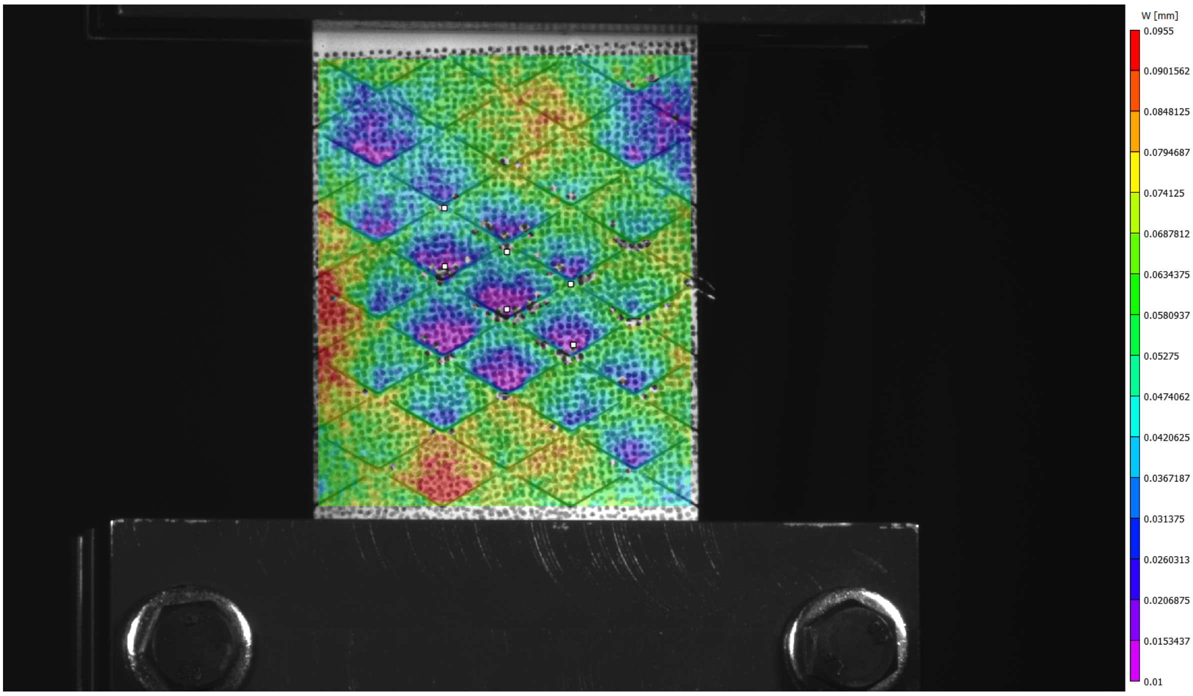

Figure A.47: 30 degree cut angle, δ/L= 0.15 sample 4 Start

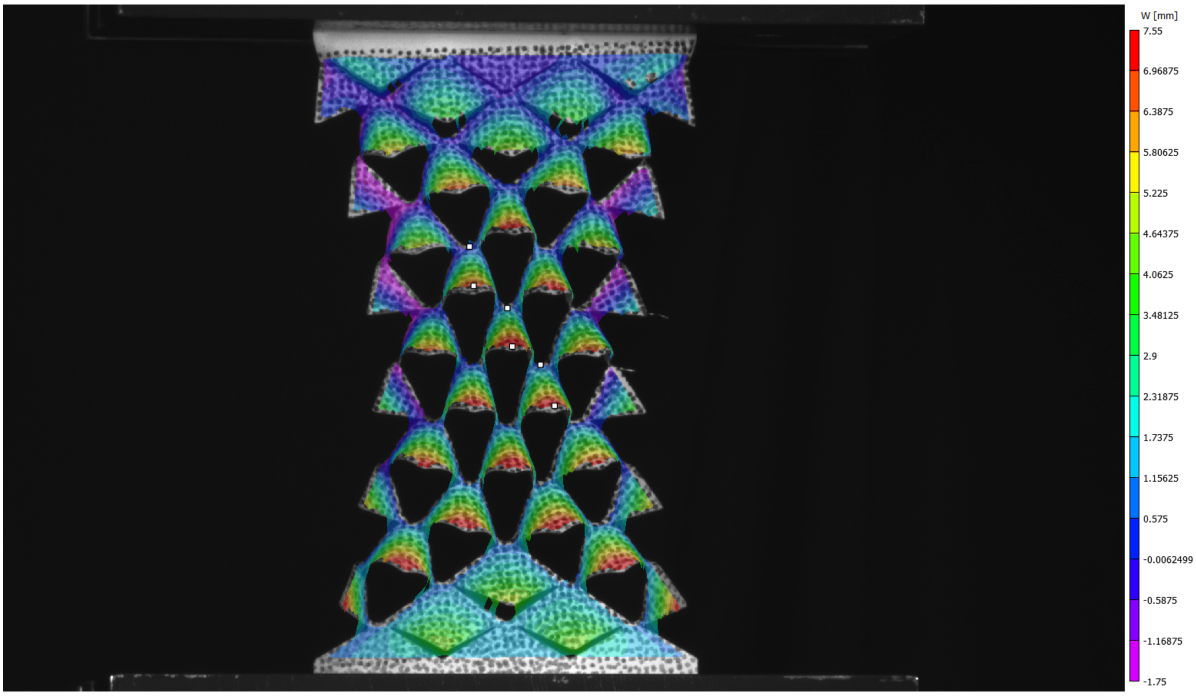

Figure A.48: 30 degree cut angle, δ/L= 0.15 sample 4 End

Samples with δ/L= 0.20

30 Degree Samples

1

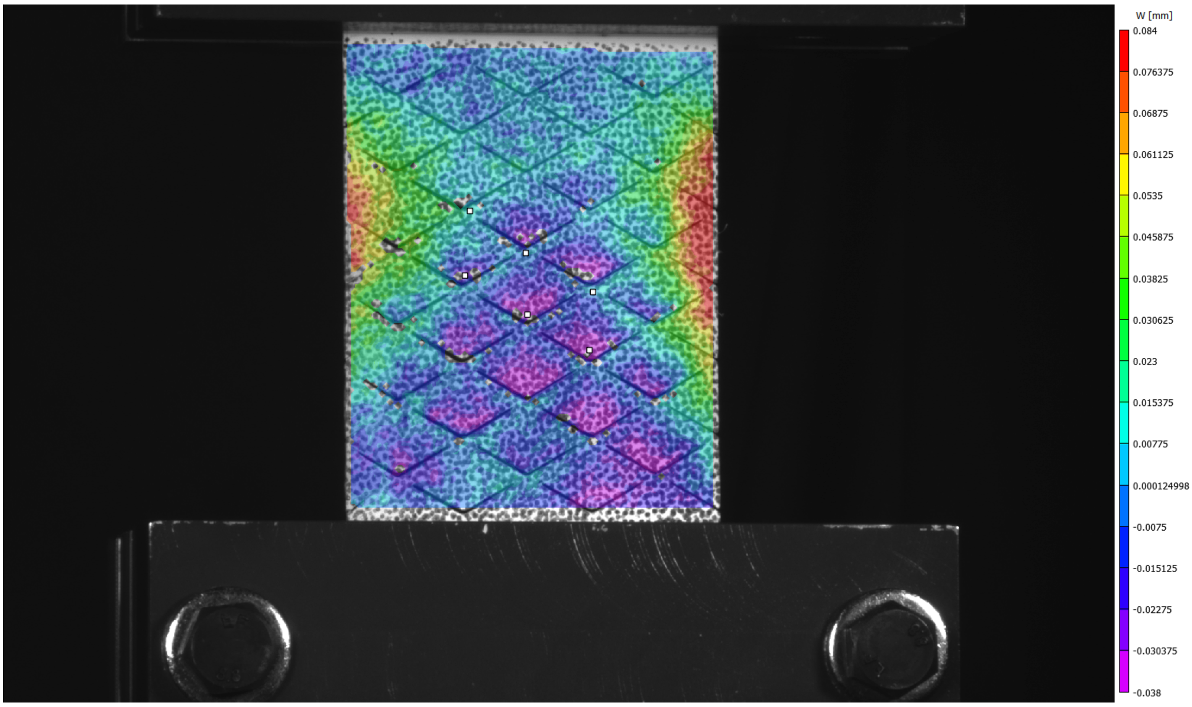

Figure A.49: 30 degree cut angle, δ/L= 0.20 sample 1 Start

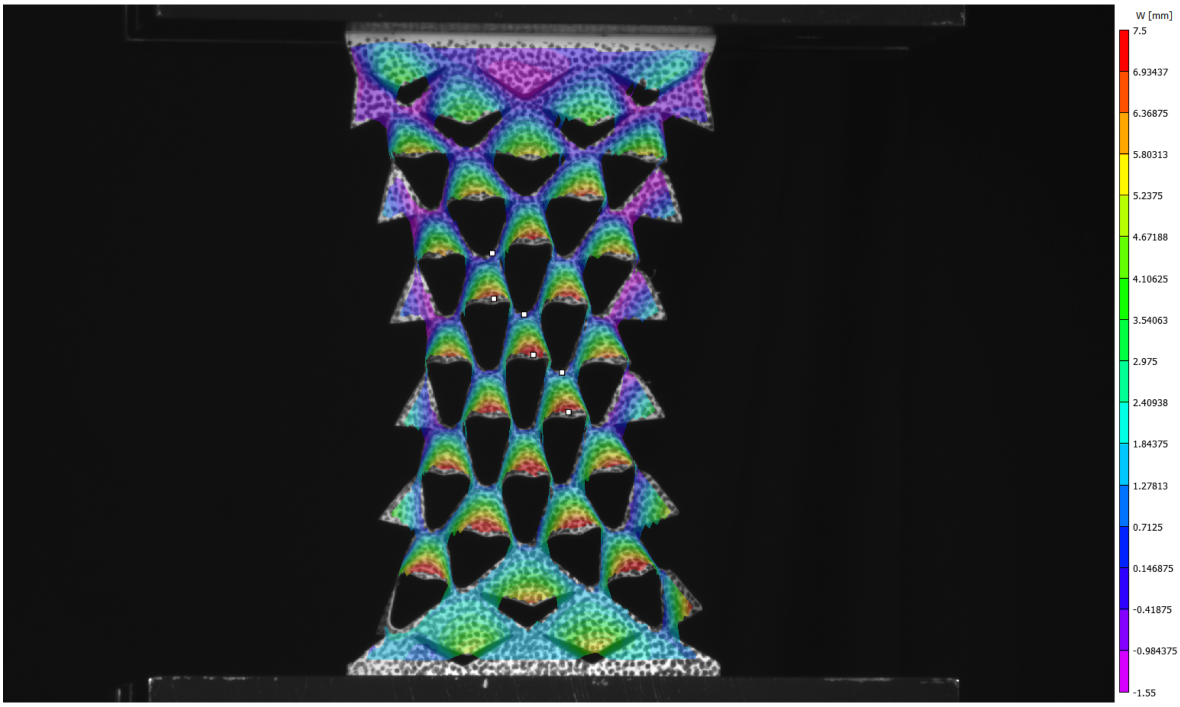

Figure A.50: 30 degree cut angle, δ/L= 0.20 sample 1 End

2

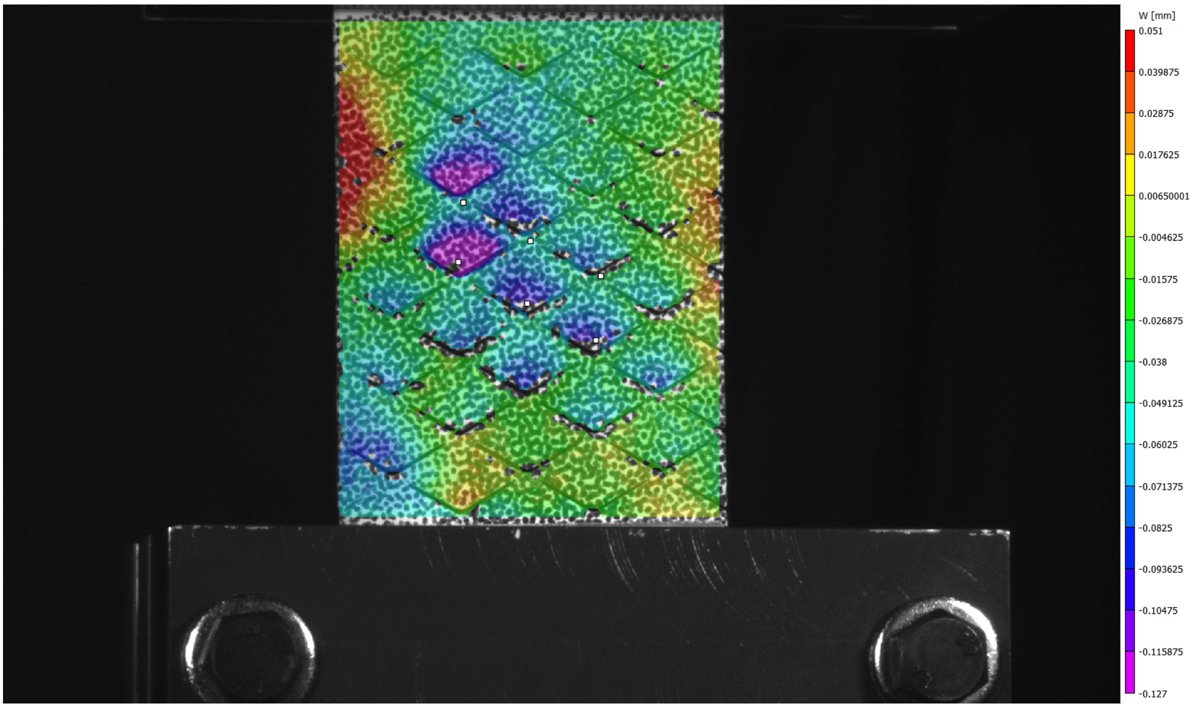

Figure A.51: 30 degree cut angle, δ/L= 0.20 sample 2 Start

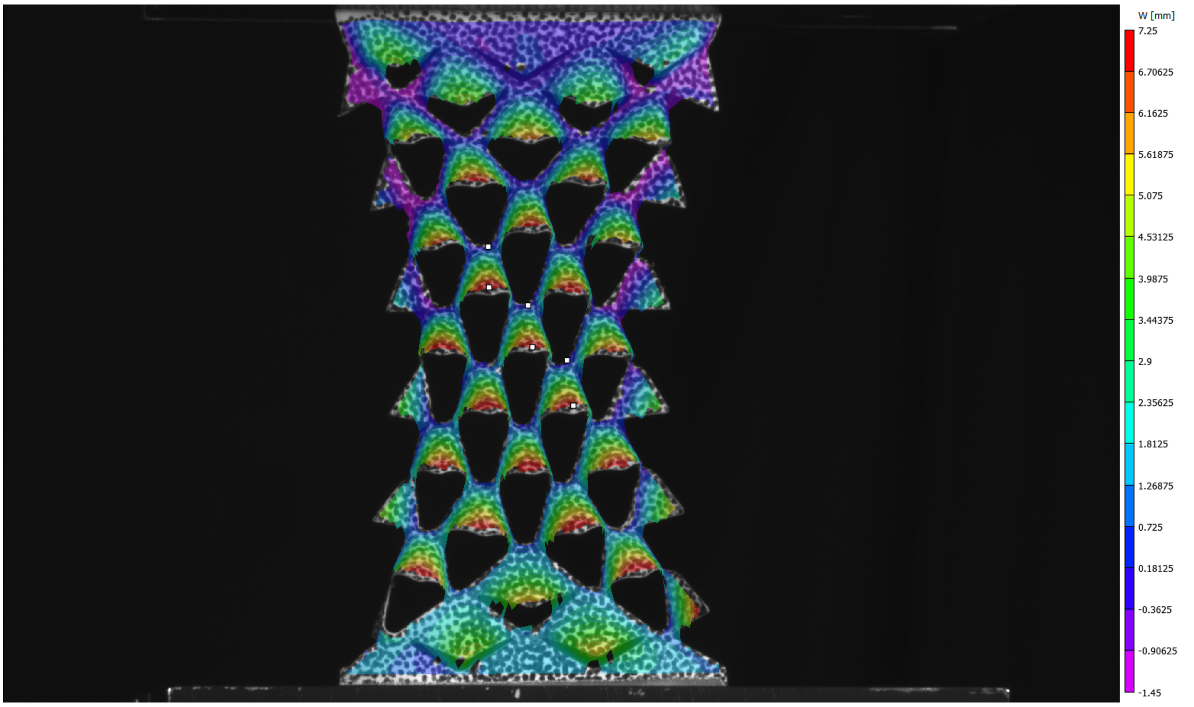

Figure A.52: 30 degree cut angle, δ/L= 0.20 sample 2 End

3

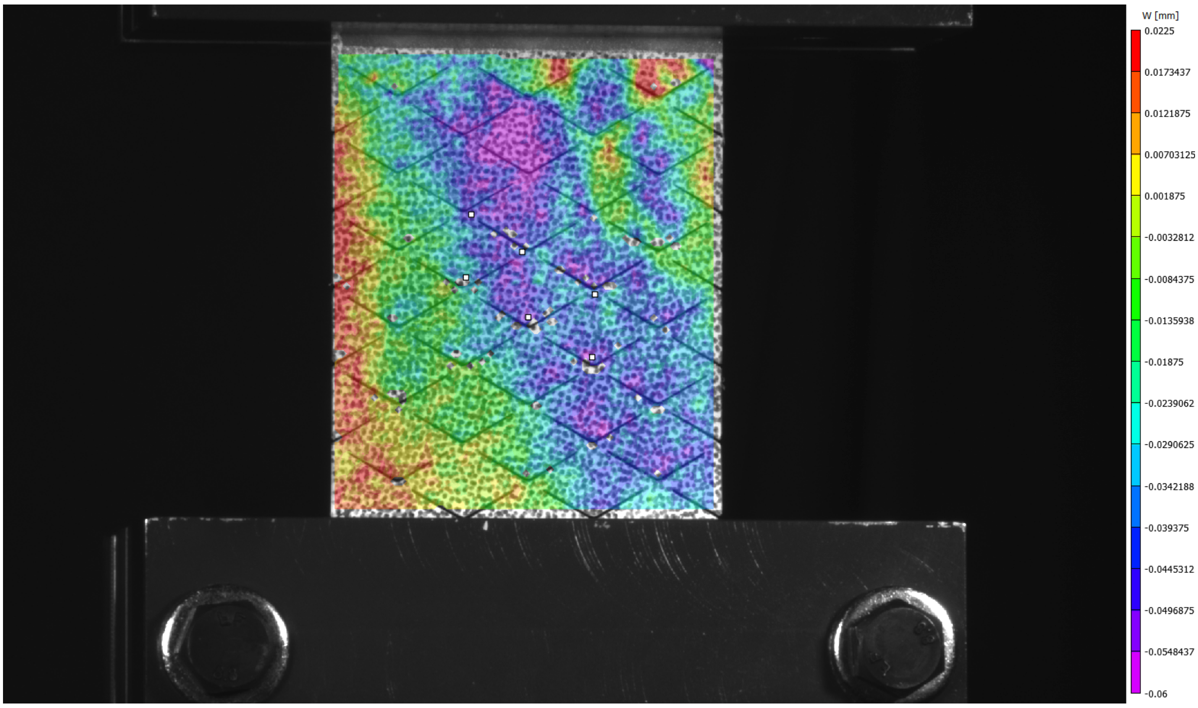

Figure A.53: 30 degree cut angle, δ/L= 0.20 sample 3 Start

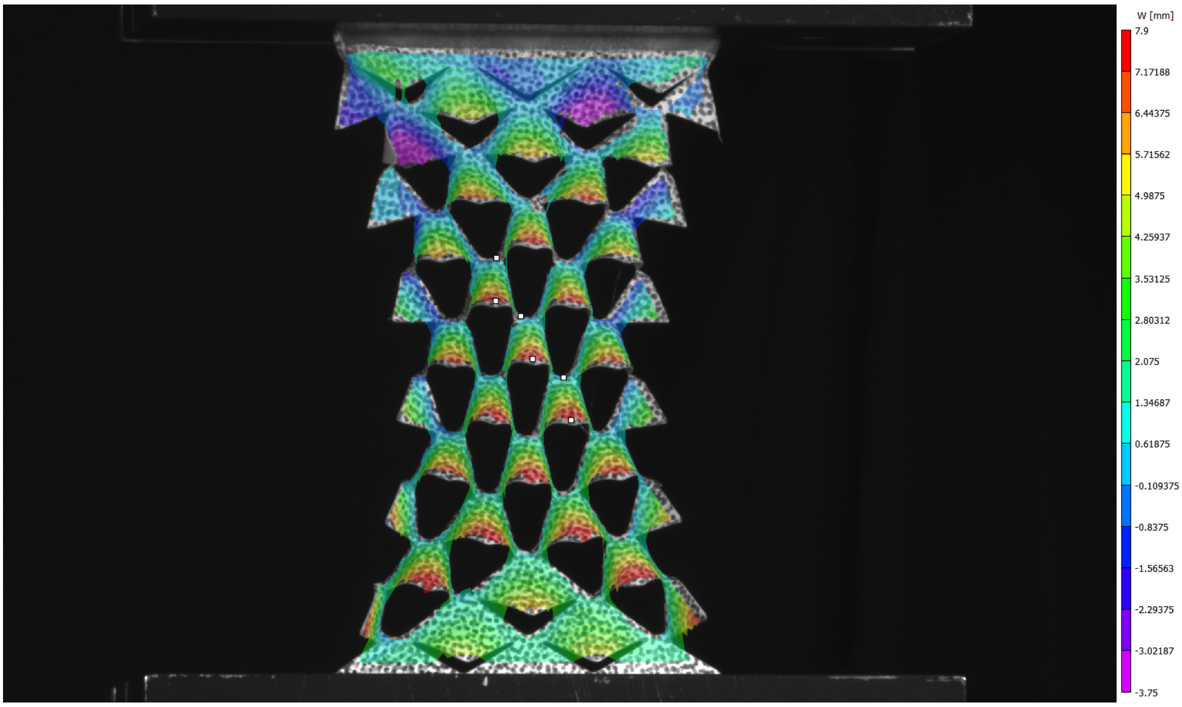

Figure A.54: 30 degree cut angle, δ/L= 0.20 sample 3 End

4

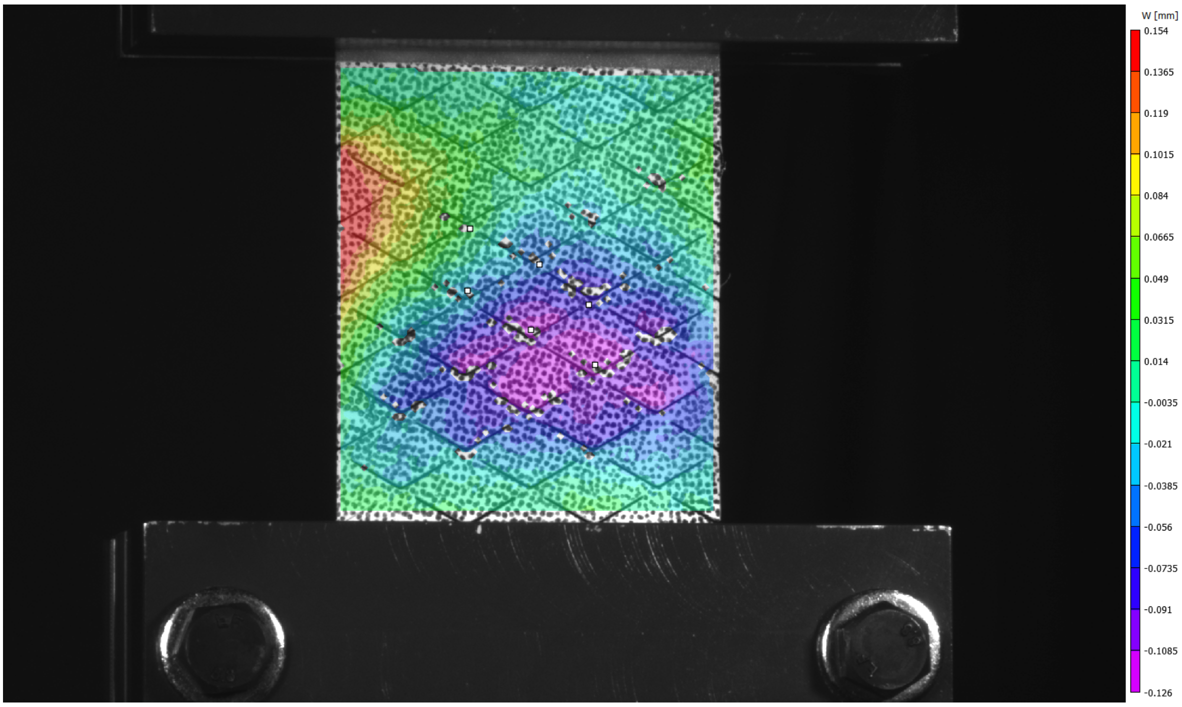

Figure A.55: 30 degree cut angle, δ/L= 0.20 sample 4 Start

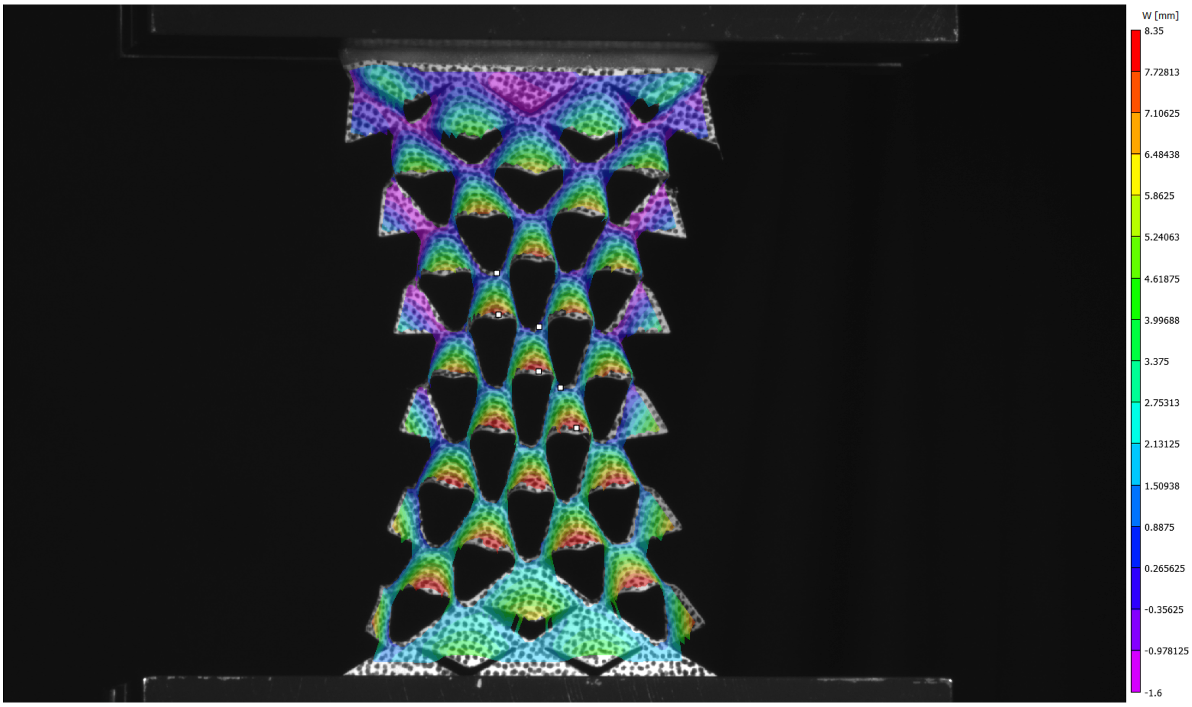

Figure A.56: 30 degree cut angle, δ/L= 0.20 sample 4 End